Investigating Exciton-Polaron interactions and their effect on high magnetic field effects in organic semiconductors

Tingting Zhang

Submitted in partial fulfillment
of the requirements of the Degree of
Doctor of Philosophy

8 September 2016

School of Physics and Astronomy
Queen Mary, University of London

Statement of originality

I, **Tingting Zhang**, confirm that the research included within this thesis is my own work or that where it has been carried out in collaboration with, or supported by others, that this is duly acknowledged below and my contribution indicated. Previously published material is also acknowledged below.

I attest that I have exercised reasonable care to ensure that the work is original, and does not to the best of my knowledge break any UK law, infringe any third party's copyright or other Intellectual Property Right, or contain any confidential material.

I accept that the College has the right to use plagiarism detection software to check the electronic version of the thesis.

I confirm that this thesis has not been previously submitted for the award of a degree by this or any other university.

The copyright of this thesis rests with the author and no quotation from it or information derived from it may be published without the prior written consent of the author.

. . . .

Tingting Zhang

8 September 2016

List of publication

Tingting Zhang and D. F. Holford et al. 'Hole-exciton interaction induced high field decay of magneto-electroluminescence in Alq_3-based organic light-emitting diodes at room temperature' Appl. Phys. Lett. 108, 023303 (2016).

H. Gu, S. Chang, H. Lu, D. F. Holford, **T. Zhang** et al. 'Impurity effects on charge transport and magnetoconductance in a single layer poly(3-hexyl-thiophene) device' Appl. Phys. Lett. 108, 203301 (2016).

H. Gu, S. Chang, D. Holford and **T. Zhang** et al. 'Annealing and doping-dependent magnetoresistance in single layer poly (3-hexyl-thiophene) organic semiconductor device' Organic Electronics 17, 51-56 (2015).

Tingting Zhang and D. F. Holford et al. 'Transient MFEs — direct evidence of triplet-charge carrier interaction' (in preparation).

List of Symbols

μ	mobility of charge carrier
μ_0	hypothetical mobility at infinite temperature and zero electric field
σ	energy disorder parameter
T	temperature in Kelvin
n	real number
k_B	Boltzmann constant
F	electric field
ΔE	Energy difference between two sites
E_F	Fermi energy
V_{ap}	applied bias
V_{bi}	Built in potential
η_{IQE}	Internal quantum efficiency
η_{EQE}	External quantum efficiency
γ	output-coupling factor
B_{hf}	hyperfine field
a_1	pre-factor for the first magnetic process
B_1	characteristic magnetic field for the first magnetic process
a_2	pre-factor for the second magnetic process
B_2	characteristic magnetic field for the second magnetic process
a_3	pre-factor for the third magnetic process
B_3	characteristic magnetic field for the third magnetic process

Abbreviation

OSC	organic semiconductor
OLED	organic light emitting diode
MFE	magnetic field effects
IVL	Current-Voltage-Luminescence
MEL	magnetic field effects on electroluminescence
EL	electroluminescence
PL	photoluminescence
TTA	triplet-triplet annihilation
TCI	triplet-charge carreir interaction
HOMO	highest occupied molecular orbital
LUMO	lowest unoccupied molecular orbital
MR	magnetoresistance
MC	magnetoconductance

Clarification

For the seek of simplicity and convenience, some terms used in the discussion of this thesis might appear to be ambiguous. To make it easier to understand, the terms which may cause confusion will be clarified here.

(1), without particular statement, **field** mentioned means magnetic field.
(2), **low field** means a magnetic field less than 50 mT.
(3), **polaron** refers to an electron or a hole residing on an organic molecule (polymer chain). In the thesis, it is equal to **charge carrier**.
(4), **free charge carrier** refers to an electron (a hole) that doesn't bond with a hole (an electron). **Free** here doesn't mean that these electrons and holes are delocalised like in a inorganic semiconductor.
(5), **bipolaron** refers to an organic molecule (polymer chain) containing two spin anti-parallel electrons or holes.
(6), **polaron pairs** refers to Wannier-Mott excitons.

Abstract

The research area of magnetic field effects (MFE) on organic systems has been intensively studied during the last decade. It has been revealed that there are processes that are subject to low fields (< 50 mT) and processes that are subject to high fields (> 50 mT). While the low field processes are widely accepted to be a result of the suppression of the spin mixing caused by random hyperfine fields and spin-orbit coupling within the devices, the origin of the high field processes is still not clear. Although several mechanisms, like triplet-charge carrier interaction (TCI) and triplet-triplet annihilation (TTA), were proposed to explain the high field MFEs, how these processes are affected by a magnetic field is not well understood. This thesis presents a study of the role of excitons on MFEs using aluminium tris(8-hydroxyquinolinate) (Alq_3) based diodes, focusing on the behaviour of high field effects on electroluminescence (MEL).

In order to investigate the role of excitons on high field MEL, devices with different structures were designed to modify the population of exciton and excess charge carriers in the devices via controlling the injection of charge carriers. In this way, the exciton population dependent TTA and TCI processes can be studied further and even distinguished, since the TTA depends mainly on the population of triplets while the TCI depends on the exciton to charge carrier ratio. Steady state MFE measurements were performed, and results show that significant high field MEL decay can be seen in a device with extremely low triplet concentration. This indicates that TTA cannot be the underlying mechanism of high field MEL decay. The gradual trend of high field MEL, changing from a moderate increase to significant decays upon adjusting the hole and electron injection from balanced to severely hole dominated, suggests that this high field decay is exciton-hole interaction dependent.

To decompose the role of singlets and triplets on high MELs, transient MFE measurements were performed on the Alq_3 based standard devices. Since in Alq_3 layer singlets feature a lifetime of $\sim$ ns and triplets feature a lifetime of $\sim \mu$s, the

behaviour of MEL at the rising edge and the falling edge of a pulse can provide a useful tool. Results show that an extra component occurs in the transient MEL at large current density and high fields. This indicates that the high field MEL is related to triplet-charge carrier interaction.

Acknowledgement

I would like to thank Prof. Bill Gillin, my supervisor, first and foremost for his patient and detailed advice during my PhD study. It is Prof. Gillin who spent his valuable time guiding me through the research process, teaching me to be critical when dealing with literature. He has an enormous experimental experience and theoretical knowledge on my research project, which helped pushing my understanding of the research related problems deeper and wider.

Besides, I would like to thank Dr. Theo Kreouzis, my co-supervisor, for always being there to help me with charge transfer, transient and mobility related problems. I couldn't express how much gratitude I own him every time when he patiently writes down equations or diagrams on his white board, trying to make things clear to me.

My completion of this project could not have been so smoothly without the lab staff. Thanks to Geoff for teaching me so many things and for being there whenever there is a problem in the clean room. Thanks to Ken for making things easier in the optical lab, the cryo State, liquid nitrogen, the lenses and the microscopes. Thanks to George for having the ITO substrates backed whenever it is needed.

I would like to extend my thanks to my colleagues. The biggest thank goes to Dave who has helped me in a lot of ways. We have cleaned the Kurt Lesker together, twice, and tested some of the other experimental equipments together. Thanks to Shuo Han, Jianxu Hu, Yu Peng, Hang Gu, Huanqing Ye, Tongtao Zhang and HaiZhou Lu, for being helpful in different ways: problem discussion or experiment guidance.

Many thanks to Filippo who has helped proof read my first year report, to Helen and Dominic who has proof read some of my thesis.

My grateful also goes to all the academics in the CCMMP group, especially Prof. Martin Dove, Dr. Kostya Trachenko and Dr. Alston Misquitta. Thanks to all the research students in the department (both present and past), the PhD life become more interesting, relaxer and funnier because of your presence.

Lastly, I would like to thank my parents, my other family members and all my friends for providing me a lot of help and support in every aspect of my life.

I am grateful to the Chinese Scholarship Council (CSC) for my PhD. research funding.

Contents

List of Figures

List of Tables

Chapter 1

Introduction

1.1 Introduction to organic semiconductors

Organic semiconductors (OS) refer to semiconductors consisting of mainly carbon and hydrogen atoms. One key feature of organic semiconductors is that they are conjugated systems containing alternating carbon single and double bonds. Therefore organic semiconducting molecules usually contain aromatic benzene rings or polymer chains with alternating double and single bonds. These systems contain conjugated π-electrons which give them the semi-conducting nature. Owing to the ease of structure modification, chemical tunability, mechanical flexibility, and self-assembly, organic semiconductors have been widely used in manufacturing promising devices such as organic light emitting diodes (OLEDs) [1–3] photovoltaic cells [4, 5], and field effect transistors [6, 7].

1.1.1 Origin of conduction

SP^2 hybridisation

To understand the semi-conducting nature of an organic molecule, it is important to explain the sp$_2$ hybridised orbitals. Figure 1.1 shows a diagram of the sp$_2$ hybridisation process. The original electron configuration of a carbon atom is $1s^2 2s^2 2p_x^1 2p_y^1 2p_z^0$. When a carbon atom needs to be attached to three groups, the sp^2 hybridisation occurs by promoting one electron from the $2s$ orbital to the unoccupied $2p_z$ orbital and mixing the $2s$ orbital with the two p orbitals ($2p_x$ and

$2p_y$) to create three sp^2 orbitals. After sp^2 hybridisation, the electron configuration of this carbon becomes $1s^2(sp^2)^3 2p_z^1$.

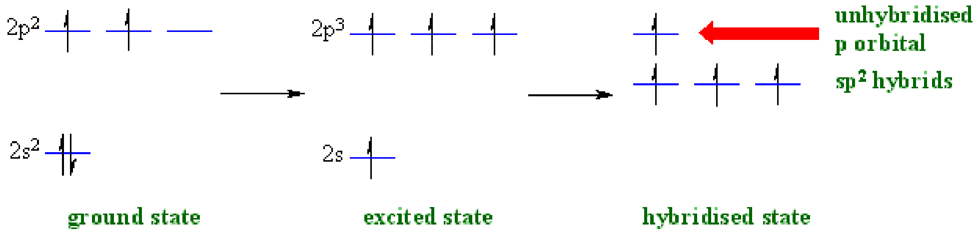

Figure 1.1: sp^2 hybridising processes for a carbon atom.

π-conjugation

A π conjugated system refers to a system with alternating single and double bonds. Here I use a benzene molecule to explain the π-conjugation. In a benzene molecule, there are six carbon atoms, each of them forming sp^2 hybridised orbitals. The three sp^2 orbitals of each carbon atom form a plane with a bonding angle of 120 degrees. Two of the three sp^2 orbitals overlap, separately, with one sp^2 orbital from its two adjacent carbon atoms, forming the backbone of the benzene ring. The remaining sp^2 orbital is attached to a hydrogen atom. σ-bonds are formed in each overlapping area. A simplified diagram is presented in figure 1.2 to show the bonds. Linear combination of these σ-bonds form a bonding (σ) and an anti-bonding (σ^*) orbitals in the molecule. The $2p_z$ orbitals are perpendicular to the plane formed by the σ-bonds. Six $2p_z$ bonds overlap sideways weakly, forming the π-bonds as shown in figure 1.3. Similar to σ-bonds, the linear combinations (symmetric and antisymmetric) of these $2p_z$ bonds also form a bonding (π) and an anti-bonding orbitals (π^*) in the molecule. As compared to the σ-bonds forming the backbone of the benzene molecule, the π-bonds are significantly weaker. Electrons in π-bonds are therefore capable of delocalising around the entire ring. The energy levels of the molecular orbitals are $\sigma^* > \pi^* > \pi > \sigma$. In molecules, the highest occupied molecular orbital is called HOMO and the lowest unoccupied molecular orbital is called LUMO. They correspond to the π and π^* orbitals, respectively, and are equivalent to the valence band and conduction band of inorganic semiconductors.

Likewise, the energy difference of HOMO and LUMO is taken to be the band gap of a organic semiconductor.

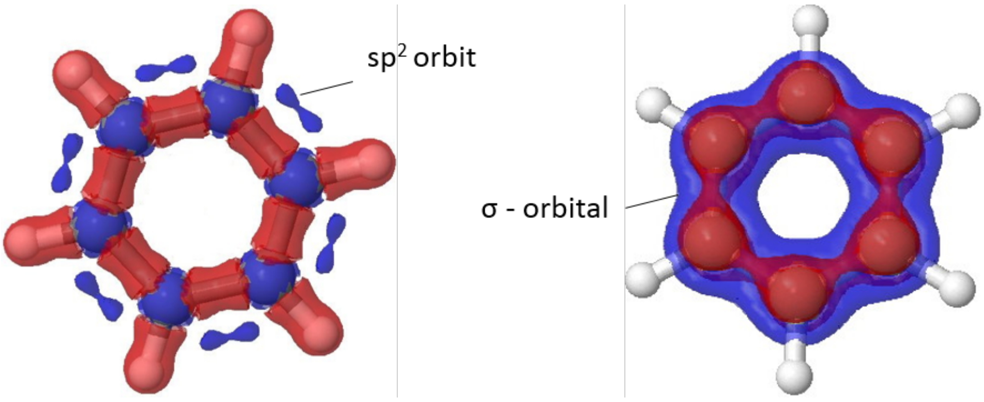

Figure 1.2: The formation of σ-bonds and σ-orbital in a benzene ring.

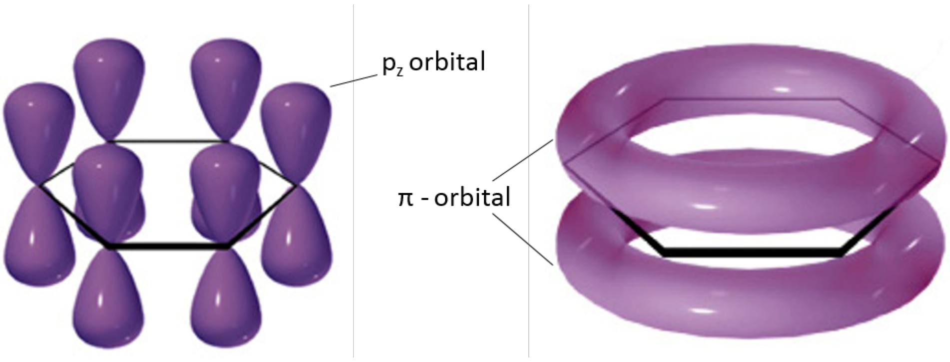

Figure 1.3: The formation of π-bonds and π-orbital in a benzene ring.

1.1.2 Comparison of organic and inorganic semiconductors

In comparison to its inorganic counterparts, organic semiconductors possess different optical and charge transport properties. This is directly due to the different bonding nature between these two types of material. Atoms of inorganic semiconductors such as Si and GaAs are coupled by strong covalent bonds. This results in well-defined conduction and valence bands where electrons and holes can transport freely in inorganic semiconductors, giving high charge mobility typically $> 10\ \mathrm{cm^2V^{-1}s^{-1}}$. For organic semiconductors, although atoms within a molecule are coupled by strong covalent bonds, molecules are coupled by considerably weaker Van der Waals force. As a result, electrons are allowed to move freely in each molecule, but the movement between different molecules is limited. This is called the weak delocalisation nature of electron wavefunctions in organic semiconductors, giving very low charge mobility typically < 1 $cm^2V^{-1}s^{-1}$ [8] in organic amorphous and 1 - 10 $cm^2V^{-1}s^{-1}$ in organic crystals [9]. In addition, owing to the weak electronic delocalisation, organic semiconductors can generate Frenkel exciton. Electrons and holes are confined to one single molecule, therefore have a considerable bonding energy of 0.5 to 1 eV.

1.1.3 Charge carrier transport

There are two extreme types of charge carrier transport in solids, band transport and hopping transport [10].

In band transport, the carriers move as a highly delocalised plane waves in a broad carrier band with a mean free path that is much larger than the nearest neighbour distance. This type of transport occurs mainly in crystals featuring delocalised charge carriers. In an idea crystal, shown as the straight line of figure 1.4 (a), a charge carrier is completely delocalised and it moves without scattering. In a real crystal, there are always lattice vibrations or phonons that disrupt the symmetry of the crystal. This disruption can be depicted as a energy peak shown in figure 1.4 (a). These defects scatter the charge carriers and therefore decrease their mobility. Lowering the temperature can reduce the lattice vibration, which can thereby increase the carrier mobility. As a characteristic feature, the temperature dependence of band transport follows a power law behaviour shown in Eq. 1.1.

$$\mu \propto T^{-n}, \quad n > 1 \tag{1.1}$$

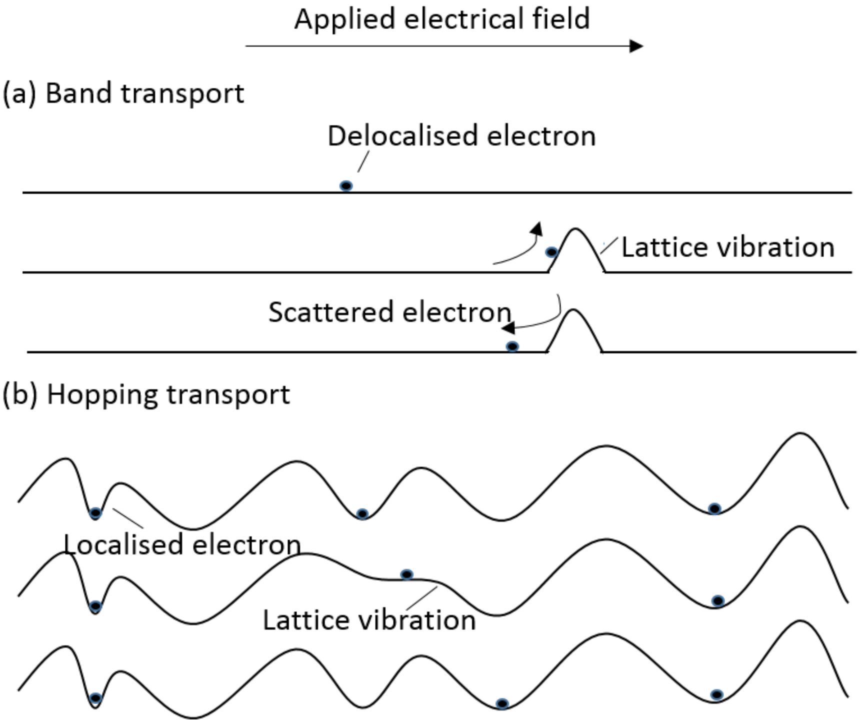

Figure 1.4: A simplified diagram showing the processes of band transport and the hopping transport in solid materials.

In hopping transport, the charge carriers are highly localised and move via hopping from site to site, being scattered almost at every site shown as in figure 1.4 (b). This type of transport occurs mainly in materials with high energetic and positional disorder caused by vacancies, dislocations and grain boundaries. The charge carrier transport of amorphous organic materials fall into this category. As can be seen in figure 1.4 (b), the charge carriers are localised on sites or in a potential well caused by the polarisation of the lattice by the charge carriers. The lattice vibration plays an important role while the charges are moving from site to site. This process is thereby an thermally activated process and the mobility increases with increasing temperature. Eq. 1.2 is an empirical function showing the dependence of mobility on temperature and electrical field, where μ_0 is a hypothetical mobility at infinite temperature and zero electric field, F is the electrical field, σ is the energetic disorder parameter, Σ is the positional disorder parameter, C_0 is an empirical constant, and k_B is the Boltzmann constant [11].

$$\mu(F,T) = \mu_0 \, e^{-(\frac{2\sigma}{3k_BT})^2} e^{C_0\sqrt{F}(\sigma^2-\Sigma^2)} \tag{1.2}$$

1.1.4 Material categories

There are two major groups of organic semiconductors, small molecular weight materials and polymers. These two types of organic materials differ mainly in their weight and the method of device production. Small molecules are often insoluble hence devices are fabricated via thermal evaporation. In contrast, polymers are usually soluble hence devices can be fabricated using solution via techniques like spin coating or inkjet printing. In comparison to thermal evaporation, solution techniques are easier to process and have the potential of producing larger area devices, which makes polymers a much more promising category in future application. Another advantage of polymers is that the wavelength of light emitted from polymers can be tuned by tailoring the conjugation length of the polymers. Tris(8-hydroxyquinoline)aluminium (Alq_3), N,N′-Bis(3-methylphenyl)-N,N′-diphenylbenzidine (TPD), N,N′-Di(1-naphthyl) -N,N′-diphenyl-(1,1′-biphenyl)-4,4′-diamine (NPB), Copper phthalocyanine (CuPc) and Fullerene (C_{60}) etc. are small molecular materials and PPV (poly-p-phenylenevinylene), poly (3,4-ethylenedioxythiophene)–poly (styrenesulfonat) (PFO), poly(3-hexylthiophene) (P3HT) and poly[2-methoxy-5-(2′-ethylhexyl- oxy)-p-phenylenevinylene] (MEH-PPV) etc. are polymers commonly used in organic electronics. Figure 1.5 shows some structures of the materials mentioned above.

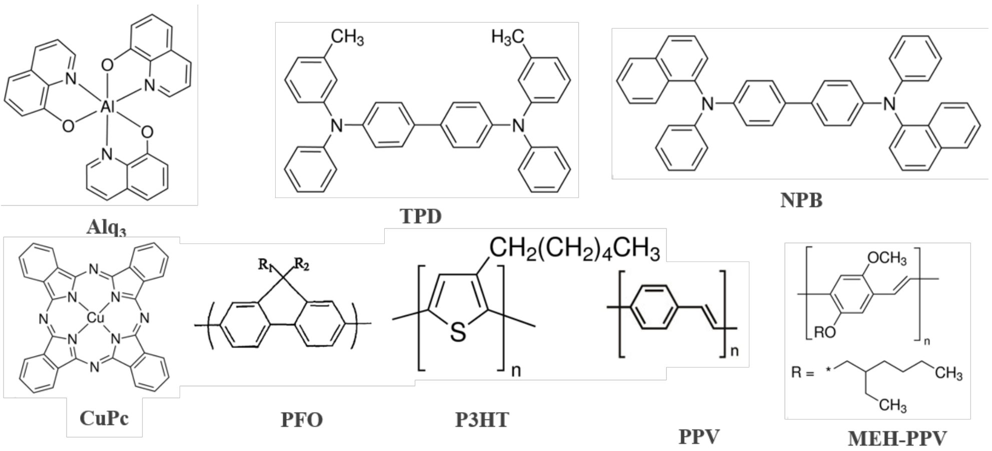

Figure 1.5: Chemical structures of some organic semiconductors, of which Alq$_3$, TPD, NPB and CuPc are small molecules while PFO, P3HT, PPV and MEH-PPV are polymers.

1.2 Introduction to organic light emitting diodes (OLEDs)

An OLED is a device with one or more organic layers sandwiched between two electrodes. Early works on OLEDs can be dated back to 1963 when a single layer of anthracene crystal with a thickness of 10-20 μm was used [12]. These devices featured drive voltages as high as 400 V, which is mainly due to the large thickness of the active material and partly due to the mismatch of work function of the organic crystal and the electrodes . The high drive voltage made the power conversion efficiency of these devices quite low, typically less than 0.1%, which hindered their development and commercialisation. The development of OLEDs was considerably advanced after 1987 when Tang et al. designed a double layer device with diamine as the hole transport layer and Alq$_3$ as the emitting layer [1]. The major breakthrough of devices with this structure was achieving much reduced operation voltage and much higher light output by assigning different roles to different materials. The drive voltage was successfully reduced to below 10 V, the highest brightness was $\sim$ 1000 cd/m ^{2}, and the efficiency was hence improved to 1%. Since then, OLEDs have received significant research interests and have successfully been used for commercial applications, such as smart-phones, television screens and digital cameras etc. In addition, the importance of OLEDs research is also valued in its possibilities of understanding charge transport and photo-physics in organic semiconductors.

1.2.1 Working principles of a modern OLED

A modern OLED consists of at least two organic layers. In this section, a device with double organic layers is used to explain the working principle of an OLED. Figure 1.6 shows the energy diagram of an OLED with the structure of ITO/TPD (50 nm)/Alq$_3$ (50 nm)/Al (100 nm) under no bias. The Fermi energy (E_F) of the ITO and the Al electrodes are 4.9 eV and 4.3 eV respectively. The lowest unoccupied molecular orbital (LUMO) and the highest occupied molecular orbital (HOMO) of TPD are 2.55 eV and 5.5 eV. The LUMO and the HOMO of Alq$_3$ are 3.05 eV and 5.8 eV. ITO acts as anode, Al acts as cathode, TPD acts as hole transport layer, Alq$_3$ acts as electron transport and light emitting layer.

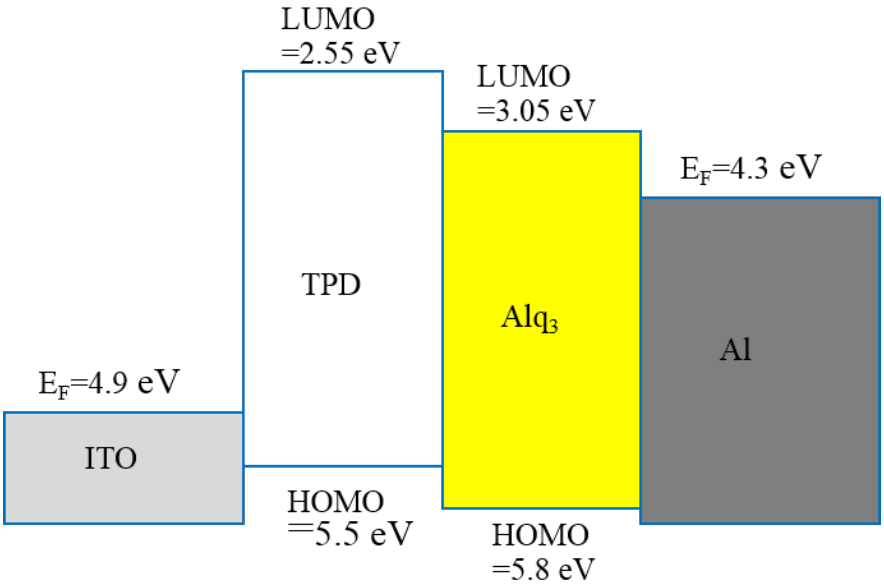

Figure 1.6: Energy diagram of a device under open circuit condition (no electrical connections between the electrodes). It shows the Fermi energy of electrodes and the HOMO and the LUMO energy of organic molecules.

When the ITO and the Al are connected by a positive bias, holes will be injected into the TPD layer from the positively biased ITO, while electrons will be injected into the Alq$_3$ layer from the negatively biased Al. Injected holes and electrons therefore migrate toward each other driven by the electric field and meet at the TPD/Alq$_3$

interface where excitons are generated and light emission occurs, to be discussed in section 1.2.2 in detail.

1.2.2 Charge carrier injection

There are two ways for charge carriers to be injected into organic layers from electrodes, thermal emission and tunnelling. The injection possibility of both processes depend strongly on the barrier height of each interface. There are four energetic barriers in the device presented in figure 1.6. Barriers in ITO/TPD interface and TPD/Alq$_3$ interface hinder holes to be injected into TPD from ITO and into Alq$_3$ from TPD. Barriers in Al/Alq$_3$ interface and Alq$_3$/TPD interface hinder electrons to be injected into Alq$_3$ from Al and into TPD from Alq$_3$. The barrier heights for hole injection are, ideally, the difference of the E$_F$ of ITO and the HOMO of TPD, and the difference of HOMOs of TPD and Alq$_3$. Likewise, the barrier height for electron injection are the difference of the E$_F$ of Al and the LUMO of Alq$_3$, and the difference of the LUMOs of Alq$_3$ and TPD. As can be seen in figure 1.6, the barriers for hole injection are smaller than that for electrons. At room temperature, the thermal energy is approximately 0.026 eV, which is small compared to the barrier height at the interfaces. As a result, charge carriers cannot achieve enough thermal energy to escape from the electrodes. There is, however, a finite possibility for charge carriers to tunnel through the energetic barrier. The possibility of tunnelling can be enhanced by electrical field strength.

Under short circuit condition, the energy levels of the device will realign so that the Fermi level of ITO and Al equalise. A simplified energy diagram of the device under short circuit is depicted in figure 1.7(a). This introduces a built-in potential gradient in the HOMOs and LUMOs of the organic materials. Ideally, the built-in potential (V_{bi}) is equal to the difference of the Fermi energy of these two electrodes, which, in this case, is 0.6 eV. Upon tuning the bias from small positive value to large positive value, the potential gradient will become increasingly flat, and eventually invert to the opposite direction, as shown in figure 1.7(b). During this process, a flat band condition occurs when the applied bias (V_{ap}) is just large enough to cancel out the built-in potential ($V_{ap} = V_{bi}$). Under flat band condition, there is no electric field across the organic layers. The energy alignment at the flat band condition is the same as the alignment when there is no connection between the electrodes (shown in figure 1.6). When V_{ap} is larger than the V_{bi} (shown in figure 1.7(b), triangular energetic barriers occur in each interface. The larger the V_{ap} is, the narrower the triangular barriers become. The possibility for charge carriers to tunnel into the other side of the barrier increases as the triangular barrier become narrower. Charge carriers can, therefore, tunnel through the thin triangular barrier into the organic layers.

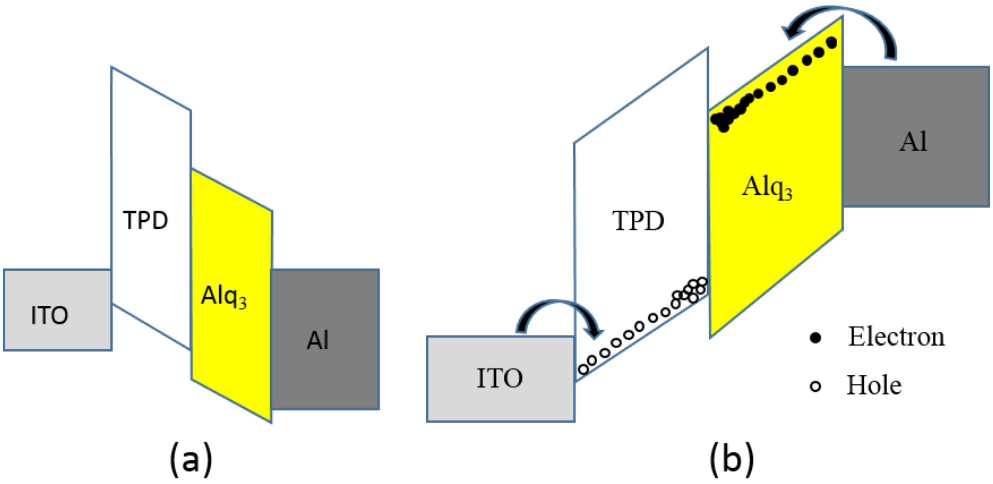

Figure 1.7: Energy level alignment of a device with the structure of ITO/TPD/Alq_3/Al under short circuit condition (a) and under large forward bias (b).

Electrons injected into Alq_3 from the Al cathode will hop toward the Alq_3/TPD interface driven by the electric field across the device. Similarly, holes injected into TPD from the ITO anode will hop toward the TPD/Alq_3 interface. Due to the large difference in the LUMOs of Alq_3 and TPD, it is almost impossible for electrons to be injected into TPD from the Alq_3/TPD interface. As a result, some electrons will accumulate at Alq_3 side near the interface. Conversely, owing to the relatively small difference in the HOMOs of TPD and Alq_3, some holes can overcome the interface barrier and be injected into Alq_3 from the TPD/Alq_3 interface. Those injected holes recombine with electrons in the Alq_3 layer and emit green light. However, due to the existence of the interface barrier and much smaller hole mobility in Alq_3 than in TPD, some holes accumulate at both sides of the TPD/Alq_3 interface. The value of V_{ap} when the current starts to increase rapidly over several order of magnitudes is defined as the turn on voltage for current.

1.2.3 Exciton formation

An exciton is an excited state consisting of an electron and a hole. Generally, there are three types of excitons: Frenkel exciton, Wannier-Mott exciton and charge-transfer exciton. Figure 1.8 shows the structures of the three types of excitons. The electron and the hole of a Frenkel exciton sit on the same molecule (for small molecular OS) or on the chain wthin a conjugation length (for polymer OS). The electron and the hole of a Wannier-Mott exciton sit several molecules apart. A Wannier-Mott exciton is also considered as a precursor to Frenkel exciton in electroluminescence. Both of them are believed to play important roles in magnetic field effects (MFE) on organic semiconducting systems (to be discussed in section 1.3). The electron and the hole of a charge-transfer exciton sit on the nearest molecules of different type. The electron and hole of an exciton is bound by the Coulomb force. Due to their small dielectric constant, organic materials possess predominantly Frenkel excitons. In comparison, charge-transfer excitons mainly appear in doped organic systems or at a interface where there is too large a electrostatic barrier to get the electron and hole onto the same molecule. There are two major methods of generate excitons: electrical excitation and optical excitation.

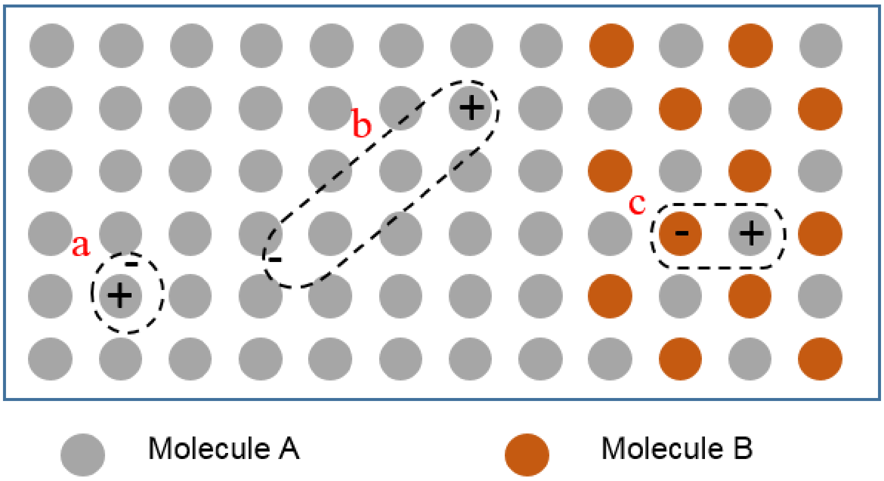

Figure 1.8: Schematic showing three types of excitons: a.) Frenkel exciton; b.) Wannier-Mott exciton; c.) Charge-transfer exciton.

Electrical excitation relies on the injection of electrons and holes from the electrodes. Once electrons and holes meet in the emitting layer, excitons are formed spontaneously and light emission occurs accordingly. Owing to the random spin orientations of the injected charges, the formed excitons possess one of the four possible configurations, shown as in figure 1.9. The net spin for the first configuration is 0 and the net spin for the remaining three configurations is 1. Therefore, excitons having the first configuration are called singlets and the other three are called triplets. Due to the Pauli Exclusion Principle, singlet excitons are spin favourable states for recombination and are capable of radiative decay to the ground states in short time scale (nanoseconds) [13]. Light emitted from singlet excitons is called fluorescence. Triplet excitons are 'spin forbidden' states and usually relax to ground states through a non-radiative pathway in a slower time scale (microseconds) [14]. Radiative decay can, however, occur in triplet excitons formed in organic materials containing heavy metals where the spin-orbit coupling is strong enough to alter an electron spin state so as to overcome the forbidden nature of the transition. Light emitted from triplet excitons is called phosphorescence, which is an active research area in phosphorescence OLED [15, 16].

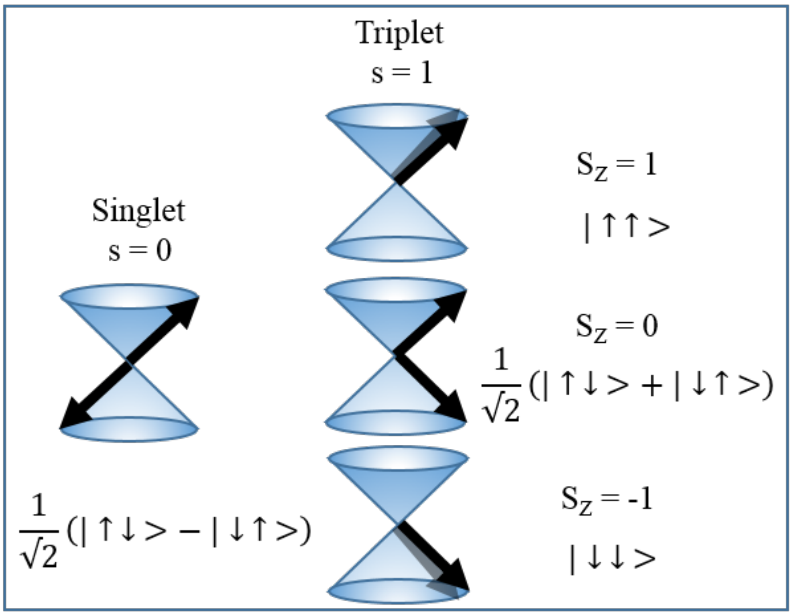

Figure 1.9: Schematic showing singlet and triplet configurations.

Optical excitation, also known as photoexcitation, is the process of forming excited states via the absorption of photons. Figure 1.10 demonstrates some of the main processes occurring in the optical excitation process. Electrons in ground states (S_0) absorb photons from a pumping source, usually a laser, and jump to a higher energy state (excited state, S_1, S_2 ...). The excited electron and the hole left behind forms a Frenkel exciton. Due to the spin conservation rules, defined by the Pauli Repulsion Principle, excitons formed at this stage are originally of a singlet configuration. Let's call it singlet. Singlets then relax to the lowest energy state of S_1 via internal conversion and vibrational relaxation. From this stage on, they can decay to the ground state radiatively, emitting fluorescence, or non-radiatively. Alternatively, they can transfer to triplets via a process called inter-system crossing. Similarly, these triplets relax to their lowest excited state (T_1) first and then decay radiatively or non-radiatively. It is worth noting that for the absorption to happen, the energy of the photons generated by the laser must be higher than the lowest energy for S_1 state. Also, the intersystem crossing rate can be affected by internal factors like specific material properties, whether or not containing heavy metals, for instance, or external properties like applied magnetic fields (to be discussed in section 1.3). Luminescence achieved via photoexcitation is called photoluminescence (PL). It provides a useful technique of measuring the lifetime of singlets in materials.

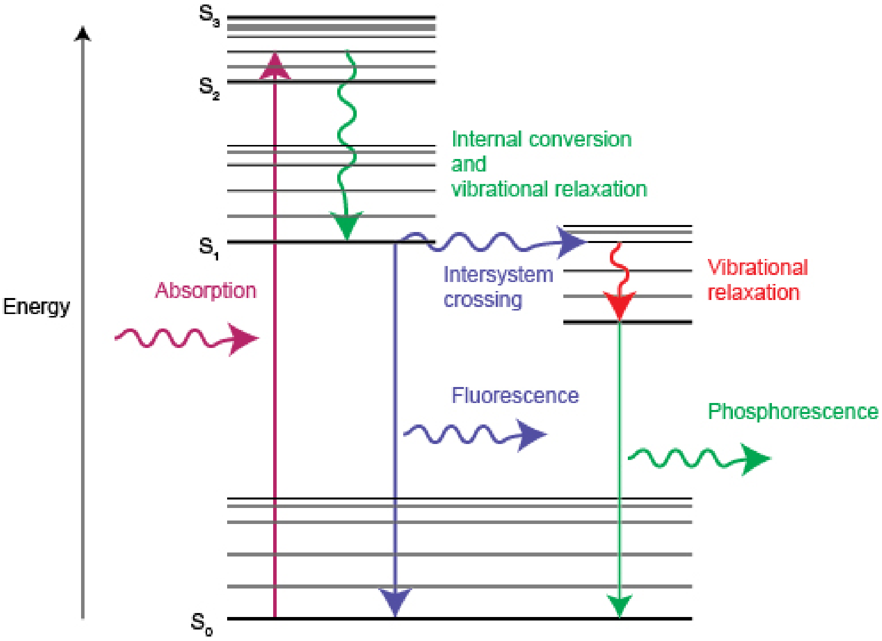

Figure 1.10: Schematic showing the photoexcitation process.

1.2.4 Processes that could affect the efficiency of an OLED

Efficiency is one of the important characteristics for showing the performance of an OLED and can be defined in several ways. The quantum efficiency is most generally used to describe the performance of an OLED. It can be divided into internal quantum efficiency (η_{IQE}) and external quantum efficiency (η_{EQE}). The internal quantum efficiency is defined as the ratio of the number of exciton radiative decayed (N_{rad}) to the total number exciton formed (N_{tot}), which demonstrates that not every exciton can generate photon.

$$\eta_{IQE} = \frac{N_{rad}}{N_{tot}} \tag{1.3}$$

Likewise, not every photon generated can find its way out of the device, as a result, the ratio of the number of photon coupled out of the device (N_{out}) to the total number of photon generated is called the out-coupling factor (γ).

$$\gamma = \frac{N_{out}}{N_{tot}} \tag{1.4}$$

The external quantum efficiency is therefore the product of internal quantum efficiency and the out-coupling factor, which is essentially the ratio of the number of photon collected to the total number of exciton formed.

$$\eta_{EQE} = \gamma \eta_{IQE} \tag{1.5}$$

There are other efficiencies: the current efficiency ($\eta_{current}$), defined as the ratio of the brightness in candelas to the current in ampere,

$$\eta_{current} = \frac{brightness}{current} \tag{1.6}$$

the luminous efficiency ($\eta_{luminous}$), defined as the ratio of the brightness in candelas to the power of light output in watts,

$$\eta_{luminous} = \frac{brightness}{output\ power} \tag{1.7}$$

and the power efficiency (η), defined as the ratio of the output power in watts to the input power (product of the current (I) and voltage (V) across the device) in watts.

$$\eta = \frac{output\ power}{IV} \tag{1.8}$$

It is worth noting that the efficiency used in the discussion of the rest of this work refers to the power efficiency. It quantifies how efficient a device is at utilising the injected charge carriers.

Many processes could occur in the active layer of an OLED during its performance, each of them are capable of modulating the number of singlets generated, therefore changing the efficiency of the OLED. To make it easier to describe these possible processes, a schematic is presented in figure 1.11. Ideally, electrons and holes injected from electrodes are well separated in the first place, so they are called free electrons and holes. Under the driving force of Coulomb attraction, electrons and holes bind to each other, forming electron-hole pairs (it was called Wannier-Mott exciton in the last section) with both singlet and triplet configuration at a rate of 1:3 according to random statistics [17, 18]. Electron-hole pairs at this stage are referred as singlet polaron pair (^{1}(e+h)) and triplet polaron pair (^{3}(e+h)). These polaron pairs further form singlet and triplet excitons accordingly via hopping of electron (hole) onto

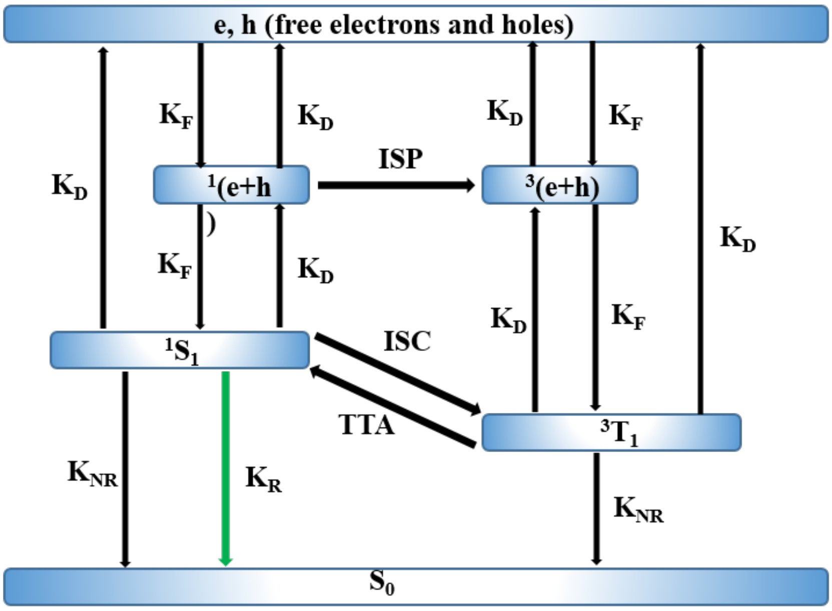

^{1}(e+h) : Singlet polaron pair (electron-hole pair possess anti-parallel spin configuration).
^{3}(e+h) : Triplet polaron pair (electron-hole pair possess parallel spin configuration).
$^1S_1$: First excited singlet states.
$^3T_1$: First excited triplet states.
S_0 : Ground state.
K_F : Formation rate.
K_D : Dissociation rate.
K_{NR} : Non-radiative decay rate.
K_R : Radiative rate.
TTA : Triplet-triplet annihilation.
ISP : Intersystem conversion between singlet and triplet polaron pairs.
ISC : Intersystem crossing between singlets and Triplets.

Figure 1.11: Diagram showing all possible processes that could occur in a working OLED.

the same molecule of the hole (electron). Singlet excitons ($^1S_1$) can then undergo a radiative process returning to ground state, and fluorescing. One should note that not all S_1 states recombine radiatively to generate photon except for materials with 100% internal quantum efficiency. In most materials, excitons can recombine non-radiatively as shown in figure 1.11. Triplet excitons ($^3T_1$) undergo non-radiative process and return to ground state (S_0), giving no light emission. However, in a real device, aside from forming corresponding excitons, polaron pairs are also subject to a dissociation process, through which they become free electrons and holes. Similarly, singlets and triplets can dissociate into corresponding polaron pairs or even into free electrons and holes. The driving force behind the dissociation processes in each stage can be an electric field across the device, trapped charges, interfaces and even excessive free charges. Like triplet excitons, singlet excitons can undergo the non-radiative route also. Apart from processes that happen purely in singlet or triplet branches, possible intersystem crossing is also believed to occur between singlet and triplet polaron pairs as well as singlet and triplet excitons. The driving force behind this is thought to be random hyperfine fields [19], but any spin mixing processes, e.g. spin-orbit coupling, would do the same. Also, it is possible for two triplet excitons to annihilate with each other to generate a singlet exciton and a ground state [20, 21].

Every process can potentially influence the efficiency of an OLED. The balance of free electrons and holes directly affects the formation rate (K_F) of singlet polaron pairs, hence the number of singlet excitons and eventually the efficiency. Singlet exciton formation rate is modified by dissociation processes in each stage, intersystem crossing processes between pair states and exciton states, and the triplet-triplet annihilation process. Since many of these processes are believed to be magnetic field sensitive, the singlet exciton concentration is also sensitive to external magnetic field. The effect of an external magnetic field on intersystem crossing is to modify the singlet/triplet ratio, hence the light output. Additionally, the changing singlet/triplet ratio indirectly affects light output through other processes involving interactions with singlets and triplets. This provides a useful tool to get insight into the processes in a working device by monitoring the effect of magnetic field on the efficiency of the device.

1.3 Magnetic field effects on OLEDs

It has been widely observed that an external magnetic field is capable of perturbing the current and luminescence of an OLED during its operation [22–27]. Indices such as current, luminescence, resistance, efficiency and voltage are usually used to describe the performance of an OLED. As a result, a change in each index (X) with and without magnetic field is referred as the magnetic field effects (MFE). They can be calculated using Eq. 1.9. In this section, a brief history of the MFE will be introduced chronologically by giving some of the main experimental results observed and experimental techniques used. Proposed models are then discussed in detail.

$$MFE = \frac{X(B) - X(0)}{X(0)} \times 100\% \tag{1.9}$$

The MFE investigated are most on current, resistance, luminescence and efficiency. The MFE on current are referred to as magnetoresistance (MR) [28–30], organic magnetoresistance (OMR) [31–33] and magneto-conductance (MC) [26, 27] by different research groups. The MFE on resistance are also referred to as magnetoresistance (MR) [34] and organic magnetoresistance (OMR) [35, 36]. In order to avoid confusion in the discussion of the current thesis, the MFE on current will be called MC and the MFE on resistance will be called MR. The MFE on luminescence is called magneto-luminescence (MEL).

1.3.1 Brief introduction

The history of MEFs on organic semiconducting system can be roughly divided into two stages. The early stage from 1960s when research of MFEs was focused on organic crystals, and the modern stage from 2003 where most researches were focused on modern OLEDs. A chronological introduction of the first stage is given, focusing on experimental results and theories. Discussion of the modern stage research will focus on key experimental phenomena and some widely accepted conclusions from the literature.

In the 1970s, MFEs in crystal anthracene and tetracene systems were intensively studied by applying the methods of photo excitation and delayed fluorescence. In 1967, Johnson and Merrifield [20] found remarkable effects of magnetic fields on the intensity of delayed fluorescence in anthracene crystals at room temperature. They observed that the intensity of delayed fluorescence, resulting from triplet-triplet annihilation (TTA), increases up to a maximum of 5% at a weak magnetic field of 35 mT and then decreases gradually at higher fields, finally levelling off at 80% of its original value for $B \geq 500$ mT. They also found that the magnitude of the high field effect was a function of the relative direction between the field and the crystal axes. After excluding the possibility of magnetic field effects upon the absorption coefficient, the emission from prompt singlet states and the triplet lifetime, a magnetic field dependent rate of the TTA was suggested to be responsible for the observed phenomenon.

To explain the magnetic field modification of the TTA rate, a paper by Merrifield [21] presented a theory involving spin Hamiltonian terms for a triplet exciton. The general idea of the theory is that, when there is no magnetic field, only three triplet pairs out of nine possible triplet pairs have singlet component. After the field is turned on, triplet pairs begin to mix, producing additional triplet pairs possessing singlet component. As a result, more TTA occurs, which naturally leads to an increase in delayed fluorescence intensity. However, at the high field region, due to large Zeeman splitting, spin states are quantised along the field and only two triplet pair states have singlet component. Thus in the high field limit, there are fewer singlet states than at zero field, leading to a decrease in the delayed fluorescence intensity.

MFEs in X-Ray irradiated anthracene system were also investigated by Merrifield in 1968 [37]. It was believed that paramagnetic centres introduced by low dosages of X-Ray irradiation act as quenchers for triplet excitons. Triplet lifetime in the irradiated anthracene was measured with and without a magnetic field. Results showed increased triplet lifetime when the experiment was conducted with a magnetic field. The authors attributed this phenomenon to a magnetic field dependence of triplet quenching rate. Their qualitative explanation was similar to what was discussed in MFEs on triplet-triplet annihilation [21]. They thought that the interaction between a triplet exciton and a free radical (paramagnetic centre) can result in two outcomes: scattering which is spin selection independent and quenching which is spin selection dependent. They suggested that the maximum quenching rate is at zero field.

MFEs on photo-physics of dye sensitised anthracene were investigated in 1972 by Groff et al [38]. Like the work carried out by Merrifield in non-sensitised anthracene, it was found that under an applied magnetic field, the intensity of delayed fluorescence firstly increases and then shows a monotonic decay towards saturation. This phenomenon, observed in dye sensitised anthracene, was obtained at a much lower magnetic field, the maximum intensity occurred at 0.3 - 0.7 mT whilst saturation occurred at 20 - 30 mT. Hyperfine field induced singlet and triplet mixing was claimed to be the reason for the observed phenomenon.

In 1975, the first example of MFEs on delayed fluorescence using electrical excitation was investigated by M.Wittmer et al. in the University of Basel [39]. They studied the triplet trapped charge carrier interaction and singlet trapped charge carrier interaction with and without the presence of a magnetic field. To remove the effect due to the free charge carriers, a high voltage supply was firstly used (to give a forward bias and inject charge carriers). Then, the forward bias was substituted with a reverse high voltage to remove free charge carriers in the bulk of the crystal. As a result, only bounded excitons and trapped charge carriers remained in the bulk. It was found that trapped charge carriers could quench triplet excitons through examining the intensity of delayed fluorescence. This was attributed to the dissociation of triplet pairs in the presence of charge carriers.

These early works give good examples about how magnetic field could affect exciton populations and exciton charge carrier interactions within organic materials. It forms some of the backbone of the theories used in modern research. However, these works were mostly focused on the delayed fluorescence technique and remained largely undeveloped.

The next stage of research on MFEs in organic systems started from 2003 when Kalinowski [19] performed field dependent measurement on modern OLED devices. He reported an increase in the electroluminescence quantum efficiency up to 3% and an increase in device current up to 2.5% when an external field of $\sim$ 500 mT was applied to an OLED with the structure of ITO/TPD:PC/Alq_3/Ca/Ag. His results started a new era of MFE research. From then on, research groups worldwide started to investigate MFEs on OLED devices by changing various aspects: the electrodes [29, 40, 41], the material of active layer [42], the performance temperature [43–47], material thicknesses [28, 48], doping the active layer [24, 49–52], modulating the hyperfine and spin-orbital coupling strength of the active layer [41, 53–55], electrically stressing the device [35, 36], and so on.

Owing to the large number of experiments conducted, various phenomena in MC and MEL have been found depending on the structure of the device and the measuring conditions. The MC can be both positive and negative and even transient from negative to positive [56–59]. The MR should show an opposite feature to that of MC. The MEL are generally positive, showing rapid increase at low fields and saturating at higher fields, or keep increasing at higher fields with smaller rates [31, 60]. However, there is a small group of MELs showing rapid increase at low field regime while starting to decrease at the higher field regime [45, 49, 61, 62]. X-ray irradiation and electrical conditioning are found to increase the magnitude of MC [35, 36, 63]. On the contrary, devices with heavy metals show smaller or even vanishing magnitude of MC [64].

It has been established that there are low field (< 50 mT) components in MFEs which originate from the random hyperfine fields and spin-orbit coupling effects on the mixing of singlet and triplet excitons and polaron pairs [22, 23]. Another process with a higher field (< 50 mT) dependence is also been found in experimental results [30, 40, 48]. This component is deduced from the fitting of MFEs using Lorentzian functions [30, 48]. It has a higher saturation field and is thought to be responsible for the slower increase or decrease of MFEs in the high field regime. There is not yet direct evidence about the nature of this process, but experimental results suggest that it is related to triplet excitons in a device [30, 40, 48]. More details about how magnetic fields influence the mixing process and how this induces MFEs in a device are discussed in section 1.3.2.

1.3.2 Models used to explain MFEs

to explain MFEs can be categorised into two groups: the excitonic models [19, 28, 31, 34, 64] and the bipolaron model [32, 33]. Excitonic models attribute MFEs to magnetic field dependent interaction ratios between polaron pairs (electron-hole pairs, Wannier-Mott exciton) or excitons. In these models the occurrence of MFEs requires the presence of both electrons and holes in the device. In comparison, the bipolaron model attributes MFEs to the perturbation of magnetic fields on bipolaron formation probability. As a result, as long as there is at least one type of charge in the device, there could be MFEs. Details and discussions about these two types of model follow.

Exciton models

The excitonic model is the main stream of model being used to interpret the MFEs in organic systems. According to the literature, there are four possible processes that can be directly affected by magnetic fields. They are: (a), intersystem crossing between singlet and triplet polaron pairs; (b), intersystem crossing between singlet and triplet excitons; (c), triplet-triplet annihilation, and (d), triplet-charge carrier interaction. Processes (a) and (b) will be discussed first, and the discussion of (c) and (d) will then follow.

It is well established that interconversion between singlet and triplet states can occur, induced by hyperfine interactions between nuclei and the charge carriers [19]. Specifically, it is widely accepted that charge carriers in organic materials undergo precession about random hyperfine fields (B_{hf}) originated from atomic nuclei, which causes a certain degree of mixing between singlet and triplet pair states as well as singlet and triplet exciton states. The result of the mixing is that some transitions between singlets and triplets occur at both pair states and exciton level. The transition process is called intersystem crossing. Although the intersystem crossing happens in both directions (singlets -> triplets and triplets -> singlets), the final result is a increase in the triplet concentration because the energy level of triplet is lower compared to singlet. After applying an external magnetic field ($B_{ext)}$, the total field (B_{tot}) experienced by each charge carrier becomes the sum of B_{hf} and B_{ext}. As B_{ext} increases, the direction of B_{tot} is dominated by the direction of B_{ext}. The mixing between singlets and triplets in all levels is, therefore, completely quenched at large B_{ext}. This quenching process reduces the number of singlets converted to triplet states, hence the final result is an increase in the population of singlet states and a decrease in the population of triplet states.

The increase of singlet population is well supported by widely achieved positive MEL($\Delta EL/EL$) in experimental results [31, 60]. There are, however, different arguments in terms of how the change of the population in singlets and triplets affects the MR ($\Delta R/R$) or MC ($\Delta I/I$). A Nature paper from Bin Hu et al.[34] suggested that it is the dissociation of singlets that contributes to the negative MR whilst the interaction of triplet with charge carriers contributes to the positive MR. Figure 1.12 shows the schematic diagram of their arguments. K_{ISP} represents the intersystem crossing rate between pair states and K_{ISC} represents intersystem crossing in excitonic states. There are two points that should be clarified. First, negative and positive MR ($\Delta R/R$) are equivalent to positive and negative MC ($\Delta I/I$), respectively. Second, it was suggested that only K_{ISP} is magnetic field dependent. This assumption was based on their earlier experimental findings that showed samples measured under electrical excitation demonstrated significant MFEs whereas those measured under photo-excitation showed negligible MFEs [65, 66]. There is, however, evidence for field dependent intersystem crossing both in pair states and excitonic states. Chen et al. [67] found large MEL in charge-transfer (CT) state devices, where light is emitted through direct recombination of the CT states. This is direct evidence for the field dependent intersystem crossing in pair states. Zhang et al. [68] found that the intersystem crossing rate between singlets and triplets was increased by 10% at 80 K and at 100 mT measured under transient photo-excition. Among all the possible processes that could occur in a device, Hu et al. [34] assumed that there are two dominant processes that contribute to the device current through secondary charge carriers: those generated via singlet dissociation and those via triplet-charge carrier interaction. Specifically, they assume that the dissociation rate of singlets is larger than that of triplets; after applying an external magnetic field, the increase of the population of singlet causes a positive MC in the device whilst the decrease in triplet population causes a negative MC; the sign of the total effect is, therefore, a sum of those two effects which could be positive or

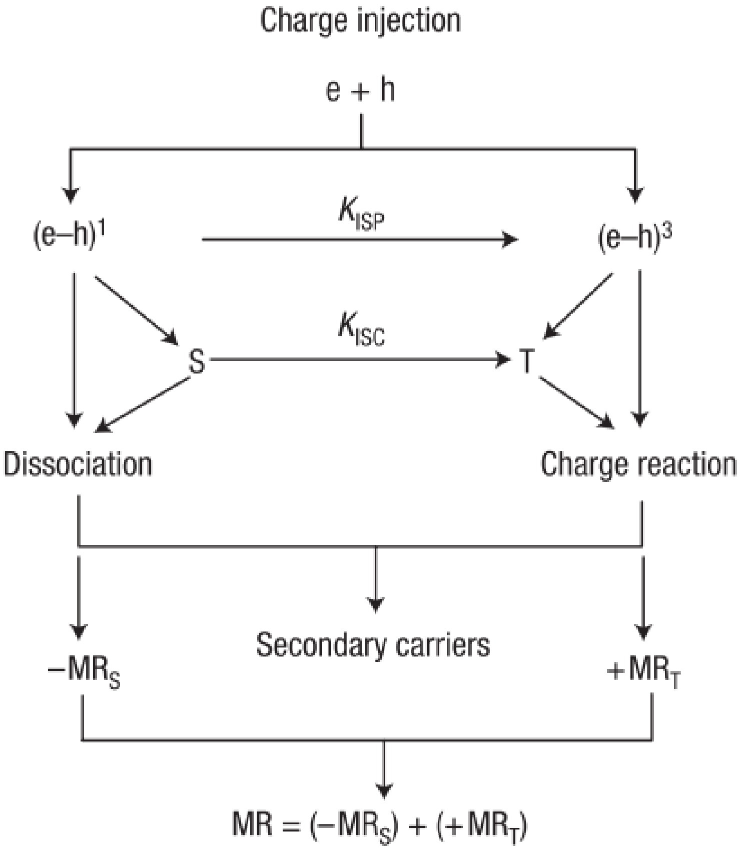

Figure 1.12: Schematic diagram showing the processes that contribute to the MR. This figure is reproduced from reference [34].

negative depending on which of the two processes dominate. It can be seen that an MC is purely a side effect of the relative change in the population of singlets and triplets. Their argument was supported by experimental results where they successfully adjusted the sign of MC from positive to negative via modifying the relative population of injected electrons and holes from balanced (singlet dissociation dominant) to unbalanced (triplet-charge carrier interaction dominant). There is a puzzle, however, concerning their assumption about the singlet and triplet dissociation rate where they cite two references [69, 70]. The first reference [69] assumed that the dissociation rate of singlets is far greater than triplets because singlets have a stronger ionic character where they cited the second reference [70]. According to reference [70], singlet exciton is ionic in nature whereas triplet exciton is covalent. In this paper, however, the terms 'ionic' and 'covalent' refer to an excited state where electron and hole are located on different sites or on the same site on the conjugated backbone, respectively. This doesn't seem to suggest that singlet should have a larger dissociation rate.

Desai et al. interpreted the effect of changes in singlet and triplet population on MR differently. In one of their works [29], they conducted MFE measurements on Alq_3 based devices with varied cathode materials. Three types of cathode, Al, LiF:Al, and Mg:Ag, with different work functions were used. Positive MC was found in these devices. For each device, there was a perfect correlation between the EL turn on voltage and the positive MC occurrence voltage. This gave strong evidence of the excitonic nature of MFE, which was further supported by experimental results found by Gärditz et al. [71] that no MR was observed in electron only devices. Desai et al. suggested that triplets play the dominant role in contributing to MC because there are a lot more triplets in a device due to their long lifetime [14] and 3 times larger formation rate compared to singlets. Inspired by early MFE studies of charge carrier effect on triplet lifetime conducted on anthracene crystal by Ern and Merrifield [72], they suggested that triplets can affect device current via blocking charge carriers. After applying an external magnetic field, the concentration of triplet decreased, hence the blocking effect is reduced and positive MC occurred. They stated that the argument that triplets play dominant role in MC was supported by experiments performed on phosphorescent dyes, tris(2-phenylpyridine) iridium ($Ir(ppy)_3$ and 2,3,7,8,12,13,17,18-octaethyl-21H,23H-porphine platinum (PtOEP), doped Alq_3 devices [64]. In these devices, triplets formed in Alq_3 were successfully removed by phosphorescence emission and much smaller MC was observed compared to that of a pure Alq_3 device. The problem, however, is that whether the reduced MC is due to reduced triplet concentration in the devices or a change of the local hyperfine field induced by the phosphorescent dyes is not clear. It is clear, though, that they didn't imply that the blocking process should have any field dependence. The MC observed is, therefore, a side effect caused by the field dependent triplet concentration.

Desai et al. in a later paper [28] extended the role played by triplets in MC. They performed MFE measurements on Alq_3 based devices by varying the thickness of the Alq_3 layer. Positive MC was found in thick devices, showing a rapid hyperfine field increase. They also noted that there is a linear MC increase at higher fields as the drive voltage was increased, in addition to the hyperfine effect. Negative hyperfine MC was found in thin devices (115 Å and 150 Å) at low drive voltages, showing a similar line shape as the positive hyperfine MC in thick devices. As the voltage was increased, similar positive MC occurred at high fields, which eventually caused a overall positive MR in these thin devices. Due to the similarity of the field dependence in the positive MC in thick devices and negative MC in thin devices, the negative MC was also attributed to the field dependent triplet concentration. The interpretation was that triplets can both block charge carriers and dissociate into free charge carriers, charge carrier blocking decreases the mobility of charge carriers hence reduces the current of the device, whereas triplet dissociation produces extra charge in the device hence increases the current of the device. After applying an external field, the concentration of triplets decreases, as a result, the charge trapping process produces a positive MC whilst the dissociation process produces a negative MC. The competition of the two decides the sign of the MC at the hyperfine field regime. Since the triplet dissociation rate is more significant at energetically favourable interfaces, the triplet dissociation probability is larger in thin devices, because the probability for triplets to diffuse and dissociate at the metal cathode is improved in thin devices. As a result, negative MC presented in the thin devices. As for the subtle linear increase seen in both thin and thick devices, they proposed a new process, triplet charge carrier interaction, to explain it. It was assumed that the interaction process is field dependent. To sum up, triplets can affect the current of a device mainly through three routes: site blocking, dissociation and triplet-charge carrier interaction. Site blocking refers to the situation where a charge carrier possesses the same spin orientation as the triplet in its neighbour molecule, the charge carrier cannot hop to that molecule due to the Pauli Exclusion Principle. After applying an external magnetic field, the population of triplets decreases, weakening the site blocking effect, increasing the charge carrier mobility, resulting in positive MC. On the other hand, decreasing triplet population decreases the amount of triplets that could potentially contribute to device current via dissociation, hence a negative MC may occur. However, little discussion was made on how the triplet-charge carrier interaction affect the current in a device except for the result that it contributes to positive MC.

The effect of triplets on charge carrier transport was tested by Song's work [73, 74]. He conducted mobility measurements in TPD using the dark injection method and found that hole mobility decreased when there are excitons in the device. More importantly, he found that hole mobility showed a small increase when measured under a magnetic field of 500 mT. MFE on charge carrier mobility has also been tested by Li et al. [75], using the transient EL method. They performed transient EL measurements with and without exposure to an external magnetic field and found that the EL arrival time remained the same in both conditions. They reached the conclusion that magnetic field has no effect on charge carrier mobility. However, it seems that they overstated their conclusion, because the EL arrival time only indicates the transit time for the fastest charge carriers which can only represent the mobility of those fastest charge carriers. The dark injection method measures the average mobility of the charge carriers. The two results don't contradict each other and therefore one cannot prove the other wrong.

Another process that has been widely discussed to be affected by external magnetic field is triplet-triplet annihilation (TTA). It is the situation when the total energy of two triplets is larger than the energy of a singlet, the two triplets can then undergo an annihilation process, producing a singlet and an excited ground state (S_0^*) as shown in Eq. 1.10. MFE on TTA was proposed in 1970s by Merrifield to explain his finding of MFEs on delayed florescence [20, 21]. The basic idea of how magnetic fields perturb the TTA process has been explained in 1.3.1. Since then, MELs with a line-shape increasing up to about 40mT and decreasing at higher fields are attributed to MFEs on TTA. Further discussion on TTA will be presented in chapter 3.

$$T_1(|\uparrow\uparrow>) + T_1(|\downarrow\downarrow>) = S_1(|\uparrow\downarrow>) + S_0^*(|\downarrow\uparrow>) \qquad (1.10)$$

The last process that has been proposed to be affected by external magnetic fields is the triplet-charge carrier interaction (TCI). The concept of TCI was used separately by Hu et al. [34] and Desai et al. [76] in their work to explain MR results. Hu et al. thought that TCI affect the current through secondary charge carriers generated by the TCI process. Since a magnetic field decreases the population of triplets, it weakens secondary charge carriers generated via the TCI channel, producing a negative MR. Desai et al. thought that TCI affects device current through a mobility channel because triplets can scatter charge carriers during their transport, hence reducing charge carrier mobility. An external magnetic field decreases the population of triplets, thereby increases charge carrier mobility, and generates a positive MC. In addition, Desai et al. also considered triplet exciton dissociation as a route to negative MC. It can be seen that in Hu's work, a magnetic field does not have a direct influence on TCI. The effect they proposed is purely a side effect of the magnetic field effect on the population of triplets originating from a magnetic field sensitive intersystem crossing process. However, experimental results later on indicate step by step that the TCI itself is a high field process.

In 2005, work led by Mermer etc. investigated MFEs on several semiconducting systems [31]. They achieved both positive and negative magnetoresistance (which is the MFEs on device resistance, having opposite sign compare to that of MFEs on device current). They suggested that MFEs are a universal effect in organic systems. More importantly, they normalised the magnetoresistance of different materials and found that there were two types of line-shape. Both of them present a rapid increase in the low field regime up to ~ 30 mT, with some tending to saturate at higher field while others keep increasing with a smaller rate showing no saturation. They proposed two empirical equations, a Lorentzian function is shown in Eq. 1.11 and a Non-Lorentzian function is shown in Eq. 1.12, to fit those two types of MFEs. They showed that the 'saturating' type of MFEs can be fitted by the Lorentzian function while the 'non-saturating' types of MFEs can be fitted by the Non-Lorentzian function. Figure 1.13 shows these two types of line shape generated from Eq. 1.11 and Eq. 1.12.

$$\frac{\Delta I}{I} = (\Delta I)_{max}(\frac{B^2}{B^2 + B_0^2}) \tag{1.11}$$

$$\frac{\Delta I}{I} = (\Delta I)_{max}(\frac{B^2}{(B + B_0)^2}) \tag{1.12}$$

$$MR = a_t(\frac{B^2}{B^2 + B_t^2}) + a_i(\frac{B^2}{B^2 + B_i^2}) \tag{1.13}$$

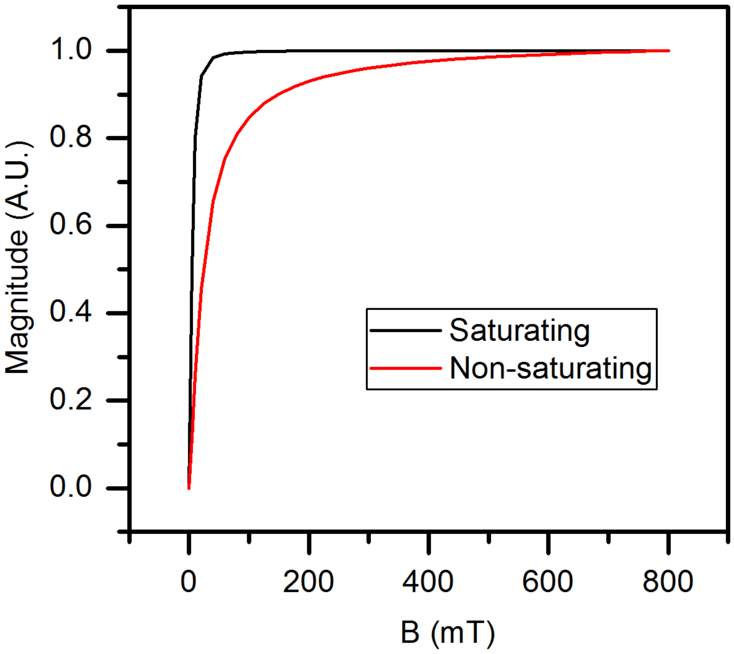

Figure 1.13: Saturating (black) and non-saturating (red) line shapes generated from Eq.1.11 and Eq.1.12 respectively.

In 2010, Gillin et al. extended the use of these two fitting functions [30]. They fitted the MFEs on the relative change of power efficiency ($\Delta\eta/\eta$) of an Alq$_3$ based device using the Lorentzian function, Eq. 1.11, and found that a B$_0$ of $\sim$ 5-7 mT gives sensible fitting to the $\Delta\eta/\eta$. They then used a combination of two Lorentzian functions, Eq. 1.13, to fit the MC data. They found that by confining the value of B_t of the equation to between 5 mT and 7 mT, the MC data can be fitted by the double Lorentzian function, giving the B_i of the second term a value of $\sim$ 160 mT. The low field term was attributed to the trapping effect of triplets on charge carriers and the high field term was attributed to the TCI process accounting for the slower rate of increase of MC in the high field regime. It should be pointed out that the trapping of charge carriers on triplets itself is not magnetic field dependent. It is a side effect caused by the field modification of the concentration of triplet via spin mixing. The TCI process, however, is expected to be field dependent. Zhang (2014) [40] at QMUL carried out MC measurements on devices based on Alq_3 with different degrees of balance between electrons and holes through modifying the electrodes of the devices. They found that the MC of devices with larger electron/hole ratio present larger rate of increase in the high field regime. Eq. 1.13 was applied to fit the results with the same confinement as that used by Gillin. Results showed that devices with bigger electron/hole ratios demonstrate nearly one order of magnitude higher strength in TCI terms, which suggests that in Alq_3 based systems electron trions play a more important role in TCI than that of hole trions.

Bipolaron Model

The Bipolaron model was firstly proposed by Bobbert et al. in 2007 [32]. Particles involved in this model are polarons and bipolarons. A polaron refers to a single charge residing on a site (molecule) whereas a bipolaron refers to a pair of charges with the same polarity residing on the same site (molecule). The model assumes that there are some energetically favourable sites that are permanently occupied by one charge. Those sites have two effects on charge carriers around them. A charge carrier sitting on a neighbouring site of a permanently occupied site can either hop onto the occupied site, forming a bipolaron if they have a spin anti-parallel configuration, or be blocked by this site if they have a spin parallel configuration. Under the parallel condition, those singly occupied sites can hinder charge transport in a device. However, due to the presence of random hyperfine field (B_{hf})

originated from nuclei, the direction of B_{hf} experienced by each charge carrier is different, which partially lift the blocking effect. The possibility of forming a bipolaron is actually higher than when there is no hyperfine field. After applying an external field (B_{ext}), the total field (B_{tot}) experienced by charge carriers become the sum of B_{hf} and B_{ext}. At large external fields, the direction of B_{tot} is dominated by B_{ext}, quenching the lifting effect brought about by B_{hf}, modifing the bipalaron formation ratio and consequently the MFEs. Figure 1.14 is a simplified diagram showing how the magnetic fields act on bipolaron formation. The way magnetic fields act on the spin mixing of singlets and triplets share a similar idea.

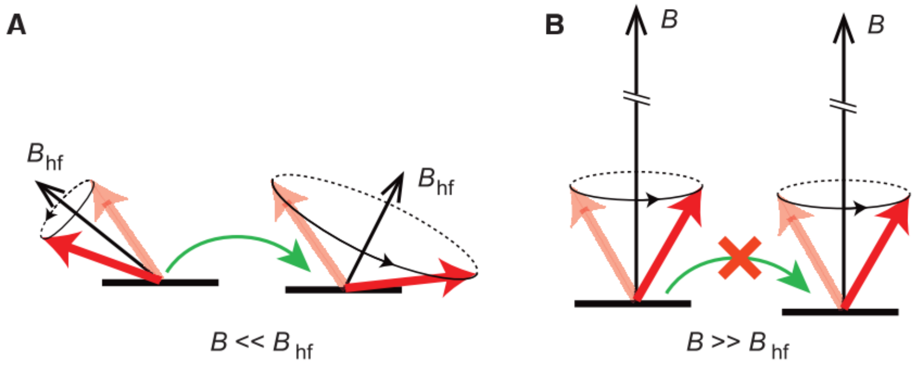

Figure 1.14: Schematic diagram showing the spin lifting (A) by hyperfine field and quenching of the spin lifting (B) by large external field. The figure is reproduced from ref [77].

Due to the quenching of the spin lifting effects by B_{ext}, negative MC should generally occur. However, authors claimed that under this model, MC of both positive and negative can occur depending on the branch ratio between the bipolaron formation or dissociation and hopping rate. Numerical Monte Carlo was employed to simulate MC in a cubic system with 9×10^3 sites. The bipolaron formation branch ratio, Random hyperfine field, Gaussian density of states, intrasite Coulomb repulsion and the Miller-Abrahams form of the hopping rate were included in the simulation. Both positive and negative MC were achieved by varying those model parameters.

Another paper released by the same group [33] extended the idea of the bipolaron model. The argument was the same except that they narrowed the system to a two-site scheme. Using Monte Carlo simulation, they also reproduced the main features of MC, such as the positive to negative sign change and characteristic line shapes. Based on the same principle, Kersten et al. [78] conducted analytical and numerical simulations of MFEs on polymers. They found that energetic disorder plays only a minimal influence on the spin blocking effect, whereas the inter-chain hoping rate holds a significant role. They then proposed potential conditions for achieving huge magnetoresistance effects: first, the charges should be localised on monomers and possess a hopping rate that is slower than the hyperfine precession rate, second, the conducting system should be essentially one dimensional so as to avoid inter-chain hopping. A year later, Mahato et al.[77] achieved such a system experimentally and observed MR as high as 2000% at room temperature, which confirmed the prediction of Kersten et al. and the suitability of the bipolaron model. Their system was formed by subliming an organic molecular dye, DXP (N,N′-bis(2,6-dimethylphenyl)- perylene-3,4,9,10-tetracarboxylic diimide), into the channels of zeolites. Since there are many thousands of electrically isolated channels in zeolites, a strict one dimensional system was formed. Figure 1.15 shows their experimented setup and material structure.

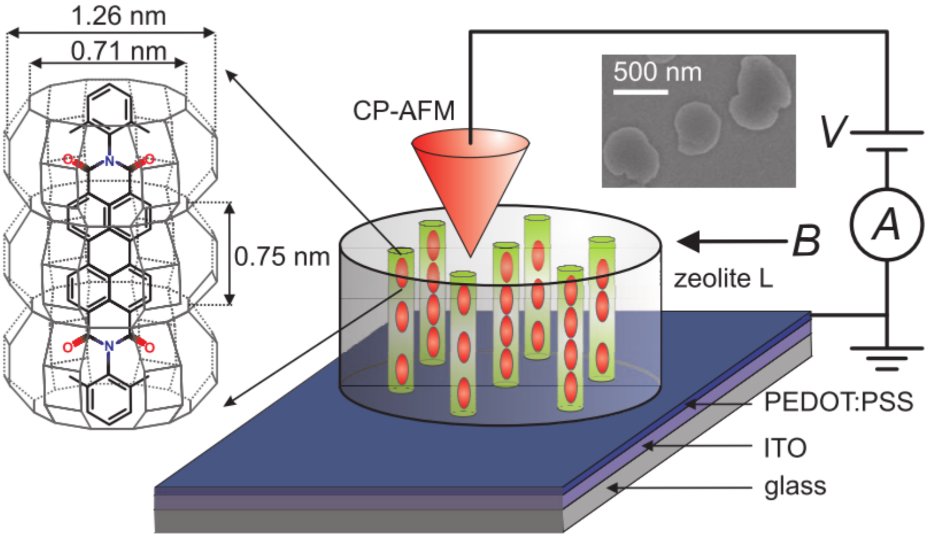

Figure 1.15: Experiment setup and material structure reproduced from ref [77].

Experimental evidence have been found to support the bipolaron nature and the excitonic nature of MFEs, and the existence of one does not exclude the other. In fact, it can be seen from the introduction of the models that the way an external field quenches the mixing between singlets and triplets is similar to the way it quenches the spin lifting of bipolaron formation. Both of them could coexist in one device and each dominates the MC behaviour under different conditions. Gu et al. [59] investigated the MFEs of a P3HT based device with the structure of Au/P3HT/Al. Under reverse bias, Au(-) and Al (+), negative MR was found. Since no excitons were formed or expected to form under this driving condition, the observed MR was explained using the bipolaron model. Under forward bias, Au (+) and Al (-), MC was observed to change from negative at low voltages to positive at high voltages. The sign transition point coincides with the turn on of luminescence. As a result, the negative MC was attributed to bipolaron formation whereas the positive MR was attributed the triplet charge carrier interaction. It is worth noting that the MC observed in this device is low, less than 0.5%. This might be due to the dimensionality (3D) of the organic material used, where the inter-chain hopping provides more routes for charge transport, thereby reducing the effect of bipolaron formation. This suggests that although bipolaron formation is one of the mechanisms for MC, its contribution to MC in general 3D organic material devices is small, excitonic mechanism is, therefore, widely used to interpret MFEs in ambipolar devices.

1.3.3 High field MFEs and their correlation to excitons

Section 1.3.2 has shown that both polaron pairs and excitons play important roles in MFEs. Polaron pairs account for the low field dependence in MFEs via random hyperfine mixing caused by atomic nuclei and spin-orbit coupling [55, 79–82]. Excitons appear to be both high field and low field dependent [76, 83]. The mechanism for low field dependence is the same as that of the polaron pairs, which have been widely studied and explored [84–86]. In comparison, the high field dependence was proposed relatively late, and hasn't been explored thoroughly. In this section, works that established the existence of the high field component will be firstly discussed. Following that, some experimental results that support the high field component and processes that were suggested to be responsible will be given.

The discovery of the high field process was in fact as early as that of the low field component [31], but at that time MFE showing the low field process was referred as a saturated line-shape whereas MFEs showing the high field process was referred as a non-saturated line-shape (figure 1.13). They were tentatively suggested to be an intrinsic property of the materials. In the paper published by Desai et al. in 2007 [76] they found that the MC of a 900 Å Alq_3 based device show both the saturated and unsaturated line-shapes as the drive voltage increases. That is the MC of low voltages shows a rapid low field increase with field, whilst the MC of higher voltages shows an extra, approximately linear, increases at high fields. A similar high field increase in MC was found in devices with various thicknesses although they showed different low field behaviour. Their results showed that several processes could contribute to the MC of a device depending on factors like the structure of the device, thickness, driving conditions etc. As the line-shapes can not be purely related to the property of the material, a different process mechanism must be dominate the high field MC. At that stage, they attributed this process to triplet-charge carrier interaction (TCI). The reason is that this high field increase occurred at high voltage, hence high current, and large number of triplets were expected to be present. This is due to their 3 times higher formation rate and $\sim$ 1000 longer lifetime than singlet, additionally, early studies on organic crystals found that the quenching rate of triplet excitons by free radicals [72] and trapped charge carriers [87] are field dependent. In a further paper published by the same group in 2010 [30], they applied two Lorenztian functions, Eq. 1.13, to fit their experimental data. They found that all data can be fitted properly, giving a low field component with a characteristic field B_1 of about 3-5 mT and a high field component with a characteristic field B_2 of about 160 mT. They attributed the low field component to the spin mixing process affecting exciton formation whilst the high field component to the triplet-charge carrier interaction (TCI) process.

Since the population of triplets can be adjusted by driving the current and operation temperature, Zhang et al. [48] at Southwest University investigated the TCI process via performing the MFE of three devices with different structures under different temperature and drive currents. The three device structures are: ITO / CuPu / NPB (60 nm) / Alq_3 (65 nm) / LiF / Al (device 1), ITO / CuPc / NPB (100 nm) / Alq_3 (15 nm) / LiF / Al (device 2), and ITO / CuPc / NPB (65 nm) / BCP (65 nm) / LiF / Al (device 3). At room temperature, the MC of these devices showed different line-shapes: The first device showed the normal positive line-shape at all currents — a rapid rise at low fields followed by a gradual rise at high fields. The second device showed a negative line-shape at low currents — a rapid decrease at low fields followed by a gradual decrease at high fields, this negative line-shape then transferred gradually to the normal line-shape as the current increased. The third device showed the normal line-shape at low current, however, as the current increased, the rapid low field rise remained whilst the subtle high field rise began to decay gradually. To make the line-shapes described clearer, the MC results of the three devices are presented in figure 1.16. They fitted the data using Eq. 1.13 used by Gillin et al. and found that the high field component (TCI strength), indicated by the pre-factor of A_2, increased as the driving current was increased. Also, the TCI strength increased as the operation temperature was decreased. Since both the increase of the current and the decrease the temperature result in an increase in the concentration of triplets, they concluded that the TCI strength is positively correlated to the population of triplets. However, the TCI contributed positively to MC in the first and the second device but negatively to the third device. They stated that this difference might come from the variations in the material thicknesses and/or the material of the active layer.

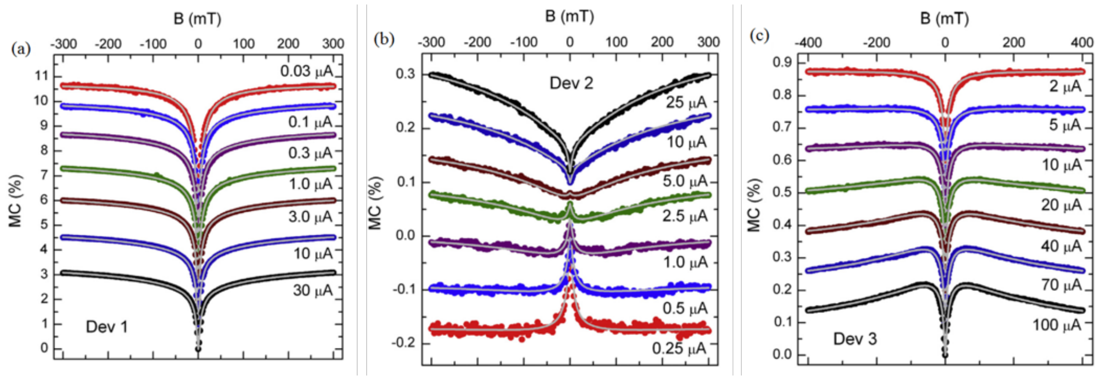

Figure 1.16: MC results with different line-shapes. Reproduced from ref [48].

Similar experiments were conducted by Zhang et al. [40] at QMUL to investigate the role of electrons and holes in TCI. Unlike what was done by Zhang et al. in Southwest University where they changed the thickness and the material of the active layer of the devices, Zhang et al. in QMUL changed only the electrodes of the devices whilst keeping the thickness and material the same. They controlled the injection of electrons and holes of the devices by modifying the cathode and anode, respectively. Three types of device were constructed: a 'standard' device which had decent injection in both electrons and holes with plasma treated ITO as anode and LiF/Al as cathode, a 'low hole injection' device which had a poor hole injection with untreated ITO as anode and LiF/Al as cathode, and a 'low electron injection' device which had poor electron injection with plasma treated ITO as the anode and Al as the cathode. All three devices showed positive MC, and the high field rise appeared to be more significant in the 'low hole injection' device. The MC was again fitted by Eq. 1.13 and A_2 was presented as a function of current density. They found that for all three devices, A_2 scaled approximately linearly with the current , which again confirmed the strong correlation between the strength of TCI and triplet concentration. Using A_2 as a measure of the TCI strength allowed them to concluded that triplet-electron interaction was stronger than triplet-hole interaction, because A_2 (low hole) > A_2 (standard) > A_2 (low electron).

To sum up, both of the above work showed strong correlation between triplets and the high field MFE, more specifically, the effect of triplet concentration on high field

MC. The work of Zhang et al. at South West University demonstrated that depending on the structure and material of the device, this high field effect can be both positive and negative. The work of Zhang et al. (QMUL) conjectured that this effect depended on the concentration as well as the sign of the charge carriers.

Multiple line-shapes and their dependence on triplets were found not only in works that investigate MC but also works that investigate MEL. Line-shapes found in MEL are generally categorised into two types: one is the most common positive line-shape featuring a rapid rise at low fields followed by a subtle increase at high fields, the other one is usually observed at low temperatures featuring a rapid rise at low fields ($B \leq 50$ mT) followed by a decay at higher fields. Refer to figure 1.16 (a) and (c) for a guide of these two types of line-shape. The magnitude of the high field decay depends on the measurement conditions of temperature and current density [43, 44, 62, 88]. MELs of this type was firstly observed by Johnson et al. in the delayed fluorescence of organic crystal systems in 1970s [20]. It was explained by a magnetic field dependent triplet-triplet annihilation process (as described in section 1.3). MELs of modern devices with this line-shape were first observed in 2009 by Liu et al. [44] in an Alq_3 based device. They performed temperature dependent MEL measurements on a device with the structure of ITO/CuPc/NPB/Alq_3/LiF/Al. Results demonstrated that MEL at room temperature showed the normal positive line-shape, as the temperature decreased, a gradual decay began to occur in the MEL at high field regime. At the same current density, the lower the temperature, the larger the decay became. At the same temperature (≤ 150 K), the larger the current density, the greater the decay became. Based on the similarity of the line-shape of this work and that of Johnson's, and the fact that the magnitude of the decay increased with increasing current and decreasing temperature, they attributed this high field decay to the TTA process proposed by Johnson et al..

Since then, MELs featuring the high field decay have been found under a wide variety of experimental conditions. Most of them were obtained at low temperature

[43, 44, 62, 88], and have been conveniently attributed to the magnetic field dependent TTA, because a higher triplet concentration is expected in low temperature due to the increase in triplet lifetime [89]. In addition, MELs with the same high field decay have been observed at room temperature [49, 61, 90]. Chen et al. [49] found similar high field decays in MELs of fluorescent dye DCM doped Alq_3-based devices at room temperature. They compared the MELs from pure Alq_3-based, 1% and 3% DCM doped devices. At room temperature, no high field decay was observed in the pure Alq_3-based device, whilst high field decay occurred in both 1% and 3% DCM doped Alq_3 devices. As the temperature decreased, the high field decay began to occur in the pure Alq_3-based device and the strength of decay was enhanced at lower temperatures, which is the same as that found by Liu et al.. The high field decay of the 1% doped device showed similar temperature dependence, however the magnitude of the decay was not as significant as that in the pure Alq_3 device. Interestingly, the high field decay of the 3% DCM doped device appeared to be independent of the temperature. The underlying mechanism of the high field decay of all devices was attributed to the TTA process. In terms of how TTA can occur in doped devices at room temperature, Chen et al. suggested that the DCM dopants acted as trapping sites for charge transport, triplets formed at these sites were therefore less vulnerable to quenching processes, as a result, large number of triplets were expected to be achieved in doped devices. Therefore high field decay occurred. However, although the triplets trapped on the DCM molecules may have a longer lifetime, the low DCM concentration means that the triplets are widely separated and the possibility of them interacting and undergoing TTA is reduced.

Peng et al. [90] conducted room temperature transient MEL measurements on Alq_3-based OLED devices and found that when driven at 1 kHz and with a 10 μs pulse width, the MELs also showed a high field decay, but when measured under steady state conditions they showed the more common positive effect. Keeping the frequency of the pulse at 5 kHz and varying the width of the pulse during measurements, they further found that the magnitude of MEL is a function of duty cycle: as the duty cycle increased from ~ 0 to ~ 1, the magnitude of MELs at a field of 150 mT changed from negative to positive. They explained this effect in terms of a combination of a charge trapping process and the TTA process. They claimed that the charge trapping to de-trapping ratio increased when the pulse width was increased at the same frequency. This quenched the triplets through triplet charge carrier interactions, reducing the TTA process and even eliminating it at long pulse widths. However, as the pulse width increased, higher triplet concentrations were achieved owing to their long lifetime. Therefore, the triplet concentration at larger pulse width is not necessarily lower than that of a small pulse width. Besides, it is worth noting that the conclusion of Peng et al. is contradictory with that of Chen et al. [49]. Peng et al. suggested that trapped charges weaken the TTA while Chen et al. believed that trapped charges enhance TTA.

In addition to the TTA process, spin-orbit coupling effects have also been proposed to explain the high field decay in MEL. Jia et al. [61] constructed Alq_3-based OLEDs with Au, Al, or Cu cathodes, they found large high field MEL decays in devices with Au or Cu cathodes and claimed that this is due to spin-orbit coupling enhancing the singlet to triplet conversion. The basic idea was that polaron pairs at the organic/metal interface were subject to the spin-orbit coupling generated by the metal, which enhanced the conversion of triplets to singlets, therefore contributing to the EL when there is no field. After applying a large magnetic field, the triplet to singlet conversion caused by spin-orbit coupling was suppressed, therefore less EL was expected, hence the high field MEL decay. Since the spin-orbit coupling strength is positively correlated to the atomic number (Z), the high field decay was present in devices with Cu and Au cathodes. However, this explanation is not convincing enough, because it has been shown in the literature that devices with high Z atoms in the emitting layer only show the common positive MEL at high fields [81]. Besides, MEL measurements have been performed on Gaq_3 and Inq_3 based OLEDs which again contain large Z atoms , and yet only the common positive MEL is observed [91]. Given these experiments, there does not appear to be much evidence that the spin-orbit coupling can account for the high field decay in

MEL.

In summary, I have shown that except for the common positive line-shape, there is another line-shape observed in MELs. This line-shape is called the high field decay in this work and features a rapid rise at low fields ($B < 50$ mT) followed by a decay at high fields. The occurrence of this line-shape depends on a variety of factors, like the measuring temperature, the driving current density, the purity of the active material, the duty circle of the pulse as well as the structure of the device. Although two mechanisms, the triplet-triplet annihilation and spin-orbit coupling, have been used to explain this high field decay, they are not convincing.

1.4 Aims and objectives

In section 1.3.3, I have introduced how the high field component was established and some of the main evidence that showed how this component is correlated to the concentration of excitons. Some literature shown the high field MFE suggested that the high field component is due to triplet-triplet charge carrier interaction and that holes and electrons may have different effects [40, 48]. Others suggests that triplet-triplet annihilation is responsible [43, 44, 62, 88]. In my work, the roles of excitons on high field MFE will be investigated further. It is aimed to study: first, from which process do excitons contribute to the high field MFE and how it is accomplished; second, is it true that triplets play a dominant role.

Chapter 2

Experimental methods

2.1 Material purification

All organic solid materials used in this thesis were purchased from Sigma-Aldrich. Despite their high purity, they were further purified via train sublimation prior to device fabrication. In this section the purification process of the Alq_3 will be used to introduce the train sublimation method.

Train sublimation, also known as temperature gradient sublimation, takes advantage of the differences in sublimation point of the target organic material and its impurities. Figure 2.1 shows a simple schematic diagram of a train sublimation system. It consists of three components: a vacuum station, a Carbolite Single Zone Furnace and Pyrex glassware (an inner tube, an outer tube and a boat as shown in figure 2.2).

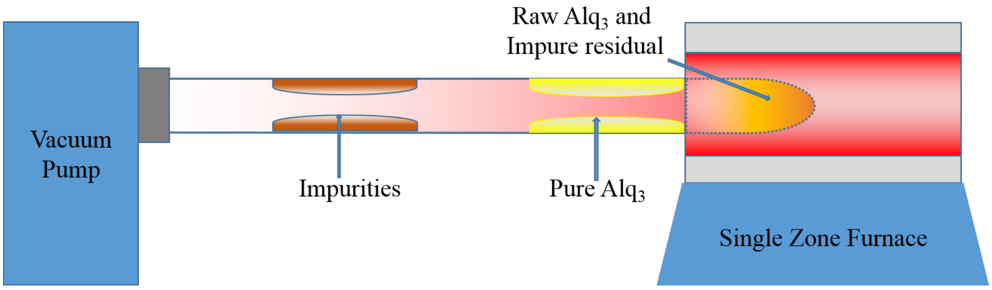

Figure 2.1: Schematic diagram of the setup of the Alq_3 purification. The pure Alq_3 was deposited on the inner tube near the furnace whilst the impurities were deposited further away from the furnace.

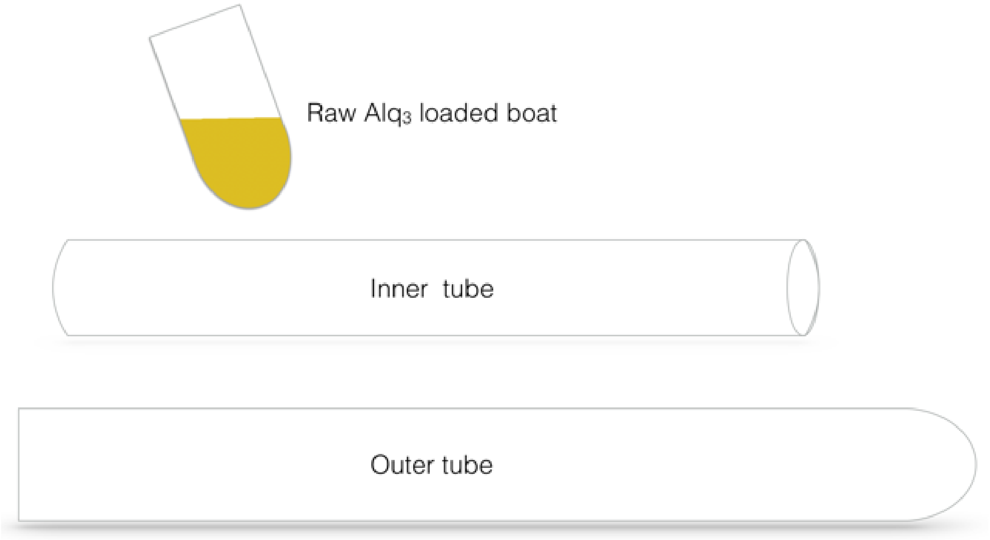

Figure 2.2: Glassware used in Alq_3 purification. The boat was used to hold raw material, the inner tube was used to collect sublimated materials and the outer tube was used to hold the boat and the inner tube.

The train sublimation procedure of Alq_3 follows:

Firstly, the two glass tubes and the boat were cleaned by a standard cleaning procedure (to be explained in detail in section section 2.2.1). Approximately 1 gram of Alq_3 was loaded into the glass boat and covered with glass fabric filter. The loaded boat was pushed to the closed end of the outer tube and the inner tube was inserted into the outer tube until it touched the boat. The open end of the outer tube was then connected to the pump station and the other end was inserted into the furnace. The system was pumped to a vacuum of the order of 10^{-7} mbar and the furnace was set to heat up to ~ 80 °C under a heating rate of 5 °C per minute. Once the temperature reached 80 °C, the system was left for $2 \sim 3$ hours to outgas until the vacuum of the system recovered to a low and stable value ($< 10^{-7}$ mbar). Finally, the temperature of the furnace was increased gradually with a step of 20 °C. Each time the system was left until the vacuum recovered before the next action. When the temperature reached the sublimation point of the Alq_3 (~ 200 °C under vacuum), a thin yellowish film starts to form on the inner tube. The temperature was increased slightly higher and the system was left until all raw material was evaporated. The system was then left to cool down to ambient room temperature for the purified Alq_3 to be collected.

It is worth noting that before the Alq_3 sublimation point, the glass tubes were placed further inside the furnace so that any impurities could be deposited on the further end of the inner tube. After the temperature reached the Alq_3 sublimation point, the glass tubes were moved out slightly from the furnace so that pure Alq_3 could be deposited on the end of inner tube near the furnace. After sublimation, the previously dark yellow raw Alq_3 in the boat became bright yellow purer Alq_3, leaving some brownish fluffy impurity in the boat.

2.2 Device fabrication

In this section, general processes related to a standard device fabrication, including substrates preparation, plasma treatment and thermal evaporation will be discussed. In the end of this section, the details of PEDOT:PSS spin casting will be presented as some of the devices used in this thesis contain a layer of PEDOT:PSS ($\sim$ 70 nm). A standard device refers to a device with the structure of ITO / TPD (500 Å) / Alq_3 (500 Å) / LiF (10 Å) / Al (1000 Å).

2.2.1 Substrate preparation

Raw substrates are 20 mm × 20 mm ITO coated glass. The sheet resistivity of the ITO is $\sim$ 13 Ω/square. Raw substrates are prepared to form a certain ITO pattern using the following steps, as shown in figure 2.3.

1. Standard cleaning
    - Rubbing with detergents under running water twice.
    - Sonicate with detergents in ultra-pure water in a sonicator for 20 minutes.
    - 3 × 5 minutes sonication in ultra-pure water.
    - 2 × 5 minutes sonication in acetone.
    - 2 × 5 minutes sonication in chloroform.
2. Dry with nitrogen

3. Spin coat positive photo-resist S1818.
4. Solidify in a preheated (90 °C) oven for 15 minutes.
5. UV exposure under the shadow mask for 1 minute.
6. Rinse in prepared developer (a mixture of ultra-pure water and 87% NaOH solution in a ratio of 3 : 1) for 20 - 30 seconds to remove the UV exposed photo-resist.
7. Rinse in pre-heated (48 - 50 °C) etching solution (a mixture of ultra-pure water, hydrochloric acid and nitric acid in a ratio of 50% : 48% : 2%) for ~ 1.5 minutes to remove the unwanted ITO.
8. Sonicate in acetone to remove the unexposed photo-resist.
9. Standard cleaning.

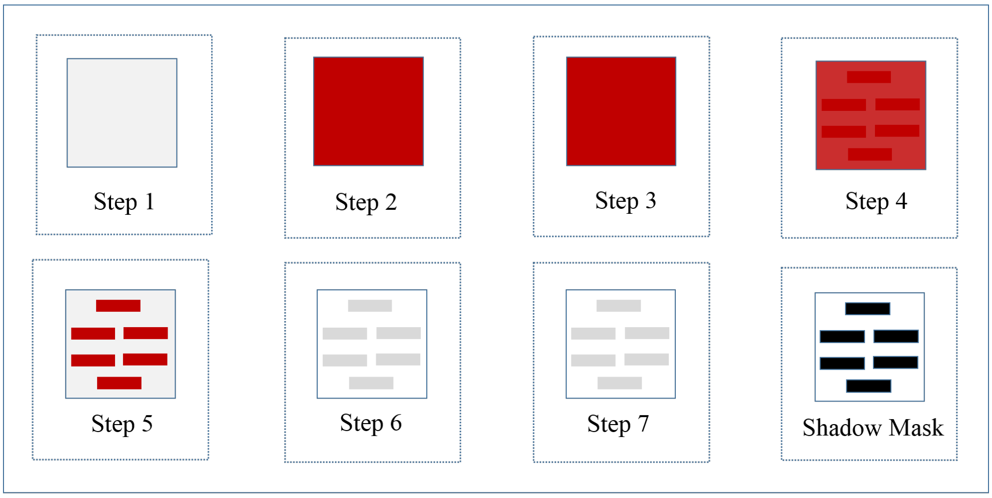

Top View Of Substrate After Each Step
1: Standard Cleaning 2: Photo-resist Spin Coating
3: Oven Solidify 4: UV Exposure
5: Developing 6: Etching 7: Standard Cleaning

Figure 2.3: Top view of a substrate after each step and the shadow mask used.

2.2.2 Plasma treatment

It has been experimentally shown that oxygen plasma treatment has improved the charge carrier injection ability of ITO by increasing the work function of ITO [92]. As a result, patterned ITO substrates were plasma treated after the standard cleaning before being loaded into an evaporation system.

The equipment used is a Diner Electronic Femto plasma system. The cleaned ITO substrate was loaded into the chamber of the system with the ITO side facing up. The system was evacuated below 0.1 mbar. A small amount of pure oxygen was introduced into the chamber until the pressure read between 2.0 $\sim$ 4.0 mbar. The system was kept in this condition for 5 minutes. This was to make sure that the chamber was filled only with oxygen. The pressure was reduced to a lower value between 0.2 $\sim$ 0.3 mbar which means that there was just a small amount of oxygen in the chamber. The system was run at a power level of 28% for 3.5 minutes. The plasma treated substrate was put onto a sample holder with the ITO side facing down, the holder was then loaded into the load lock of the thermal evaporation system, ready for material deposition.

2.2.3 Thermal evaporation

In this section, a brief introduction of the thermal evaporation system will be given. The deposition of organic materials and electrodes follow.

The Kurt J. Lesker SPECTROS thermal evaporation system:

Kurt J. Lesker SPECTROS thermal evaporation system is a computer controlled system designed for low sublimation point material deposition. Figure 2.4 shows a simplified schematic diagram of the system. It contains two steel cylindrical vacuum chambers, namely the load lock and the process chamber (PC). These two chambers are isolated by a vacuum gate valve, through which samples are transferred. The transferring action between the load lock and the PC is handled by the transfer arm. The thermal deposition process takes place in the PC. At the top of the PC, there is a four-layered mask cassette which is capable of moving up, down and also rotating. In the middle of the PC, there is a main shutter. Directly beneath it there are two quartz crystal monitors. The main shutter is designed to shield material vapour during pre-heating process and the quartz crystal monitors are used to monitor the rate and thickness of material vapour. The material crucibles are located at the bottom of the PC. Alumina crucibles at the top are used for organic material deposition. Beneath them are two titanium-diboride crucibles used for metal deposition. The crucibles are isolated by metal shields. A side view of the assembly of those crucibles are presented next to the PC in figure 2.4. The typical vacuum in the load lock is of the order of 10^{-7} mbar maintained by a turbo-molecular pump and that in the PC can reach the order of 10^{-8} mbar maintained by a cryo pump.

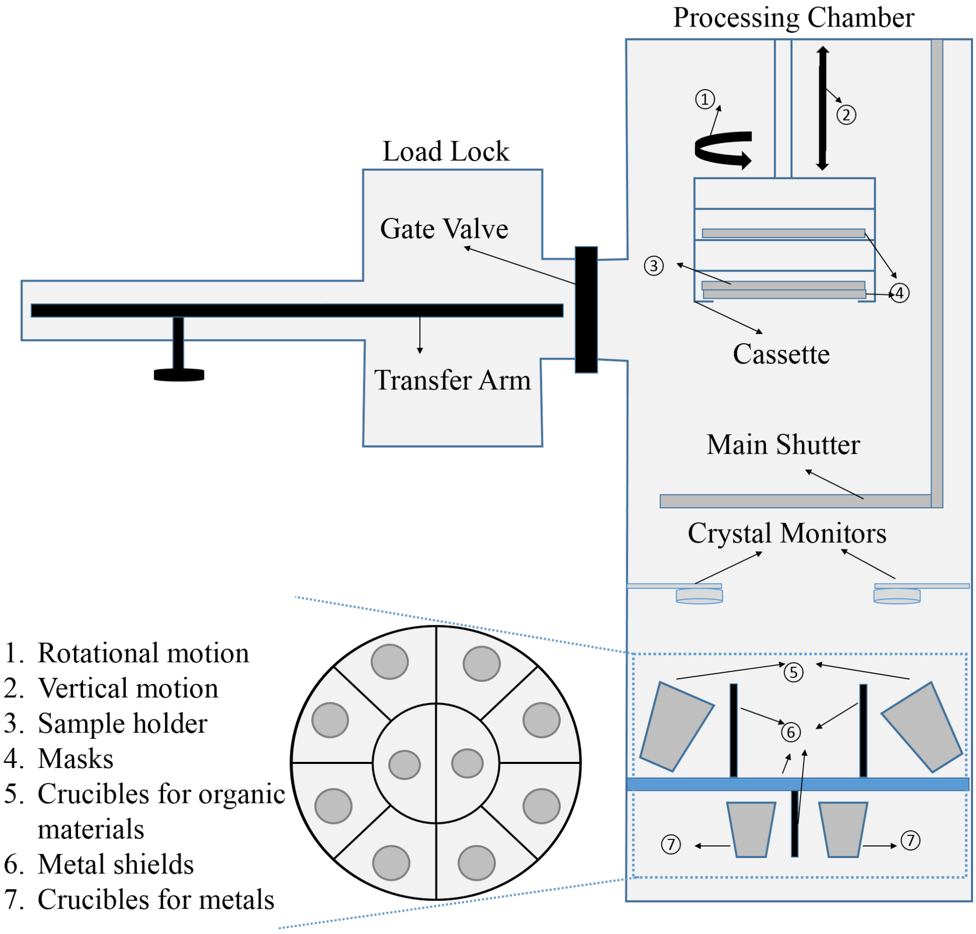

Figure 2.4: Schematic diagram of the Kurl J. Leskerevaperation system.

Organic materials deposition

The plasma treated ITO substrate was immediately loaded onto a substrate holder with the ITO side facing the open bottom of the holder. The holder was put onto the fork from load lock side. The load lock is then pumped down until the vacuum was less than 5 $\times 10^{-5}$ mbar and the holder was transferred onto the mask designed for organic material sublimation located in the bottom layer of the cassette. Following that, the cassette was lowered to the deposition position which is slightly above the main shutter. From experience, the organic material to be deposited was pre-heated to $\sim$ 40 degrees lower than its sublimation point to speed up the whole evaporation process. The deposition recipe of the corresponding material was performed until the rate of the vapour reached 0.5 Å per second. The main shutter was then moved away so that the organic vapour could deposit onto the ITO substrate. At the same time the system adjusted the sublimation rate gradually to 2 Å per second. To achieve a uniform thin film, the cassette was rotating at a rate of 10 Hz during the deposition of each material. For a standard OLED device, the deposition sequence of organic film was 500 Å TPD followed by 500 Å Alq_3.

Electrode sublimation

The cathode of the standard device consists of 10 Å LiF and 1000 Å Al. Unlike organic materials, LiF and Al do not need to be pre-heated, because they easily sublimate due to their relatively higher thermal conductivity. The sublimation of LiF took place immediately after Alq_3 because it used the same mask as organic material. The rate of LiF sublimation was set to 0.2 Å/s. For the sublimation of Al, a different mask was used. Two deposition rates were used during Al deposition, a smaller rate of 1 Å/s was used for the first 100 Å deposition to form a uniform interface with Alq_3 layer, a rate of 6 Å/s was used for the remaining 900 Å. Figure 2.5 shows the structure of a fully processed substrate and when it was under positive bias. Four OLEDs were formed on the same substrate after the procedures demonstrated above, each with an area of $\sim$ 4 mm^2. The dashed squares are guides to the rough positions of these OLEDs.

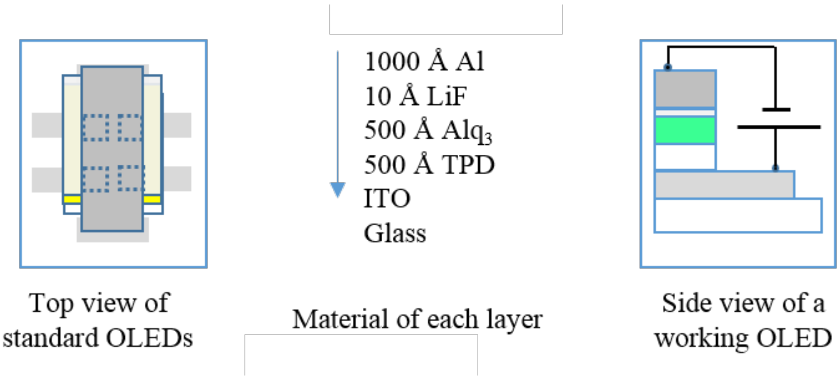

Figure 2.5: Top view of OLEDs formed on the same substrate(left) and side view of a positive biased OLED(right).

2.2.4 PEDOT:PSS spin coating

Some of the devices used in this thesis contain a $\sim$ 700 Å thick layer of PEDOT:PSS on top of ITO, a brief description of the spin casting process is giving below.

The PEDOT:PSS (Poly(3,4-ethylenedioxythiophene)–poly(styrenesulfonate)) used was purchased from Sigma-Aldrich. It is a low conductivity grade mixture of 0.14% PEDOT and 2.6% PSS dispersed in H_2O. Prior to spin coating, the PEDOT:PSS was filtered by a 0.45 µm filter to block larger particles. The cleaned ITO substrate was placed on top of a spin coater, 5 small drops of filtered PEDOT:PSS were placed on the substrate (one in the middle, 4 at the edges). The spin coater was then set to spin at 500 RPM for 9 second and at 4000 RPM for 60 second. The substrate was then solidified in a pre-heated oven at 130 °C for 15 minutes. After that, the substrate was loaded into the evaporation system for other material deposition. The thickness of PEDOT:PSS from the above procedure was 700 ± 50 Å. The amount of PEDOT:PSS and the spin rates used above were obtained by different trials. Its thickness was measured using the Dektak Surface Profilometer. According to the thickness, the amount of PEDOT:PSS and spin rates were adjusted subsequently until the desire thickness was achieved.

2.3 Current - Voltage - Luminosity (IVL) measurement

Each fabricated device generally underwent an IVL characterisation. A schematic of an IVL setup is shown in figure 2.6. A sample holder with vacuum port was used to provide electrical access via a LEMO connecter. An Agilent 2902A Source Measure Unit (SMU) was used to provide voltage across the device and measure the current flow accordingly. A Newport silicon photodetector (S/N 13594) incorporated with its matching integrating sphere was used to measure the light output. A calibration module then transferred the signal to Newport 1830-C, giving the power of the light output (EL) in unit of watts. A turbo molecular pump was used to create a $< 10^{-5}$ mbar vacuum environment for the sample. The use of an integrating sphere made the incoming light distribute evenly, hence gave an absolute value of the EL. This made the comparison of EL or efficiencies of devices with different structures possible. After setup, the measuring process was controlled by the "IVL" software from the PC. It created a list of voltages need to be measured. During the sweep of each voltage, 32 readings of the current was taken and the average value was calculated as the final current to be recorded. The EL was then measured and only one reading was taken.

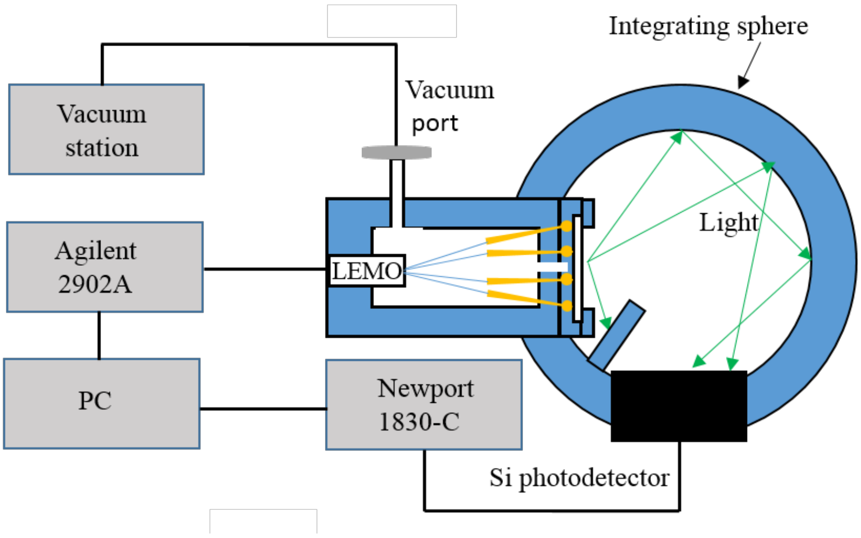

Figure 2.6: Schematic diagram of the IVL measurement setup.

Typical IVL characteristics of a standard OLED are shown in Figure 2.7. It shows the characteristics of a light emitting diode with a current turn-on at 2.2±0.1 V and a EL turn-on at 2.3±0.1 V. Along with the IVL is the power efficiency as a function of current, peaking at 0.65%. One should bear in mind that improving device efficiency is not the purpose of this work. The peak efficiency was taken only as a standard of showing the reproducibility of devices with the same structure.

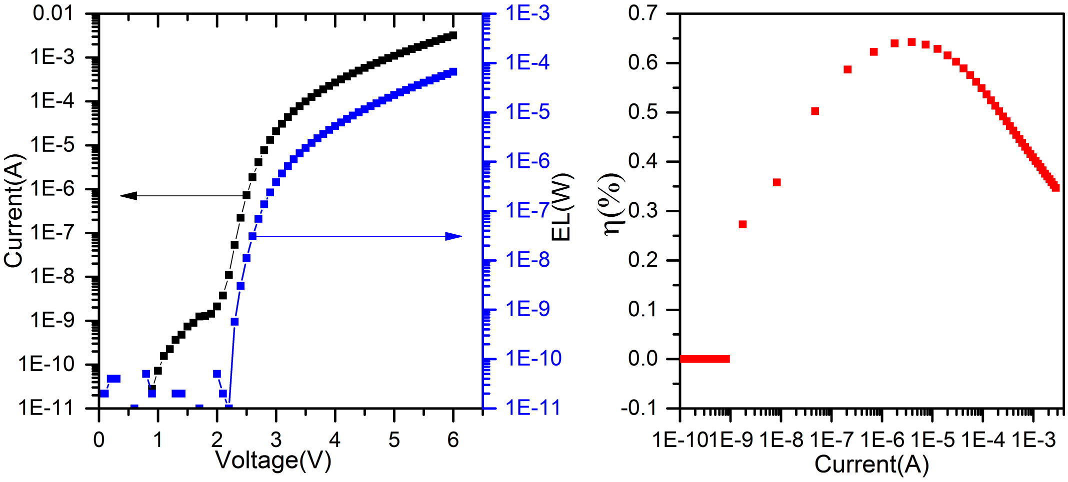

Figure 2.7: IVL characteristics of a standard OLED (left) and its power efficiency (right).

2.4 Magnetic field effects measurement

The measuring of OLED performance under magnetic fields will be discussed. It consists of two parts: measurement with a DC voltage, namely the steady state measurement, and measurement with a pulsed voltage, the transient measurement.

2.4.1 Steady state MFE measurement

The steady state MFE measures the current and the EL of a working OLED in magnetic fields. The measurement was carried out at room temperature. Figure 2.8 shows a schematic diagram of the setup of the sample at room temperature MFE measurements. The sample holder was secured between the two magnet pole pieces in the way that the magnetic field is parallel to the sample surface and perpendicular to the current flow in the device. As with the IVL characterisation, the Agilent 2902A SMU provided DC voltage driving for the device via the LEMO connector. The silicon photodetector was connected directly to the sample by a light tight lock to measure the EL intensity. A KEPCO power supply provided current for the magnets. A model 475 DSP Gaussmeter was used to measure the magnetic field strength and control the current flow of the KEPCO power supply. The space between the two pole pieces was set to 8 cm which was wide enough to mount the sample holder but kept as small as possible to achieve larger fields. The largest magnetic field strength achieved with this setup was around 850 mT.

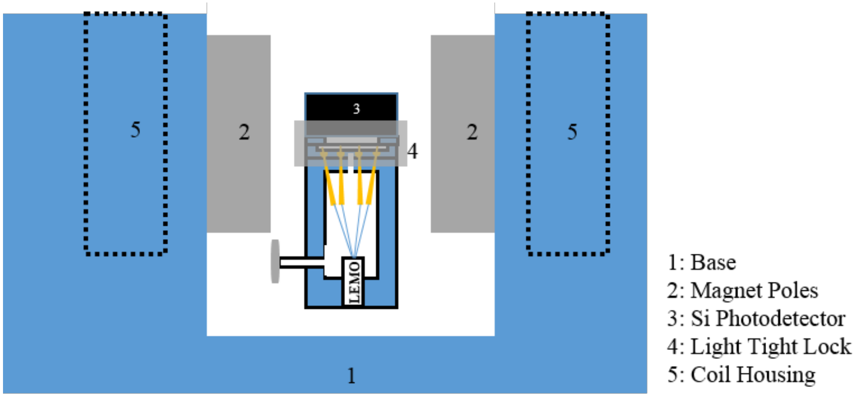

Figure 2.8: Schematic diagram of the sample setup of steady state MFE measurements at room temperature.

The whole MFE measurement procedure was controlled automatically by a software named ‘magnetoresistance’. It runs from low voltage to high voltage, for the measurement at each voltage, the field starts from low field to high field. The system firstly sets a DC voltage to the device, waits for 1 minute, so that the current flow through the device is stabilised. The B field is adjusted to 0 mT (zero field), and the current and the EL are subsequently recorded. The field strength is then moved to the target field, the current and the EL are measured accordingly. The field strength is then moved back to zero field and the current and EL measured. The measurement procedure carries on alternatively measuring the current and EL at target fields and zero fields until the last target field measurement finishes. An additional measurement at zero field is taken to finish the measurement of a single voltage. DC voltage is set to zero and turned off afterwards. The field strength along with the current and the EL data are saved in a text file, forming raw data of

MFEs at a particular voltage. The software then moves onto the MFEs measurement of another DC voltage. MEFs measurement was carried out from low voltage to high voltage to avoid electrical stressing (conditioning). As mentioned in the introduction chapter, conditioning can enhance MFE effects (see section 3.3.3 for details). Changing B field strength from low field to high field was just a matter of personal preferences. Measurements taken from high field to low field have been carried out and showed no difference to the low to high one. To improve the signal to noise ratio, the value of a recorded current is the average over hundreds of readings taken in a very short time during the measurement.

2.4.2 Transient MFE measurement

The transient MFE measurement measures only the EL of a working device as a function of time under a particular magnetic field strength. This allows us to investigate how the MEL evolves with time on a scale of nanoseconds to milliseconds. The experimental setup is shown in figure 2.9. Apparatus used in this procedure includes a pump station to provide vacuum environment for the sample; a TGA1241 waveform generator to provide pulse waves to drive the sample device; a triax 550 Spectrometer coupled with a photo multiplier tube (PMT) to detect the EL signal; two optical lenses to focus the light on the entrance gate of the spectrometer; a high definition oscilloscope to store and display the EL signal. The signal received by the PMT was going through a load resistor R and the voltage drop across the resistor was stored by the oscilloscope.

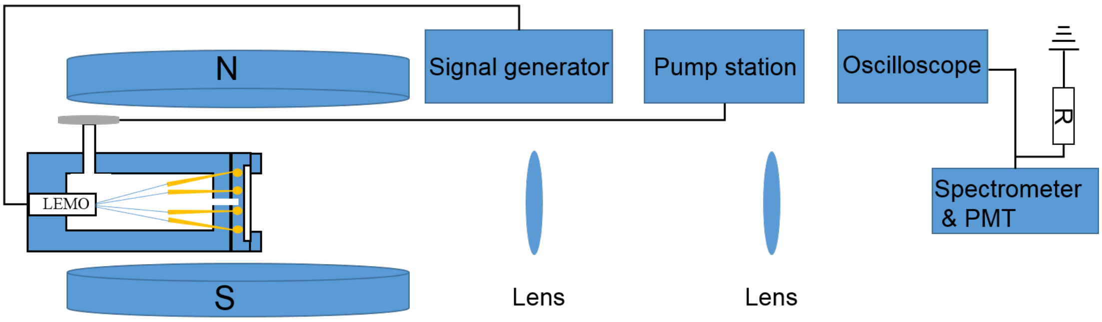

Figure 2.9: Schematic diagram showing the setup of the transient MEF measurement.

The resistance of the resistor can affect the signal received. The larger the resistance is the stronger the signal will be. However, larger resistance can also cause larger RC decay, which may hide important information. In order to find out an appropriate resistance, EL measurement of a standard OLED was conducted with resistors of different value. Figure 2.10 shows the EL signal measured with 50 Ω, 500 Ω and 1 kΩ resistors. The pulse used is of 1 kHz frequency and 1 μs width. It can be seen that The EL signal increase proportionally to the resistor and the EL measured with 50 Ω resistor is of the order of 10^{-4}, which is very small for further MFEs measurement.

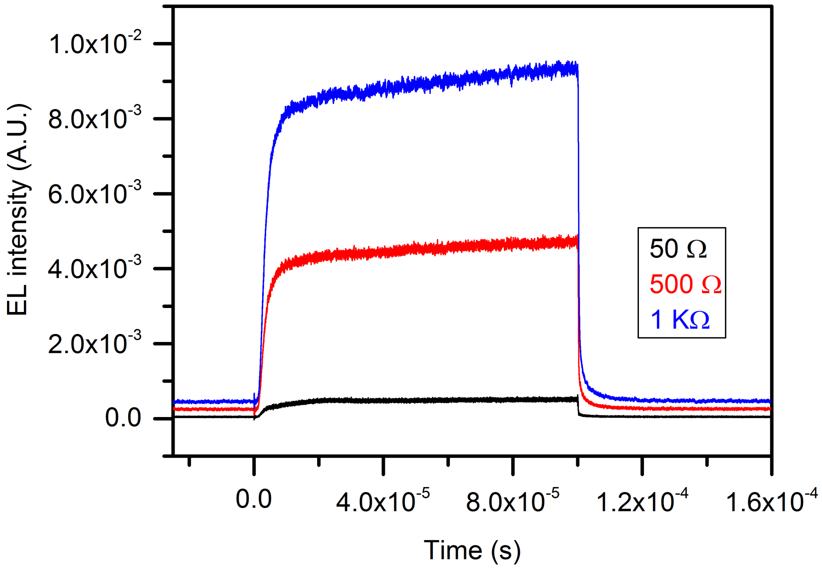

Figure 2.10: EL signal measured with different resistor.

In order to check the RC response of instruments of this setup, a laser pulse of nanosecond width was used to conduct the same measurement. The normalised signal was presented in figure 2.11(a). The RC time constant increases with resistance. Exponential decay fitting found out that the RC time constant is 8.33×10^{-9} s, 8.37×10^{-8} s and 1.65×10^{-7} s respectively. Figure 2.11(b) shows the normalised decay of the ELs of the OLED. The Zero time point was set as the point from which the ELs began to decrease. The green line is a guide to eyes and was set to have a magnitude of 0.1. It can be seen that there is a fast and a slow decay in each EL. The fast decays, dominated by the RC time constant varies with the resistance, however, the slow decays don't vary much, especially for the 50 Ω and 1 kΩ ones. The comparison of the decays of the signals of the laser and those of the OLED implies that the slow tails are real signals due to the OLED itself rather than the instruments. Also, the RC decay does not hide the signals, as a result, the 1 kΩ resistor was used in the rest of the measurement.

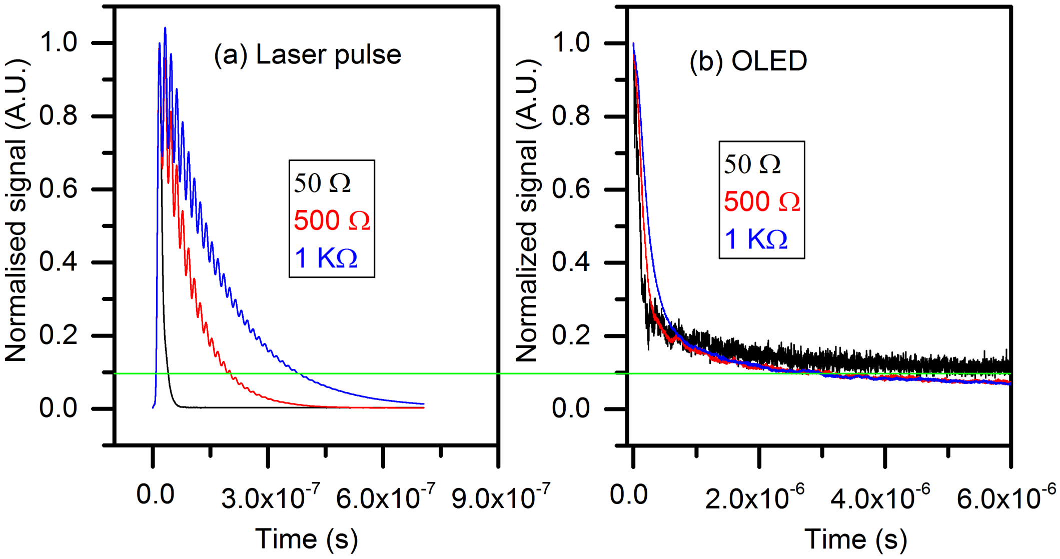

Figure 2.11: (a), instrument response measured with a laser pulse; (b), EL decays of a standard OLED. Signals were normalised.

The Labview based software 'MRTS' was used to conduct the transient MFEs measurements. The main inputs of the software are a text file containing a list of target fields, the magnitude of the working pulse and the magnitude of the background pulse. The outcomes are 2N+1 raw data files where N is the number of target fields. Before and after each file measured at a target field, there is a file measured at zero field. The average of these two raw data at zero field is then used as the zero field signal in the final calculation. Each raw data is the EL signal as a function of time at a particular B field. A final EL signal is the difference of the EL signal taken at working pulse and the EL signal taken at background pulse. Background pulses were set to 1 V at which the EL of the device was not turned on.

Chapter 3

The effects of exciton-charge carrier interaction on MEL

3.1 Introduction

It was demonstrated in 1.3.3 that triplet-charge carrier interaction (TTA) and triplet-charge carrier interaction (TCI) both show high field dependent. TCI was proved to exist by Zhang et al. at QMUL and Zhang et al. at South West University through controlling exciton concentration via varying the structures and the measuring conditions of the devices. It was claimed to be responsible for the change of the MC line-shapes at high fields. The results of from QMUL further showed that the polarity of the charge carriers that interact with triplets may as well play a role. That is, the triplet-electron interaction is more significant than triplet-hole interaction. In Alq_3 based systems the TTA was widely used to explain the high field MEL decay. The high field decay obtained at low temperatures, where larger triplet concentration is expected, was attributed to TTA [43, 44, 62, 88]. The high field decay obtained in DCM doped devices at room temperature was attributed to TTA although it is not certain whether high triplet concentration was achieved or not. The high field decay obtained in transient measurements at room temperature was also attributed to TTA. The existence of high triplet concentration due to the charge trapping to de-trapping ratio is not clear since for both TCI and TTA, the concentration of exciton plays an important role. The current work will investigate the role of excitons on MFEs in OLEDs via controlling the structure of the devices. In the experiment at South West University they changed the thickness of NPB and Alq_3 in the first and the second device. When it came to the third device, the Alq_3 layer was substituted by a BCP layer. The change of multiple elements in the experiment makes the comparison of the behaviour of MFEs among different devices difficult although the comparison of the behaviour of a particular device under different measurement conditions is still reliable. As for the experiment at QMUL, they adjusted only the electrodes of each device whilst keeping the thickness of TDP and Alq_3 layers the same. Anodes are ITO with or without O_2 plasma treatment and cathodes are Al with or without LiF between Al and Alq_3 interface. This makes the comparison of MFEs among devices possible. In the current work, Alq_3 was used as the active layer where light emission and potential processes like TCI and TTA occur. To make the comparison among different devices possible, the thickness of Alq_3 layer was kept the same. Like the previous work at QMUL the concentration of excitons in the current work was adjusted via controlling the injection of electrons and holes. However, the change of hole and electron injection were moderate in their work, because the difference of the Fermi level of ITO and plasma treated ITO is 0.3 eV and that of LiF/Al and Al is 1 eV [42].

3.2 Device structure and experiments

Devices with four structures were used to modify either the hole or electron injection into Alq_3 based devices, so as to modulate the exciton concentration as well as the charge to exciton ratio in the devices. These were named A, B, C, and D. Device A is a device with "standard" structure consisting of ITO / TPD (50 nm) / Alq_3 (50 nm) / LiF (1 nm) / Al(100 nm). Device B was designed to include a poly(3,4-ethylenedioxythiophene) polystyrene sulfonate (PEDOT) hole injection layer to improve the hole injection and had the structure, ITO / PEDOT (70 nm) / TPD (50 nm) / Alq_3(50 nm) / LiF (1 nm) / Al (100 nm). Device C had the TPD layer removed to directly inject holes into the Alq_3 layer and had the structure, ITO / PEDOT (70 nm) / Alq_3(100 nm) / LiF (1 nm) / Al (100 nm). Finally, device D, with the structure ITO / PEDOT (70 nm) / TPD (50 nm) / Alq_3 (50 nm) / Au (80 nm), had its cathode replaced with gold to reduce the electron injection. Device A was designed to generate moderate charge injection of both electrons and holes, therefore, a balanced hole to electron ratio was expected. Compared to device A, device B was expected to achieve a slightly higher hole to electron ratio, because of the presence of the PEDOT layer which is supposed to enhance the hole injection; device C was expected to achieve an even higher hole to electron ratio, because of the absence of the TPD layer; device D was expected to achieve the highest hole to electron ratio, because of the substitution of the cathode LiF/Al with Au.

IVL measurements were firstly conducted to check the diode characteristic of the devices, the steady state MEL measurement was then carried out to investigate the MFEs.

3.3 Results and discussion

3.3.1 Current - voltage and EL - voltage characteristics

Through the IVL measurement, one can obtain the current - voltage characteristics, the EL - voltage characteristics and the efficiency of a device. The EL intensity allows one to calculate the approx population of singlet in the devices, and the efficiency can be used to estimate the electron-hole balance of the devices.

Figure 3.1(a) shows the IVL characteristics of all the devices in a log - linear scale. It can be seen that all four devices show a clear diode characteristic, the turn on voltages for device A - D are 2.1 V, 2.2 V, 2.3 V and 1.6 V respectively, within an error of ± 0.1 V. The turn on voltage is positively correlated to the difference between the Fermi level of the cathode and the anode in a device. The results presented are agree qualitatively with what was expected. Compared to device A, the use of a PEDOT layer in devices B and C is expected to lower the Fermi level compared to the ITO anode. Considering the ITO/PEDOT as an anode, it has a work function of 5.2 eV [93], approximately 0.2 eV larger than that of plasma treated ITO, hence a slightly higher turn on voltage is expected in devices B and C. The turn on voltage, however, can also be affected by the interfaces near the electrodes. This might be the reason for the small variation of the turn on voltage in devices B and C, because device B has a PEDOT/TPD interface whilst device C has a PEDOT/Alq$_3$ interface. To explain the extremely small turn on voltage of device D, device B is taken as the reference, because the only difference between them is the cathode. Device B has LiF/Al as its cathode and device D has Au as its cathode. The work function of Au is 0.8 eV larger than that of LiF/Al, which, therefore, explains the much lower turn on voltage of device D. Another noticeable feature in figure 3.1(a) is the difference of leakage current in device A compared to devices B - C. The current flow before current turn on is defined as the leakage current which increases linearly with drive voltage, following the Ohm's law. The leakage current in devices B - C is approximately one order of magnitude higher than that of device A. This is probably due the conduction between the ITO and the cathode pads via the PEDOT layer. The PEDOT used in the devices were purchased from Sigma - Aldrich, featuring a resistivity of $\sim 10^3\Omega$ m. Since the thickness of the PEDOT layer is $\sim$ 700 Å, a simple calculation shows that the sheet resistance is of the order of 10^9 Ω/square, which is correspond to the resistance needed for the leakage current.

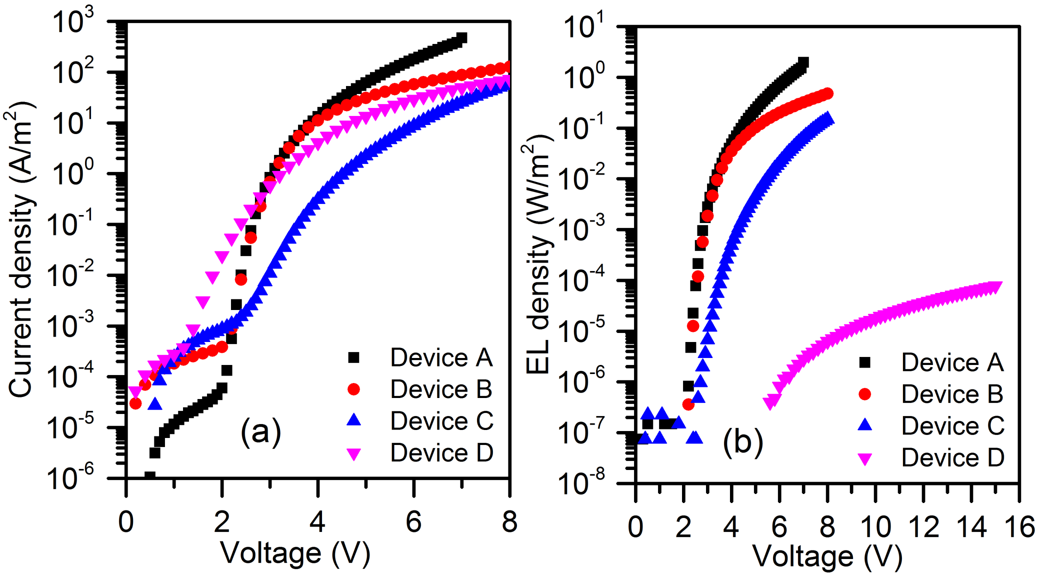

Figure 3.1: (a), Current density - voltage characteristic and (b), EL density - voltage characteristic of devices A - D. Device structures are: A, ITO/TPD/Alq_3/LiFAl; B, ITO/PEDOT/TPD/Alq_3/LiF/Al; C, ITO/PEDOT/Alq_3/LiF/Al; D, ITO/PEDOT/TPD/Alq_3/Au.

Figure 3.1(b) shows the EL intensity - voltage characteristics of devices A - D. Similar turn-on behaviour is presented, the EL turn on of devices A and B occurs at 2.2 V, and that of devices C and D occur at 2.4 V and 5.6 V. The real turn on might be lower than shown, because it can be shadowed by the sensitivity of the photo detector and the noise level. However, this is not of an issue in the current work, because only the relative relations of these devices matter. The EL intensity is taken to give a guidance to the exciton concentration in those devices and the turn on points give an idea of the polarity of the current before EL occurrence. For example, the current of device D turns on at 1.6 V whilst the measurable EL occurs at 5.6 V, which indicates that the current flow of device D before 5.6 V can be taken as predominantly ‘hole only’ because Au is a poor electron injector. On the contrary, both electrons and holes contribute the current in devices A - C soon after the current turn on.

It can also be seen from figure 3.1(a) that devices A and B show a sharper rise of current after turn on than devices C and D. Knowing that the current flow in device D before 5.6 V is predominantly ‘hole only’ and giving the similarity of the shapes of current rise after turn on in devices C and D, it is reasonable to assume that the current in device C is hole dominated. Since the hole mobility in Alq_3 is much smaller than that of the electron [94], the rise of current in devices C and D is less steep, which also corresponds to the EL turn on shapes in figure 3.1(b). Devices A and B both show a rapid rise in current and EL, which indicates a much more balanced electron and hole injection. Compared to device A, lower current and EL are present in device B. Since the only difference between device A and B is the improved ability of hole injection in device B, the lower current and EL might be a result of excessive holes in the device.

3.3.2 Comparison of efficiency

Figure 3.2 shows the power efficiency of devices A - D as a function of current density, the magnitude of the efficiency of device D was magnified 20000 times. Over the

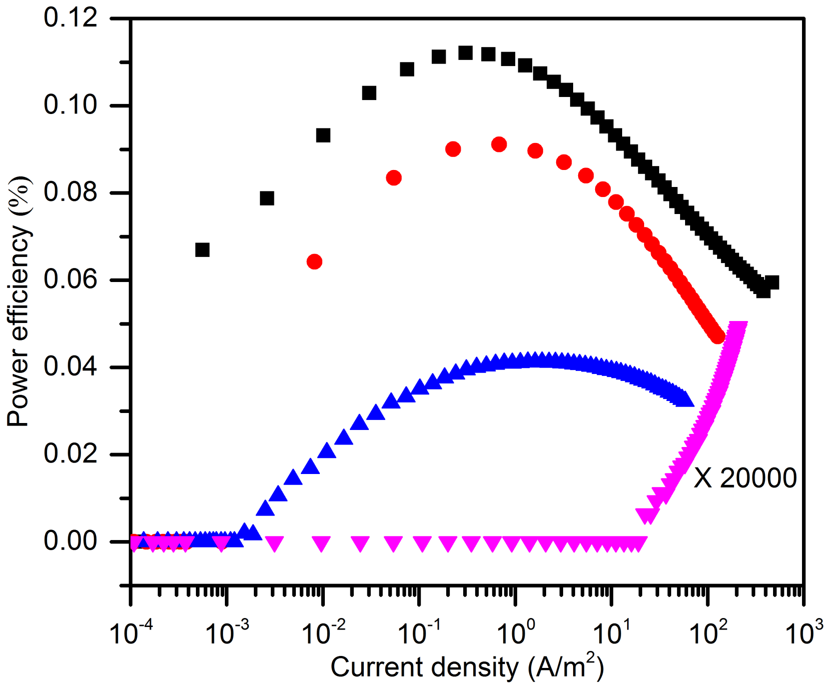

Figure 3.2: Power efficiency as a function of current density: black square, device A; red dot, device B; blue up triangle, device C; pink down triangle, device D. The magnitude of device D was 20000 times magnified.

whole current range, efficiency decreases from device A to device D. Devices A - C show an initial rise in the efficiency as the current increases, the efficiencies then reach a peak value, followed by a decline as the current increases further. These are the common efficiency features in many organic diodes. Unlike the other three devices, device D is a very inefficient device. It can be seen from figure 3.2 that light emission from device D only occurs at a current density > 22 A/m^2, which is nearly 4 orders of magnitude higher than the other devices. Also, unlike the trend in the other devices, the efficiency in device D keeps increasing with the current. Giving the huge injection barrier for electrons in device D, this extremely low efficiency is not surprising. It has been discussed that before EL turn on, device D is 'hole only', as EL occurs, electrons begin to be injected and the number of electron injected increases with the drive voltage, therefore the EL increases, hence the efficiency increases.

As has been discussed in section 1.2.4, there are many processes present in the active layer of a device during operation and each of them is capable of modulating the efficiency. After electrons and holes meet in the active layer, they form polaron pairs in singlet and triplet configuration with a ratio of 1:3 spontaneously. These polaron pairs then form singlets and triplets accordingly, and the radiative decay of singlet gives the light emission. Apart from the radiative decay, singlets are also subject to the non-radiative decay which can be enhanced by exciton charge carrier interaction as well as the electric field assisted dissociation. These can qualitatively explain the initial rise then roll off of the efficiency as a function of current density. At low current density, the concentration of the charge carriers is small, as is the electric field. The increase of electric field enhances the injection of charge carriers, and, as the concentration of charge carrier increases the possibility of elections and holes meeting increases. Hence the formation rate of excitons increases, therefore the efficiency increases. As the electric field increases further, although the exciton formation rate may still increase, there is increasing possibility of excitons meeting and interacting with excessive charge carriers. This quenches the excitons, causing the efficiency roll off at large current density. Another possible reason for the efficiency roll off at large current density might be that a large number of triplets reducing the number of molecules in ground state. this would reduce the molecules that are available for forming singlets, hence reduce the efficiency.

3.3.3 Comparison of magnetic field effects

Following IVL characterisation, each device was subjected to the steady state MFE measurement. Raw data from each measurement contains current and EL. It is important to look at the raw data because we must ensure that the data to be discussed is at the regime where all the devices behave normally .

Figure 3.3 shows two sets of raw data from the MFE measurement of device A at different voltages. Figure 3.3(a) shows the raw data at low current density which corresponds to low drive voltage. The red dots present the current measured with the magnetic field on and the black squares at zero field. The whole measurement sequence of a set of raw data begins and ends with a measurement at zero field, in between them are alternating measurements at non-zero and zero fields, the magnetic field increases as the measurement continues. From the black squared line it can be seen that there is a small current drift at zero fields as the measurement

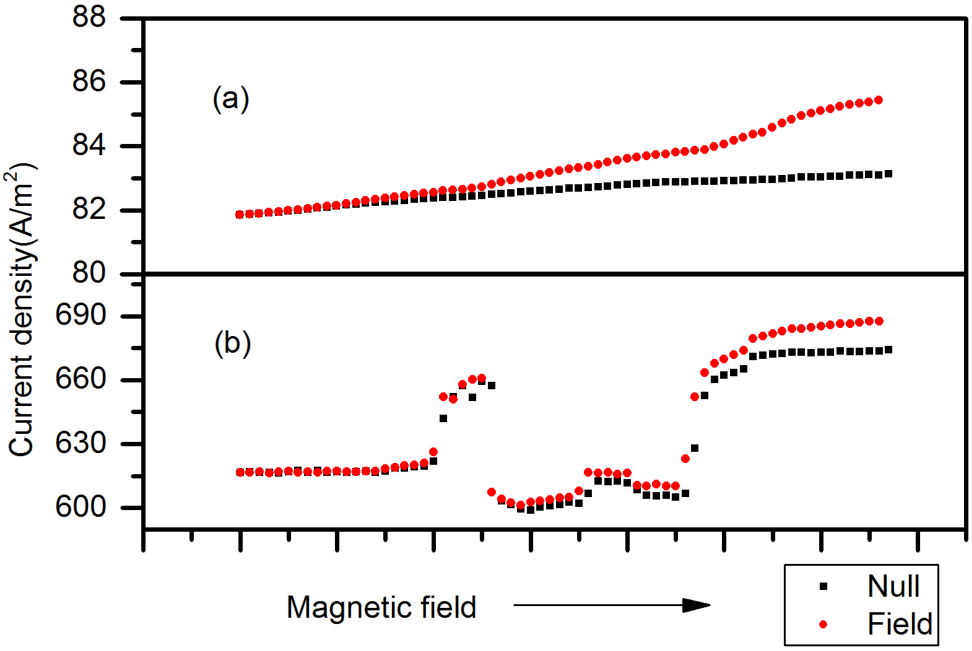

Figure 3.3: Examples of MFE raw data. Current density with and without field of device A measured at 5 V (a) and 9 V (b).

carries on. This drift can be in an increasing trend, like the one in figure 3.3(a), or in a decreasing trend. Usually, the drift at low drive voltages shows the increasing trend and the drift at high drive voltages decreases. The increasing trend is most likely due to the thermal effect on the charge carrier mobility. As organic devices feature high resistance, significant heating can occur upon continuous current flow through the device. The mobility of charge carriers in organic systems is very sensitive to temperature. Eq. 3.1 shows the dependence of mobility on temperature deduced from Eq. 1.2 [11], where μ is the mobility, μ_0 is a hypothetical mobility at infinite temperature and zero electric field, T the temperature, k_B the Boltzmann constant and σ the energy disorder parameter which has an experimental value in the range of 50 meV - 150 meV [95].

$$\mu \;\propto\; \mu_0\, e^{-(\frac{2}{3k_B T}\sigma)^2} \tag{3.1}$$

As joule heating raises up the temperature of the device, charge carrier mobility increases, and so does the current density. Assuming that μ_1 is the mobility at T_1, μ_2 is the mobility at T_2 and T_1 is 293 K. One can calculate from Eq. 3.2 that the temperature needed for a 10% increase in the mobility is just 295 K.

$$T_2 \;=\; \frac{2\,\sigma}{\sqrt{4\sigma^2 - 9(k_B T_1)^2 \ln\frac{\mu_2}{\mu_1}}}\, T_1 \tag{3.2}$$

The decreasing trend is due to the device degradation. The reason of the degradation can be oxygen, moisture and large joule heating [96, 97]. As long as the drifts in the devices are approximately linear, the problem can be solved by taking the average of the two zero field measurements before and behind the field measurement as the zero value to compensate the drift. Severe break downs can, however, occur at high voltages, causing large jumps in the raw data, as shown in figure 3.3(b). In this case, devices lose their diode characteristics and the MFE calculated from the raw data will be noisy, misshapen and meaningless. All data that is going to be presented and discussed in the current work is taken at the regime where diode characteristics are reserved.

The effect of electrical conditioning on MFEs

Electrical conditioning has been found to enhance the MFEs in polymer based OLED systems significantly [35, 36]. Niedermeier et al. [35] conducted electrical conditioned MFE measurements on poly(paraphenylene vinylene) (PPV) based devices. They found that for the enhancement to occur, the conditioning current density has to be larger than the operational current density, the larger the conditioning current is the more significant the MR enhancement will be. The result of MFE as a function of stressing duration up to 10 hours showed that the longer the duration the large the enhancement. The conditioning process can easily cause an improvement of the MR (ΔR / R) from 1% to 15%. However, they found that applying a reverse bias does not cause any MR enhancement. They suggested that the degradation of the bulk material during conditioning process is responsible for the MR enhancement. Among all the possible degradation mechanisms, the thermal degradation of the active material and the dark spot formation were excluded because the temperature of the devices was much smaller than the glass transition temperature of PPV and no dark spots were found in these devices. They then concluded that this conditioning effect is caused by defects, like traps or non-radiative recombination centres, generated due to the energy released from non-radiative processes. In a later paper, Bagnich et al. [36] found that by shining an infrared light on the preconditioned device the enhanced MFE can be reduced, after removing the infrared source, the enhanced MFE is restored. They also found that annealing the preconditioned device at high temperature can eliminate the enhanced MFE and in order to restore the enhanced MEF, the device needs to be conditioned again. They suggested that the electrical conditioning process is accompanied by the formation of energetic traps and/of the transformation of the polymer morphology.

Although the electrical conditioning works shown in the above paragraph were conducted on polymer based devices, it is very likely that similar effects are expected in the Alq_3 based devices. Therefore, in my work, which focuses on the interaction of excitons and charge carriers, it is important to avoid the electrical conditioning phenomena. As a result, attempted conditioning measurements were conducted on standard OELDs to study how it affects the MFEs and what is the best way to carry out the main experiments.

Two OLEDs grown on the same substrate were used to do the electrical conditioning MFE measurement, one was measured from low voltage to high voltage and the other one measured from high voltage to low voltage. Figure 3.4 shows the MC ($\Delta I/I$) and MEL ($\Delta EL/EL$) of these two devices. Significant enhancements in both the MC and MEL can be seen when measured from high voltage to low voltage. This means that like the polymer systems studied by Niedermeier et al., electrical conditioning effects also occurs in the Alq_3 small molecular system. Compared to the low voltage to high voltage measurement results, the highest MC from the high voltage to low voltage

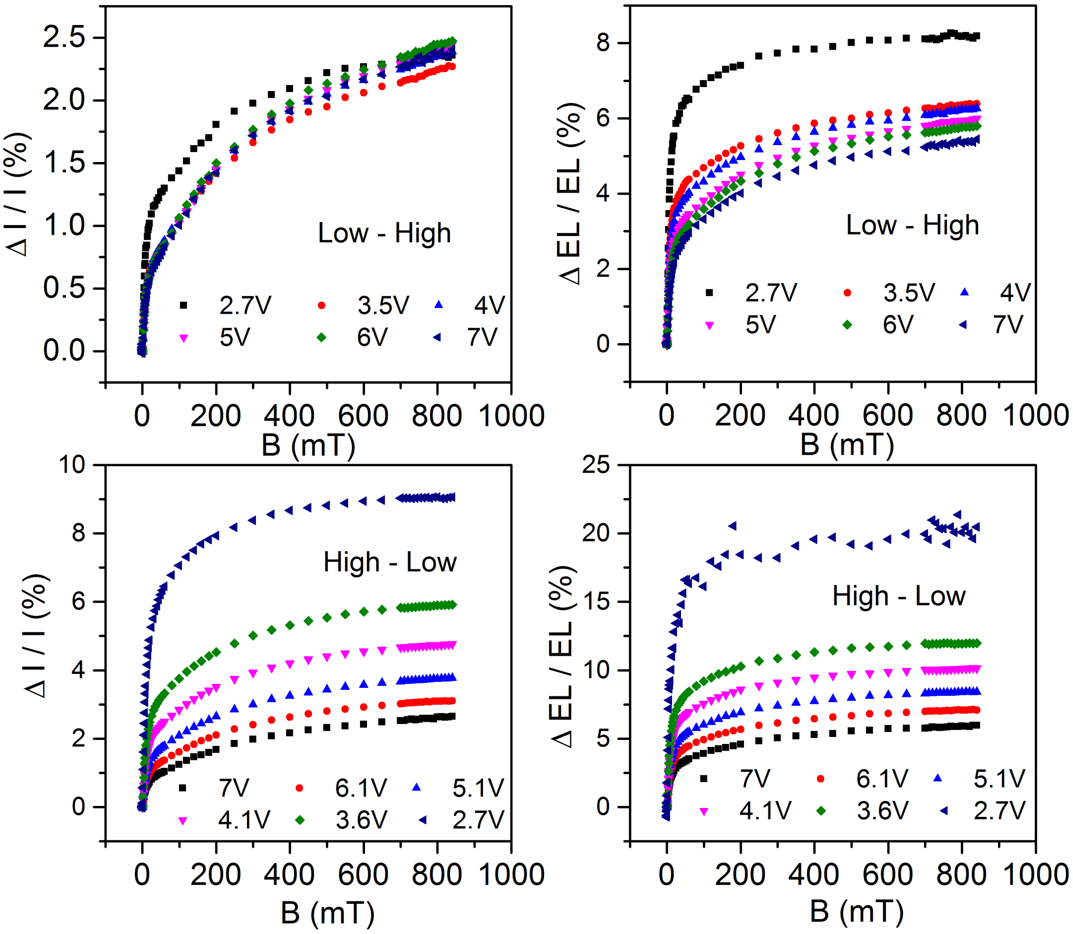

Figure 3.4: MC and MEL measured from low voltage to high voltage (top) and measured from high voltage to low voltage (bottom). The experiments were conducted on two fresh standard OLEDs.

measurement has more than tripled and the highest MEL doubled. Figure 3.5 shows the MC and MEL measured at 800 mT as function of drive voltage.

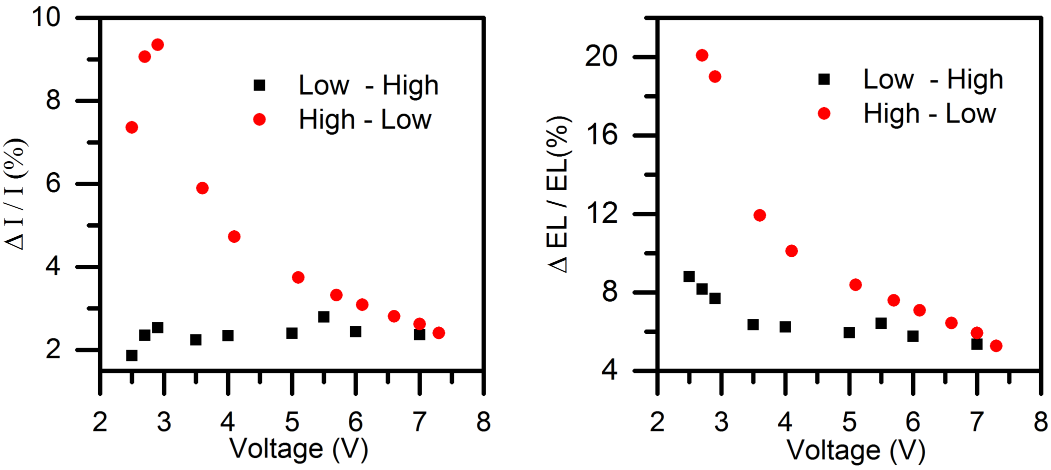

Figure 3.5: MC (left) and MEL (right) as function drive voltage. Low - High means that the measurement sequence is from low voltage to high voltage, High - Low means the opposite. The magnetic strength is 800 mT and two identical standard devices were used.

It can be seen that the conditioning effects are more prominent in low voltage regimes, as the MR and MEL measured from those two different cases begin to overlap at high voltages. This seems to suggest that stressing the device at low voltage has no effect on the MFE measured at high voltage whereas stressing the device at high voltage has a large effect on the MFE measured at low voltages. This is in agreement with the findings of Niedermeier et al. [35].

In order to have a deeper understanding of the conditioning effect, MFEs of a fresh standard OLED were measured at 3 V before and after different electrical stressing. The bias of the device followed the sequence: 3 V, 4 V, 3 V, 5 V, 3 V, 6 V, 3 V, 7 V, 3 V. The 3 V biases were applied for MFE measurements and the other biases were applied for stressing. The duration of each bias was approximately 37 minutes. A final MFE measurement was then taken at 3 V 16 hours after the above measurements to check if the conditioning effect reduces after the device was relaxed. The MC and MEL data obtained is shown in figure 3.6. As can be seen, the MC and MEL increases steadily as the stressing voltage is increased from 4 V to 7 V. The highest MC after 7

V stressing is approximately 5 times larger than that measured before any stressing and almost tripled in the case of the MEL. The enhancement remains even after 16 hours relaxation.

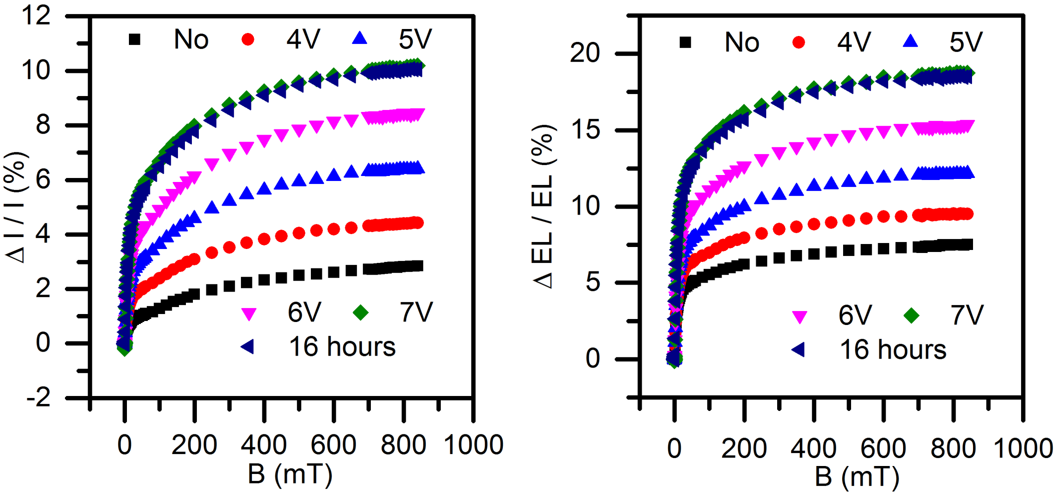

Figure 3.6: MC and MEL of a standard OLED measured at 3 V before any electrical stressing (black square); after 37 minutes stressing at 4 V (red dot), 5 V (blue up triangle), 6 V (pink down triangle) and 7 V (green diamond); and after 16 hours relaxation (navy left triangle).

Figure 3.7 shows the MC and MEL at 3 V bias, measured at 40 mT and 800 mT, as a function of the corresponding device current. It shows that the current decreases

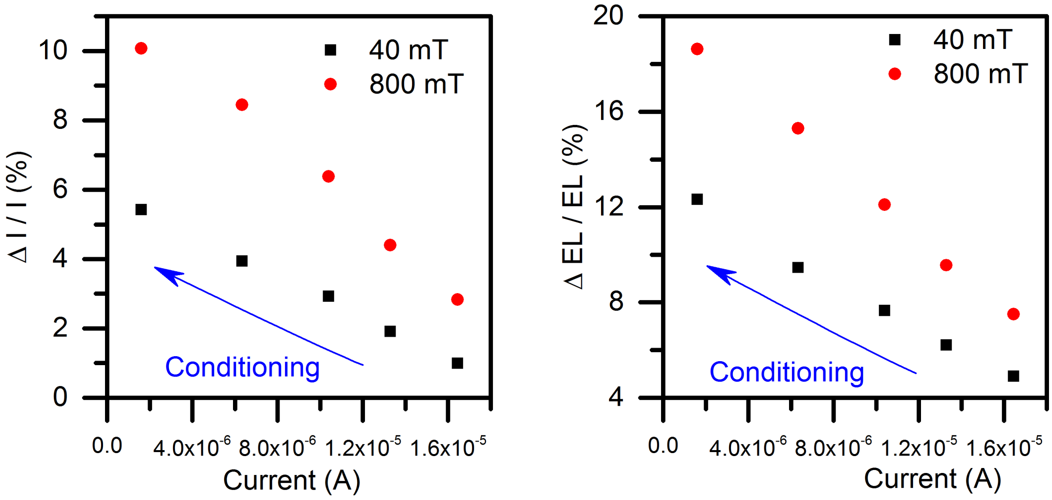

Figure 3.7: MC and MEL measured at 3 V as a function of device current. Only the data at magnetic fields of 40 mT and 800 mT is shown.

steadily after each stressing, and the corresponding MC and MEL increases. Since the MC and MEL are the percentage changes with and without applying a magnetic field, the increase of MC and MEL could just be a result of the decreasing denominators (current and EL). It should be noted that the numerators (ΔI and ΔEL) are not expected to remain the same. If both numerator and denominator decrease equally, the MC and MEL would remain unchanged. To achieve increased MC and MEL, a reasonable guess would be that the denominators decrease at a larger rate.

Figure 3.8 shows the ΔI and ΔEL as function of magnetic field. It is interesting to find that the ΔI measured after 4 V, 5 V and 6 V stressing is actually larger than the one measured without any stressing. The ΔI keeps increasing up until 5 V, the one after 6 V begins to decreases but is still about 18% larger than the no stress case. A large drop is shown after the stressing at 7 V. It is surprising that the current drops ~ 36% whereas the ΔI increases ~ 46% after the stressing at 5 V. No matter what defects the stressing process causes in the device, they decrease the current of the device but make the device more magnetic field dependent. In comparison, no increase is shown in ΔEL. However, it is also surprising that the EL intensity drops 23% after the stressing at 4 V whereas the ΔEL remains approximately the same. ΔEL keeps decreasing steadily from 5 V stress to higher voltages at a larger rate.

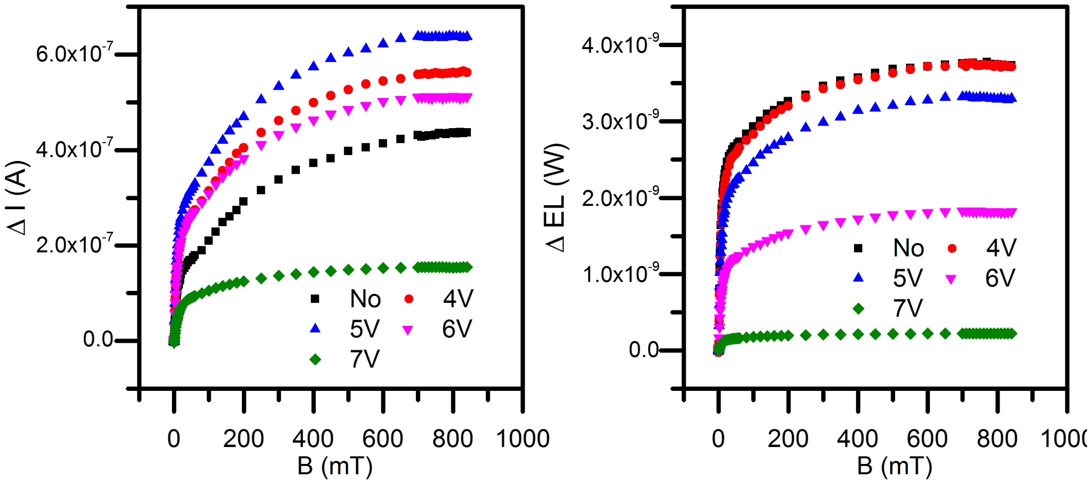

Figure 3.8: ΔI and ΔEL under different electrical stressing conditions are presented as a function of magnetic field. All measurements were taken at 3 V bias. The labels (No - 7 V) indicate the applied stressing bias before each MFE measurement taken at 3 V.

Although Niedermeier et al. [35] has suggested that for enhancement of MFEs to occur, the stressing current needs to be larger than the operating current, it is worth checking if there is any change in the MFEs when stressing the device at the same voltage for a longer time. To achieve that, a fresh standard OLED was used to conduct MFE measurements at 3 V 15 times. The duration of each measurement was 37 minutes, so the whole duration was $\sim$ 9.5 hours. Figure 3.9 shows the MC and MEL measured in sequence. It can be seen that both the MC and MEL increase gradually over the 9.5 hours duration although this increase is less significant than that found after stressing at higher voltages. The enhancement effect in MEL is smaller than in MC. For both the MC and the MEL, the difference between two consecutive measurements becomes smaller and smaller as the measurement proceeds. This seems to suggest that the stressing process can bring about defects in the device, at every voltage level, it simply takes longer for lower voltages to generate defects and the number of defects that can be generated at a particular voltage level is limited. Thus, the conditioning effects (MFE enhancements) at 3 V saturate in both MC and MEL as the measurement proceeds.

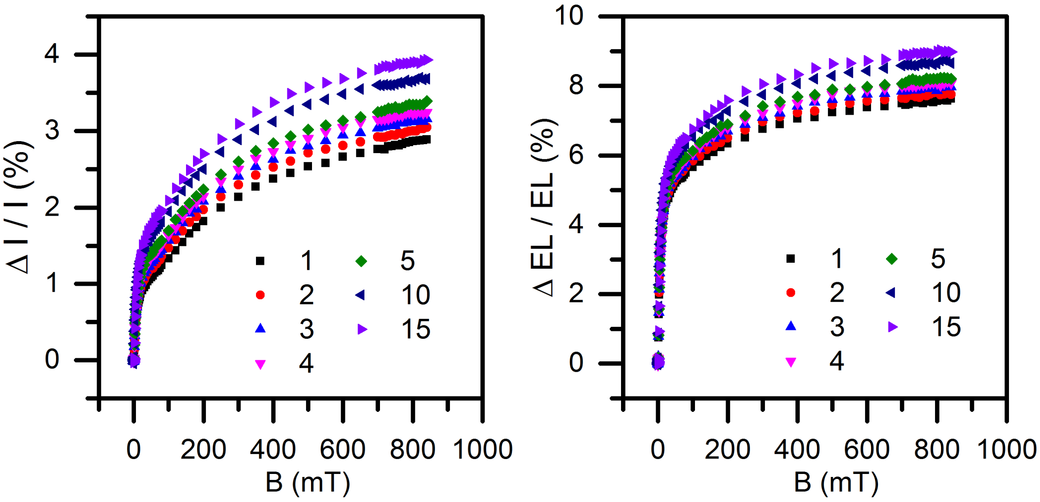

Figure 3.9: MC and MEL at 3 V measured in sequences. The numbers indicate the order and the device used is a standard OLED.

Comparison is made between the high voltage-stressed (H-stressed) device and the self-stressed (S-stressed) device. The data shown in figure 3.10 is extracted from that of figure 3.6 and 3.9. The first measured MC and MEL, labelled as No (black square) and 1 (blue triangle), from the H-stressed and the S-stressed, respectively, almost overlap each other with the S-stressed being slightly larger, which indicates that there is a good repeatability in MFE measurements on different devices. The second measurement of the S-stressed device, labelled as 2, shows only a small increase in both the MC and MEL. In comparison, the one measured after 4 V stressing in the H-stressed device (red dot), is comparably larger than the fifteenth measured one in the S-stressed device (green diamond). This means that fewer defects are generated by 9.5 hours of self-stress compared to 37 minutes stressing at 4 V. Thus, measuring the MFEs from low voltage to high voltage should not lead to significant stress, which should still be valid for studying the drive voltage dependent behaviour in our devices. As a result, all the MFEs to be discussed in the rest of this thesis were measured from low voltage to high voltage.

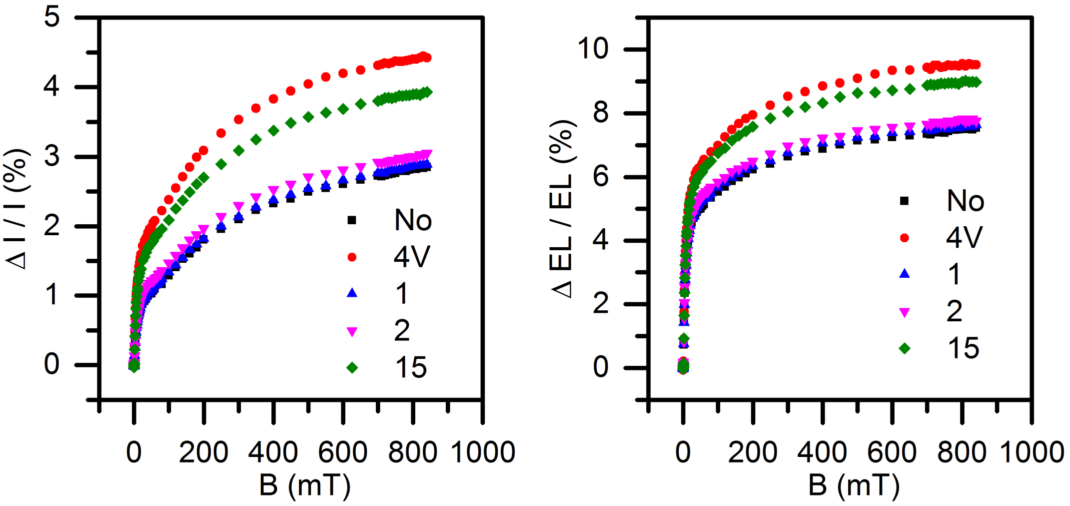

Figure 3.10: MC and MEL comparison between the H-stressed device and the S-stressed device. Data labelled as No and 4 V are taken from the H-stressed device, referring to measurement without stressing and after 4 V stressing, separately. Data labelled as 1, 2, and 15 are taken from the S-stressed device, referring to the first, the second and the fifteenth measurement accordingly.

Magnetic field effects on device A

Figure 3.11 shows the MEL as a function of drive voltage in device A. Figure 3.11(a) presents the MEL at lower voltages and figure 3.11(b) presents the MEL at higher voltages. Measurable MEL occurs from 2.3 V. Although noisy, it clearly features a rapid rise up to approximately 10% at low fields, which then levels off at high fields. This is comparable to the results found in a standard device in the literature [76] and has been attributed to the quenching of spin mixing between singlets and triplets by the magnetic field. The MELs at 2.3 V and 2.5 V are noisy, which is caused by the sensitivity limit of the photo detector used as the absolute value of EL at those voltages is small, of the order of 10^{-11} to 10^{-10} W. As the drive voltage increases, the MELs become smoother and the trend of the line-shape becomes clearer: a rapid rise at low fields followed by a small increase at high field. The same line-shape applies to higher voltages as shown in figure 3.11(b). From 3 V to 7 V, as the voltage increases, the overall magnitude of MEL decreases and the rate of decrease becomes smaller. It is worth noting that an additional feature occurs at the high field area: the rate of gradual rise at high fields (B > 50 mT) increases slightly at higher voltages, which, although subtle, can be seen by comparing the MELs at 3V and 4V.

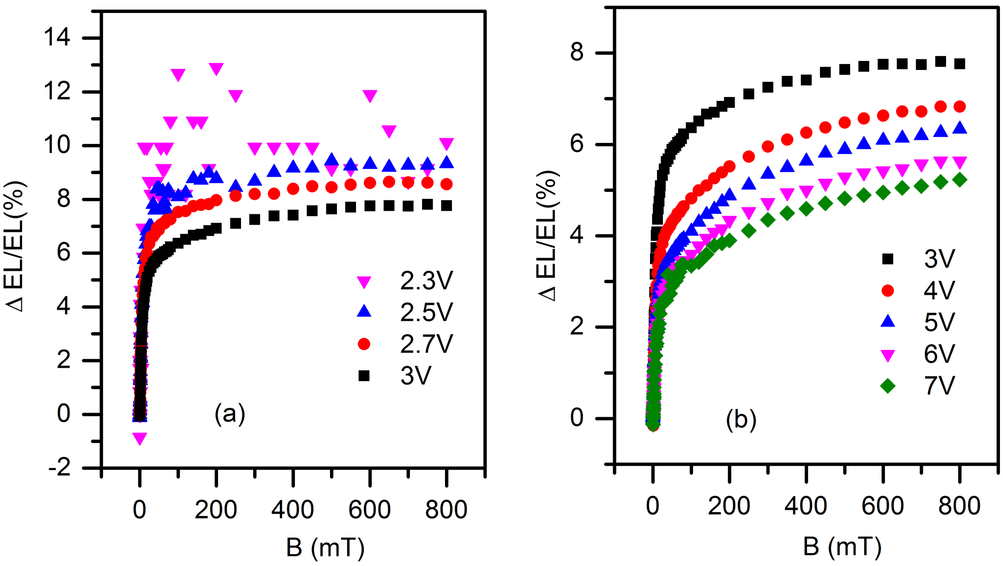

Figure 3.11: MEL of device A as a function of drive voltage: (a), low voltages; (b), high voltages. Device A has the structure of ITO/TPD/Alq_3/LiF/Al (standard device).

In order to investigate the change of the increasing rate at high fields, normalised MELs are presented in figure 3.12. Data from 2.3 V and 2.5 V are not presented because the noise may overshadow the information from other voltages. As has been discussed in the introduction section of this chapter, there are at least two processes

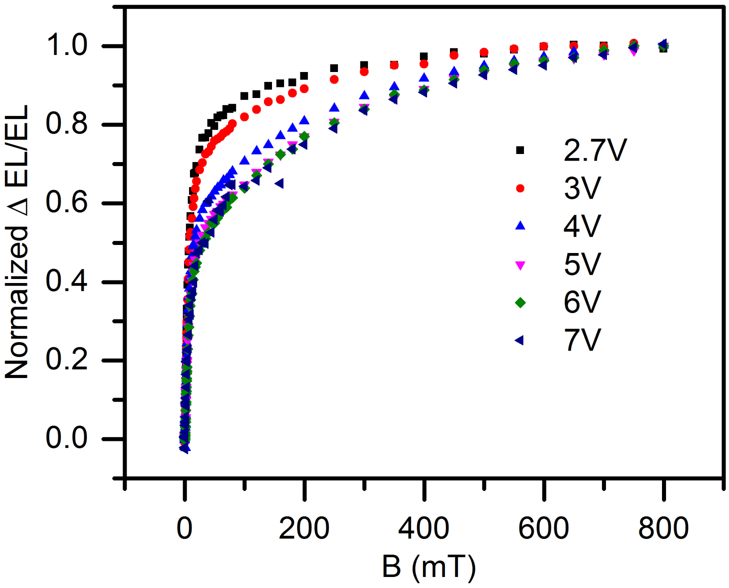

Figure 3.12: Normalised MEL of device A as a function of drive voltage. Device A has the structure of ITO/TPD/Alq_3/LiF/Al (standard device).

accounting for the MFE: one accounts for the low field rapid change, which has been attributed to the spin mixing process; and the other one accounts for the high field change, which is believed to be due to triplet exciton related processes. It can be seen clearly from the normalised MELs that as the voltage increases, the contribution of the second process to the overall magnitude of the MEL at 800 mT becomes larger. This trend is much clearer from 2.7 V to 5 V as the line-shapes at high field regime become steeper. Although the line-shapes from 5 V to 7 V still follow this trend, the change is negligible.

Magnetic field effects on device B

Figure 3.13 shows the MEL of device B as function of drive voltage. Measurable MEL did occur from 2.4 V but is not presented because of its noise. MELs of device B from 2.7 V to 4 V are presented in figure 3.13(a). Similar to device A, these MELs consist of a rapid low field rise up to $\sim$ 50 mT and a gradual rise at the remaining high fields. The overall magnitude of the MEL decreases steadily from 7.6% at 2.7 V to 5.7% at 4 V. What is worth noting is that the MELs at higher voltages, shown in figure 3.13(b), feature multiple line-shapes at high field regimes. At 4 V, 5 V and

6 V, the MELs have a similar line-shape to that seen in device A. As the voltage increases, in contrast to device A the high field effect in device B reduces, leading to a flat MEL at 8 V and then to a subtle decay as the voltage is increased further. This suggests that several processes are affected by the magnetic field at high field regimes during device operation. At low voltages, a positive process dominates the feature of high field MEL, whereas a negative process dominates as the voltage increases. At intermediate voltages, the two processes appear to cancel each other out.

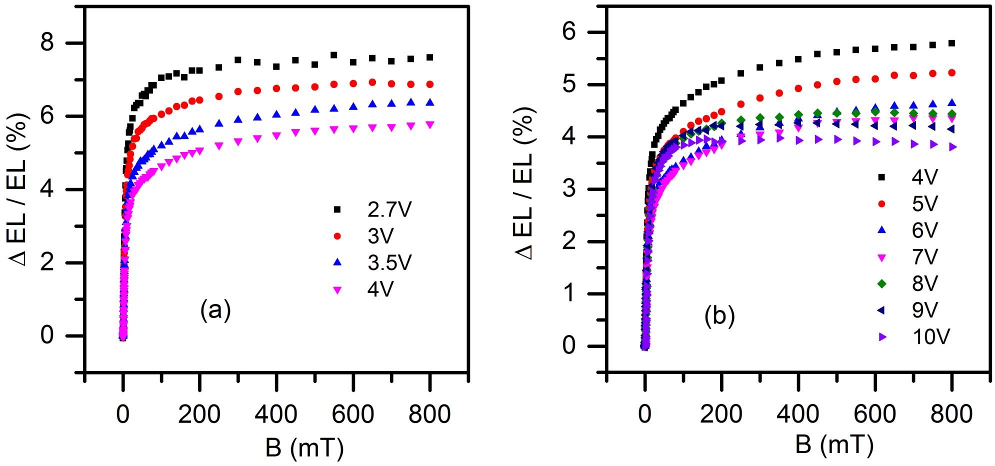

Figure 3.13: MEL of device B as a function of drive voltage. Device B has the structure of ITO/PEDOT/TPD/Alq_3/LiF/Al.

Figure 3.14 illustrates the normalised MELs of device B, corresponding to the MELs in figure 3.13. From figure 3.13(a) one can see the dependence of magnitude on drive voltage clearly, however, it is hard to tell the subtle difference in the line-shapes. After normalisation, shown in figure 3.14(a), it can be seen that the high field component increases slightly from 2.7 V to 4 V. Figure 3.14(b) shows the normalised MELs from 4 V to 10 V, the black horizontal line is a guide to the eyes. It can be seen that the MELs demonstrate the same trend as that shown in figure 3.13(b); as the voltage increases, the line-shapes at high fields change from small positive rise to subtle decay, which indicates the transition from a dominant positive process to a negative process.

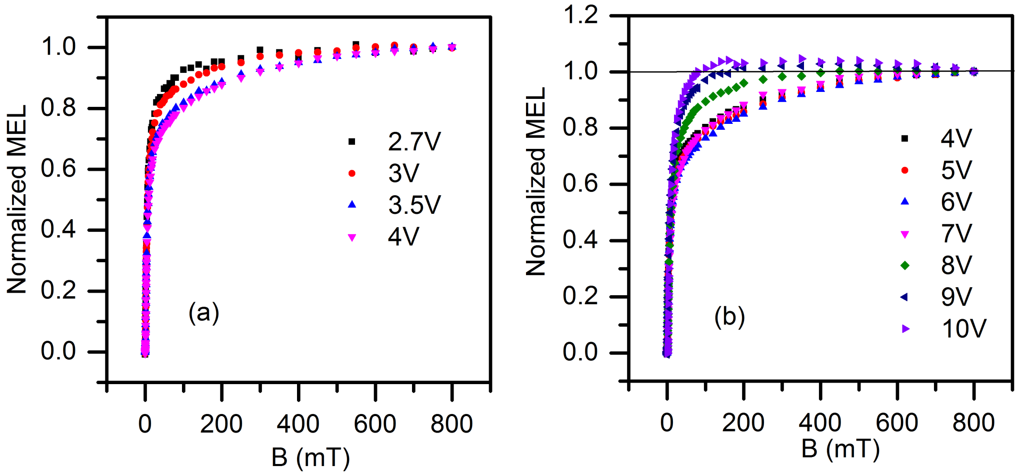

Figure 3.14: Normalised MEL of device B as a function of drive voltages. Device B has the structure of ITO/PEDOT/TPD/Alq$_3$/LiF/Al.

The literature discussed in the introduction section of this chapter has suggested that the high field MEL decay is widely attributed to the triplet-triplet annihilation process which occurs when large triplet density is achieved. The subtle negative component observed in device B might share the same mechanism, because larger triplet concentration can be achieved in device B as opposed to device A due to the presence of the PEDOT layer in device B. The presence of PEDOT layer improves the hole injection ability whilst the electron injection remains as good as that of the device A, which may improve the exciton formation rate, and the triplet concentration. As a result, TTA may exist in device B and the magnetic field effect on TTA produces the negative MEL process. Zhang et al. [40] showed the effect of triplet-charge carrier interaction effect on the line-shapes of MC, and it has been shown in the discussion of efficiency that at large current density, there exists significant exciton charge carrier interaction that accounts for the efficiency roll off. It is likely that the high field decay in MEL is a result of magnetic field effects on exciton charge carrier interaction. Since the efficiency roll off in device B at large current density is comparable to that of device A, it is confusing why the high field MEL decay occurs in device B but not in device A. Compared to device A, a larger hole injection is expected to be introduced into the active layer by the presence of PEDOT, if the high field decay is due to exciton charge carrier interaction, it has to be exciton hole interaction. At this stage, it is not conclusive which process is the reason for the high field MEL decay.

Magnetic field effects on device C

Figure 3.15 shows the MELs of device C as a function of drive voltage. It consists of data showing the overall features of device C in a reasonable scale. It can be seen that the overall magnitude decreases as the voltage increases from 4 V to 11 V; the line-shapes at high fields change from a saturated trend at 4 V to a subtle decay at 7 V, which is similar to the transition of MEL from 8 V to 10 V in device B, shown in figure 3.13(b). As the voltage increases further, the high field decay becomes more and more significant, with the MEL reaching a negative value at 11 V and 800 mT. Data at lower voltages that are not shown in figure 3.15 have the same line-shape as that at 4 V, but with a larger overall magnitude. Noticeable MEL was achieved from 3 V, showing an overall positive trend with the noise decreasing as voltage increases.

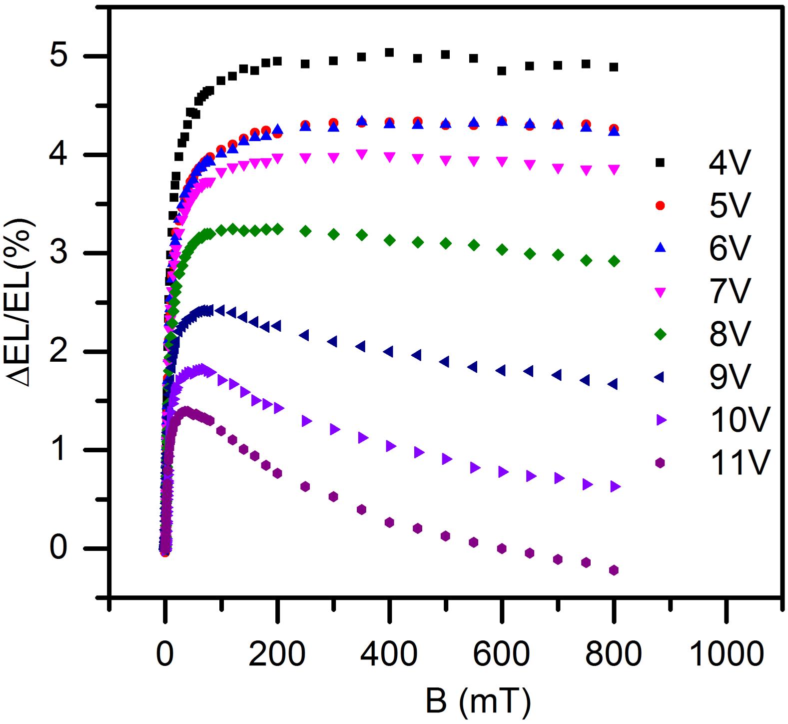

Figure 3.15: MELs of device C as a function of drive voltage. Device C has the structure of ITO/PEDOT/Alq_3/LiF/Al.

Device C shows no high field increase in MEL at all bias.

The astonishing high field MEL decays at high voltages in device C look extremely similar to those found by Liu et al. [44] at low temperature and high current density. However, can this high field decay in device C be attributed to triplet-triplet annihilation? Compared to device B, device C had the TPD layer removed so that the holes can be injected directly into the Alq_3 active layer. This means that more holes are present in the active layer of device C, which may again increase the probability of electrons meeting with holes, hence leading to a higher formation rate of excitons. As a result, large triplet concentration could be obtained in the device, much more significant triplet-triplet annihilation therefore, occurs and causes the astonishing high field MEL decay. This seems, however, unlikely, because if the increased number of holes in the active layer enhance the exciton formation rate, then the absolute efficiency should not be approximately 60% lower than that of a standard device (device A). One possible explanation is that there is a probability that the low efficiency could be due to the exceptionally high triplet concentration which reduces the number of molecules in the ground state and hence the number of singlets. Whilst this is unlikely, it cannot be ruled out.

Magnetic field effects on device D

Figure 3.16 shows the MEL of device D as a function of drive voltage. It consists of two parts: low voltages in figure 3.16(a) and high voltages in figure 3.16(b). It can be seen that MELs at low voltages show the same line-shape as that of device A, featuring a rapid low field rise and a gradual high field increase. Unlike the other devices in which the highest MEL magnitude reaches 9% and the magnitude of the MEL at low voltages decreases steadily as the voltage increases, the highest magnitude in device D is less than 2% and there is no clear trend of the change of the magnitude as the voltage increases from 12 V to 20 V. At higher voltage regimes, high field MEL decays occur. The line-shapes are similar to those observed in device C. Although the overall data is noisy due to the small EL intensity, the magnitude of the decays increase with voltage, reaching approximately -0.7% at 30 V, 800 mT.

The structure of device D is identical to that of device B apart from the difference in the cathode: device D has a high Fermi level metal, Au, as its cathode, which gives poor electron injection whilst device B has LiF/Al which features decent electron injection as can be seen from the high efficiency of the device. From the absolute efficiency shown in figure 3.2, one can see that the peak efficiency of device D is about 2.4×10^{-6}% and that of device B is about 0.9%. This means that the number of electrons injected into device D is at least 10000 times lower than that of device B. Therefore, in device D, the triplet concentration will be much reduced compared to devices A, B and C, and hence triplet-triplet annihilation cannot occur in this device. The observation of large MEL decay at high fields cannot be simply attributed to TTA on the basis of the similarity of the line-shape to that observed by Johnson et al. [20]. The fact that this high field MEL decay is seen to increase as the relative hole concentration in the Alq_3 layer is increased seems to suggest that the mechanism is related to exciton hole interaction. This may well be the reason of the lower efficiency of devices B and C compared to device A.

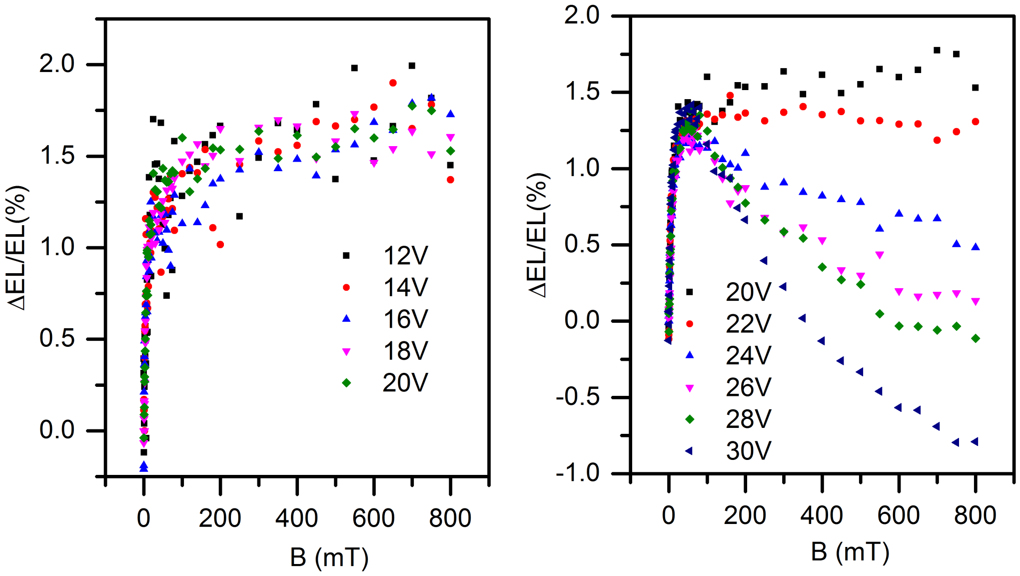

Figure 3.16: MELs of device D as a function of drive voltage. Device D has the structure of ITO/PEDOT/TPD/Alq_3/Au.

3.3.4 Fitting of magnetic field effects on efficiency

A function with the form of Eq. 1.11 (chapter 1) is called the Lorentzian function. It was first proposed in the literature [31], derived by considering the magnetic field dependence of the hyperfine interaction and spin-orbit coupling. A single Lorentzian function is often not sufficient to fit the MFEs as there may be more than one spin interaction process occurring. Functions with multiple Lorentzian components are, however, widely used in the literature to investigate the number of processes occurring in a device, the relative saturation fields of each process, as well as the strength of each spin process [30, 40, 48, 83]. Gillin et al. [30] used the double Lorentzian (Eq. 1.13) to fit their data, obtaining a low field component with a saturation field of 5 - 7 mT, and a high field component with a saturation field of $\sim$160 mT. Whereas Rolfe et al. [83] used a triple Lorentzian function to fit their data where they obtained two low field components and a high field component. The first low field component had a saturation field of 2.7 mT, and was attributed to the spin mixing between polaron pairs with singlet and triplet configurations. The second component had a saturation field of 11 mT, and was tentatively attributed to the spin mixing between singlets and triplets. The third component had the saturation field of 130 mT and was attributed to the triplet polaron interaction. In this section, Lorentzian functions are introduced to fit the relative efficiency data of devices A - D and extract the strength of the high field component. In order to keep the function as simple as possible, a double Lorentzian function is applied first. The function used is of the form of Eq. 3.3, where a_1 and a_2 are pre-factors, B_1 and B_2 are the saturation fields for different processes, and B is the magnetic field.

$$MFE = a_1(\frac{B^2}{B^2 + B_1^2}) + a_2(\frac{B^2}{B^2 + B_2^2}) \tag{3.3}$$

Figure 3.17 shows an example of the free double Lorentzian fitting of the relative change of efficiency ($\Delta\eta/\eta\%$) in device A at two biases with two different types of line-shape. It can be seen that the double Lorentzian function gives a reasonable fitting to the data at 2.7 V where the high field component is negligible. However, the data at 5 V which shows a clear high field rise is a poor fit. The saturating fields are B$_1$ = 3.9 mT and B$_2$ = 35 mT at 2.7 V and B$_1$ = 4.6 mT and B$_2$ = 98 mT at 5 V. The fact that the double Lorentzian function gives good fitting to all data in the work of Gillin et al. [30] might be a result of the range of fields measured: the highest field in that work is $\sim$ 300 mT whereas it is 800 mT in the current work. Alternatively, it may be due to the quality of the data: if the data at 5 V is noisy, the small variation of the fitting can easily be overshadowed by the noise and produce a "reasonable" fit.

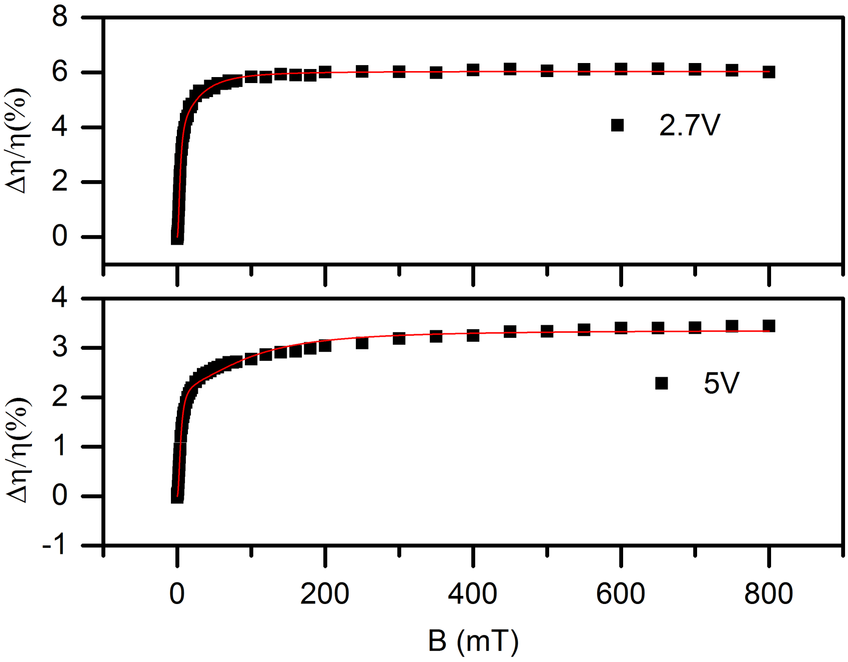

Figure 3.17: Free double Lorentzian fitting of the relative change of efficiency in device A measured at 2.7 V and 5 V.

As there are more than two processes occurring, it is reasonable to use a triple Lorentzian function, shown as in Eq. 3.4, to fit the data. Similar to Eq. 3.3, a_1, a_2, and a_3 are pre-factors whilst B_1, B_2 and B_3 are saturation fields.

$$MFE = a_1(\frac{B^2}{B^2+B_1^2}) + a_2(\frac{B^2}{B^2+B_2^2}) + a_3(\frac{B^2}{B^2+B_3^2}) \tag{3.4}$$

Figure 3.18 shows the free triple Lorentzian fitting of the relative change of efficiency of device A. It can be seen that both the saturation line-shape at 2.7 V and the high field rising line-shape at 5 V are well fitted. The saturation fields are B_1 = 3.6 mT, B_2 = 16 mT and B_3 = 106 mT for the data at 2.7 V and B_1 = 3.8 mT, B_2 = 21mT and

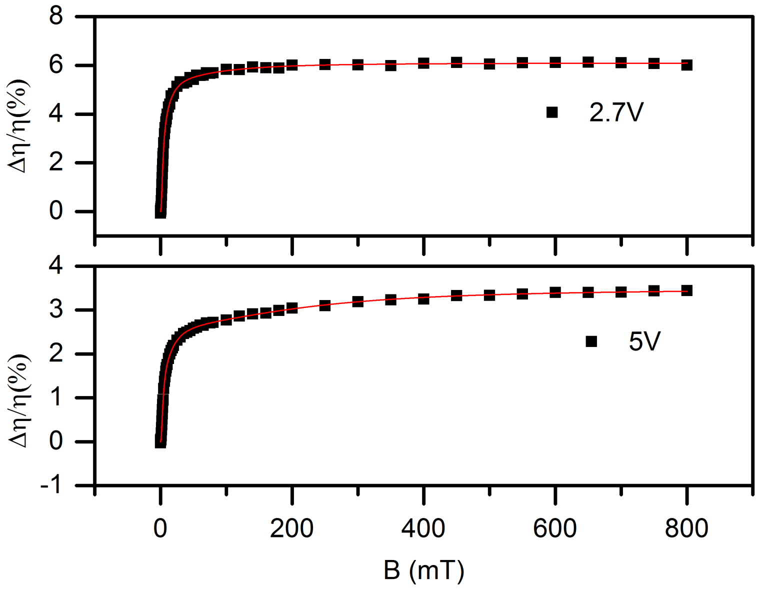

Figure 3.18: Free triple Lorentzian fitting of the related change of efficiency in device A measured at 2.7 V and 5 V.

B_3 = 231 mT for the data at 5 V. Similar to the work of Rolfe et al., there are two low field components and a high field component. The value of B_1 is well defined whilst there is a small variation in B_2 and a large variation in B_3. As a result, a constrained triple Lorentzian function is used to fit all efficiency data in device A. The constraints are: 3 mT < B_1 < 5mT, 10 mT < B_2 < 30mT, and B_3 > 100 mT. Since the variations in $B_1$and B_2 are small, the fitting is performed by setting B_1 and B_2 as shared parameters. That is, data from different voltages is fitted simultaneously with the same B_1 and B_2. Results show that all data can be fitted by the triple Lorentzian function. Figure 3.19 shows some of the representative fitting results of device A. The fitting parameters are summarised in table 3.1. A term called the high field strength (a_3%) is defined as the percentage ratio of a_3 to the sum of the absolute values of a_1, a_2 and a_3, shown as in Eq 3.5

$$a_3\% = \frac{a_3}{|a_1| + |a_2| + |a_3|} \tag{3.5}$$

By looking at the magnitude of this term, one can have a rough idea of the contribution of the high field process to the overall MEL. Figure 3.20 shows the high field strength of device A as a function of drive voltage. The high field strength increases with the drive voltage, which indicates that the contribution to the overall

MEL from this positive process increases with current density.

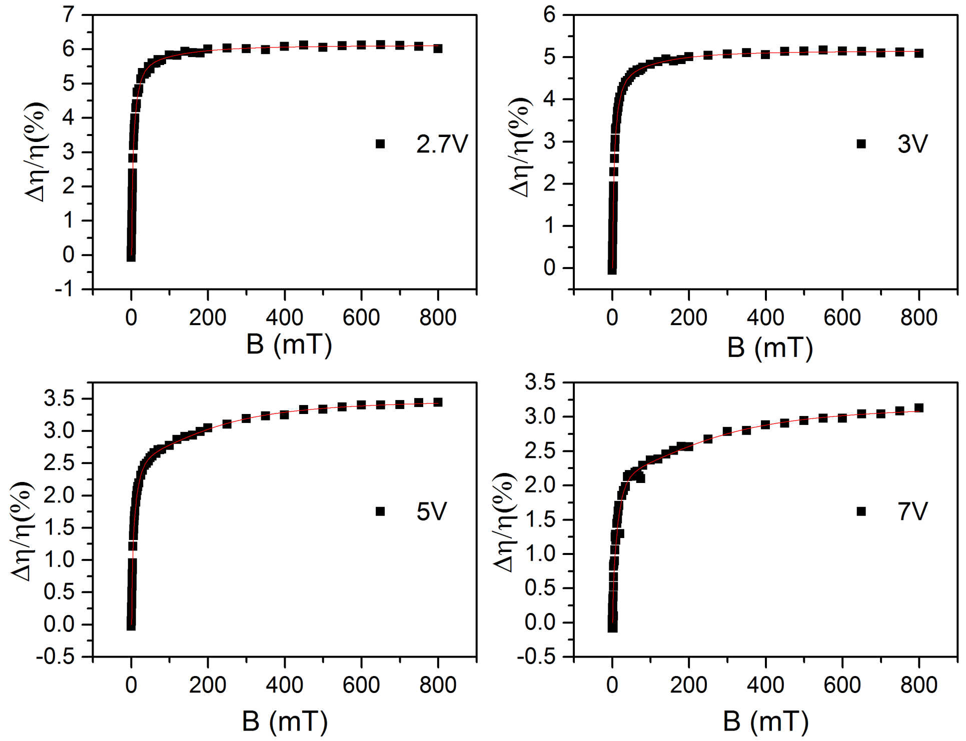

Figure 3.19: Constrained triple Lorentzian fitting results of device A at representative voltages.

Voltage (V)	a_1	a_2	a_3	B_1 (mT)	B_2 (mT)	B_3 (mT)
2.5	4.67±0.12	2.18±0.12	0.43±0.10	3.5±0.08	19±1.5	230±157
2.7	4.11±0.11	1.61±0.13	0.39±0.08	3.5±0.08	19±1.5	217±65
3	3.43±0.09	1.29±0.13	0.43±0.08	3.5±0.08	19±1.5	250±54
4	2.30±0.07	1.00±0.10	0.53±0.07	3.5±0.08	19±1.5	206±65
5	1.74±0.07	0.96±0.13	0.80±0.07	3.5±0.08	19±1.5	231±50
6	1.42±0.07	0.98±0.09	0.93±0.08	3.5±0.08	19±1.5	229±42
7	1.03±0.07	1.24±0.09	0.90±0.08	3.5±0.08	19±1.5	270±58

Table 3.1: Fitting parameters of device A obtained from constrained triplet Lorentzian fitting

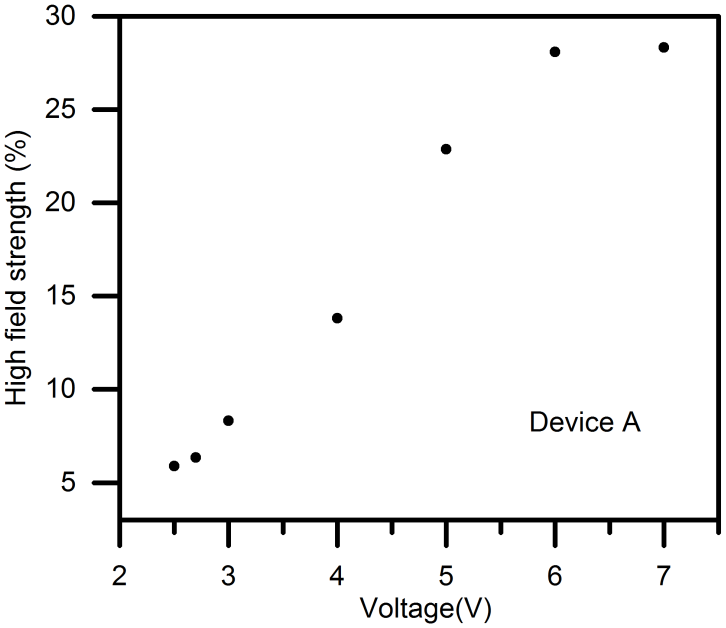

Figure 3.20: High field strength of device A as a function of drive voltage.

Triple Lorentzian fitting was applied to device B similarly. It was first fitted by free parameters. As there are multiple line-shapes in the relative change of efficiency, data featuring different line-shapes are initially freely fitted to find out the final parameters for the constrained fitting. Figure 3.21 shows the free triple Lorentzian fitting of the relative change of efficiency of device B. Data at 3.7 V and 7 V represent line-shapes with different level of high field rises whilst data at 9 V represents line-shapes with subtle decay. They are well fitted. The saturation fields are B_1 = 3.4 mT, B_2 = 20 mT and B_3 = 163 mT at 3.7 V, B_1 = 3.7 mT, B_2 = 20 mT and B_3 = 140 mT at 7 V, and B_1 = 4.2 mT, B_2 = 23 mT and B_3 = 800 mT at 9 V. As in the case of device A, B_1 and B_2 are well defined whilst B_3 has a big variation. Ideally, two high field components should be included in the function to fit the data as it is very clear that there are positive and negative high field components present this device. However, when using a function with four components to fit the data, as there are 8 free parameters in the function, reliable fitting is difficult due to mutual dependence occurred among the parameters. In order to extract and compare the high field strength among the devices, a triple Lorentzian function was still applied to fit device B. The constraints

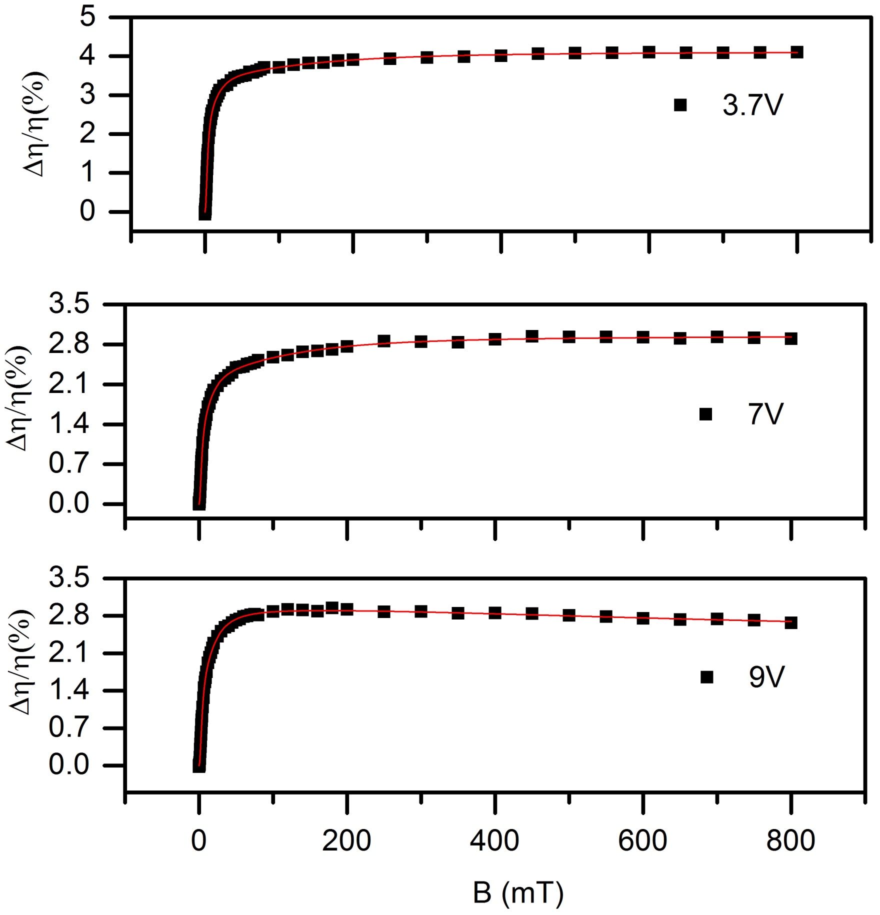

Figure 3.21: Free triple Lorentzian fitting of the related change of efficiency in device B measured at 3.7 V, 7 V and 9 V.

on the parameters were set as: 3 mT < B_1 < 5 mT, 10 mT < B_2 < 30 mT, and B_3 > 100 mT, same as device A. B_1 and B_2 are also set as shared parameters (MEL at all voltages use the same B_1 and B_2). The fitting results at some representative voltages are shown in figure 3.22. Reasonably good fits are obtained and the fitting parameters are summarised in table 3.2. The high field component, a_3, changes from positive value to negative. The high field strength (a_3%) as a function of drive voltage is shown in figure 3.23. It firstly increases with voltage, reaching a peak of 28% at 6 V, it then starts to decrease as the voltage increases further and becomes negative from 8 V onwards. The increase of the strength from 3 V to 6 V indicates the increase of the dominating positive component at low voltages; from 6V on, a competing negative component occurs, weakening the strength of the positive high field process; from 8

V onwards, the negative high field component begins to dominate and the strength begins to increase in a negative direction. This in agreement with the line-shapes of the normalised MELs of this device, shown in figure 3.14.

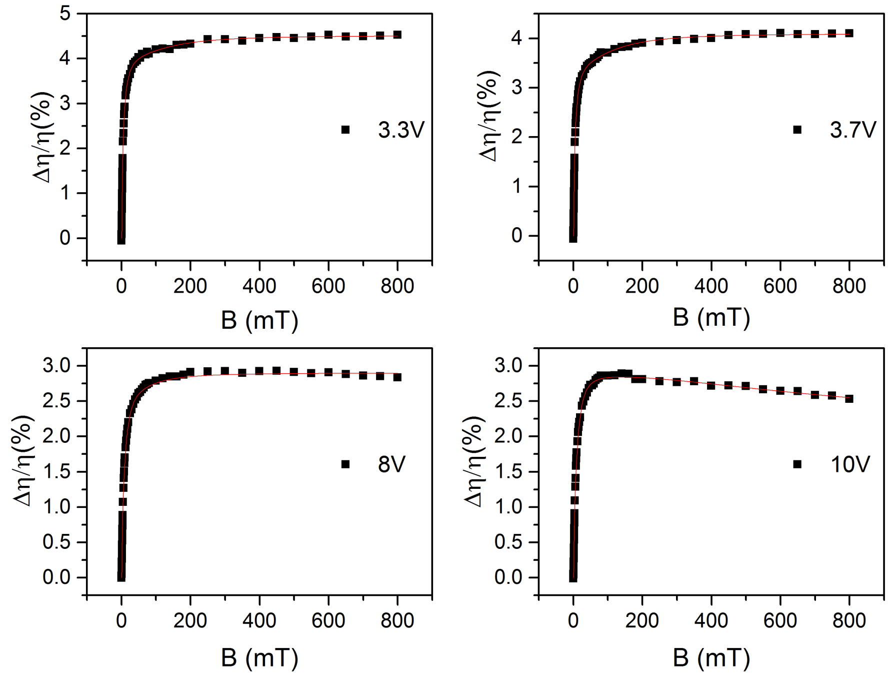

Figure 3.22: Constrained triple Lorentzian fitting results of device B at representative voltages.

Voltage (V)	a_1	a_2	a_3	B_1 (mT)	B_2 (mT)	B_3 (mT)
3	3.51±0.02	1.10±0.04	0.49±0.03	3.4±0.02	16±0.33	115±9.3
3.5	2.83±0.02	0.94±0.03	0.49±0.02	3.4±0.02	16±0.33	135±12
4	2.47±0.02	0.89±0.03	0.55±0.02	3.4±0.02	16±0.33	136±10
5	2.15±0.02	0.92±0.03	0.64±0.02	3.4±0.02	16±0.33	184±11
6	1.79±0.02	0.87±0.03	0.68±0.02	3.4±0.02	16±0.33	195±12
7	1.44±0.02	0.96±0.03	0.55±0.02	3.4±0.02	16±0.33	135±13
8	1.48±0.02	1.23±0.04	-0.20±0.02	3.4±0.02	16±0.33	103±20
9	1.48±0.02	1.42±0.02	-0.49±0.03	3.4±0.02	16±0.33	800±1E6
10	1.49±0.02	1.40±0.02	-0.60±0.14	3.4±0.02	16±0.33	716±159

Table 3.2: Fitting parameters of device B obtained from constrained triplet Lorentzian fitting

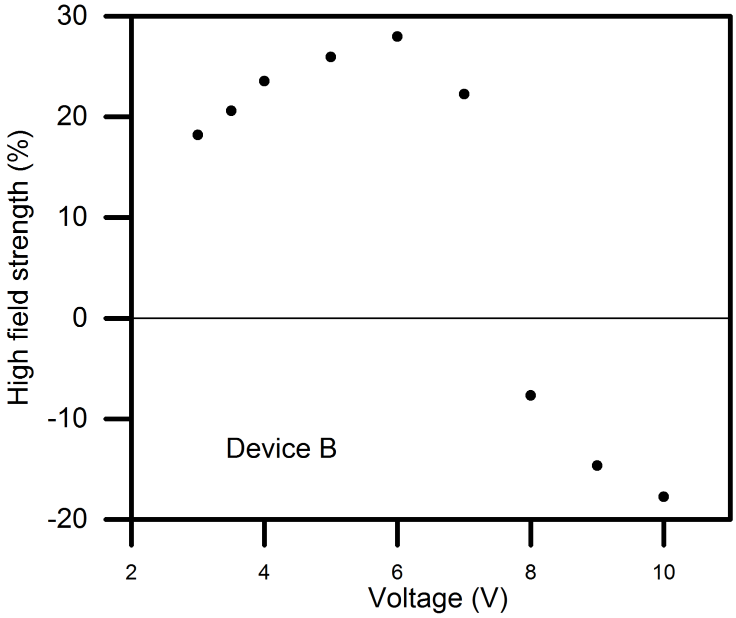

Figure 3.23: High field strength of device B as a function of drive voltage.

For the fitting of devices C and D, the same constraints used. Since larger variations are found in the B_1 and B_2 of the later two devices, they are not set as shared parameters, which mean the data at different voltage can use different value. Some representative fitting results are presented in figure 3.24. Figure 3.24(a) shows the fitting of device C at 5 V, 8 V and 11 V which feature different levels of decay. Figure 3.24(b) shows the fitting of device D at 18 V, 24 V and 30 V which feature a transition from positive rise to moderate decay, then significant decay. Fitting parameters are summarised in table 3.3 for device C and table 3.4 for device D.

Figure 3.25 shows the high field strength of devices C and D obtained from constraint triple Lorentzian fitting. The value of a_3 in device C are all negative, which indicates that the negative process dominates the high field effect at all measurable voltages. As the voltage increases from 5 V to 11 V, the magnitude of the high field strength increases from -9.5% to -77.8%. For device D, the dominant process before 20 V is positive, and the competitive positive and negative processes cancel out at 20 V. As the voltage increases further, the negative process dominates and the magnitude of the strength increases with voltage up to -63.4% at 30 V.

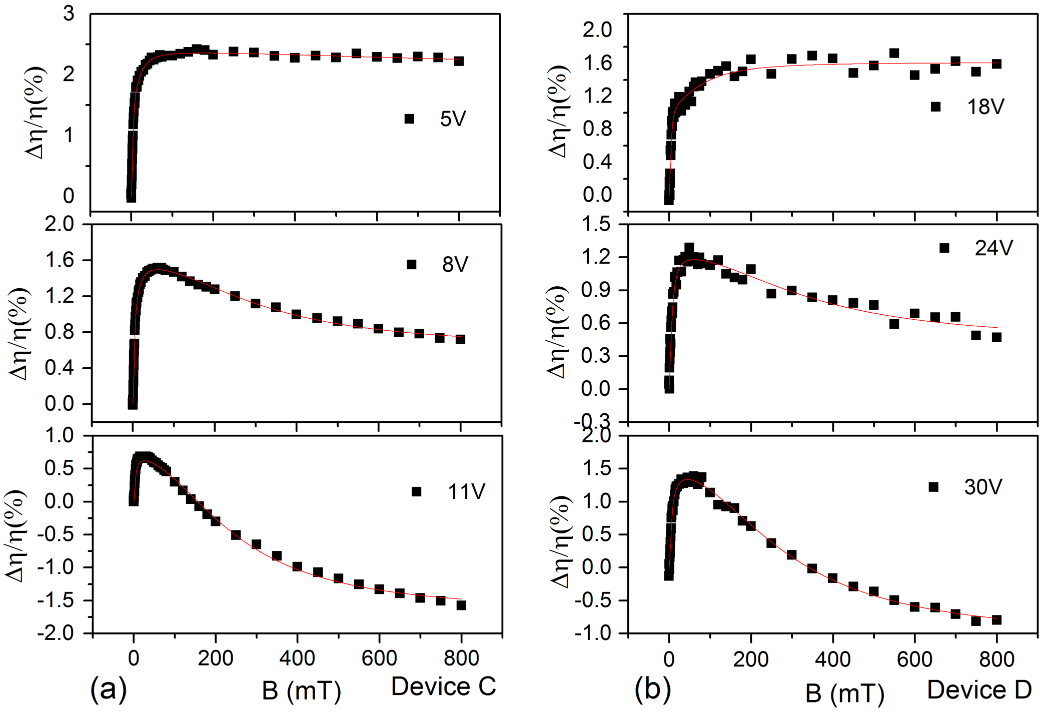

Figure 3.24: Triple Lorentzian fitting of the relative change of efficiency: (a), fitting of device C measured at 5 V, 8 V and 11 V; (b), fitting of device D at 18 V, 24 V and 30 V.

Voltage (V)	a_1	a_2	a_3	B_1 (mT)	B_2 (mT)	B_3 (mT)
5	1.75±0.04	0.63±0.04	-0.25±0.21	3.6±0.09	23±2.3	800±600
6	1.50±0.03	0.64±0.03	-0.33±0.10	3.4±0.06	23±1.0	800±228
7	1.31±0.03	0.59±0.02	-0.54±0.02	3.3±0.05	19±0.8	380±28
8	1.13±0.04	0.43±0.03	-0.94±0.01	3.4±0.09	17±1.6	318±10
9	0.84±0.07	0.31±0.07	-1.49±0.01	3.2±0.05	16±2.4	271±6.3
10	0.60±0.17	0.26±0.16	-2.0±0.03	3.0±0.54	12±5.0	258±7.8
11	0.52±0.23	0.15±0.22	-2.36±0.03	3.1±0.83	15±11	248±8.3

Table 3.3: Fitting parameters of device C obtained from constrained triplet Lorentzian fitting.

Voltage (V)	a_1	a_2	a_3	B_1 (mT)	B_2 (mT)	B_3 (mT)
16	0.64±0.66	0.48±0.64	0.70±0.12	3.3±2.1	15±9.7	350±118
18	1.09±0.11	0.13±1.0	0.39±1.01	3.5±0.5	27±19	319±129
20	1.08±0.09	0.47±0.12	0±0.17	4.1±0.5	20±19	250±0
22	0.85±0.09	0.52±0.08	-0.33±0.38	3.2±0.4	19±4.6	320±850
24	0.53±0.26	0.67±0.25	-0.79±0.06	3.3±1.1	14±3.2	348±49
26	0.71±0.17	0.57±0.16	-1.32±0.04	3.7±0.8	16±5.1	270±21
28	0.90±0.13	0.47±0.11	-1.67±0.04	3.8±0.5	19±6.1	297±18
30	1.05±0.23	0.41±0.21	-0.52±0.04	4.2±0.7	16±7.4	292±10

Table 3.4: Fitting parameters of device D obtained from constrained triplet Lorentzian fitting.

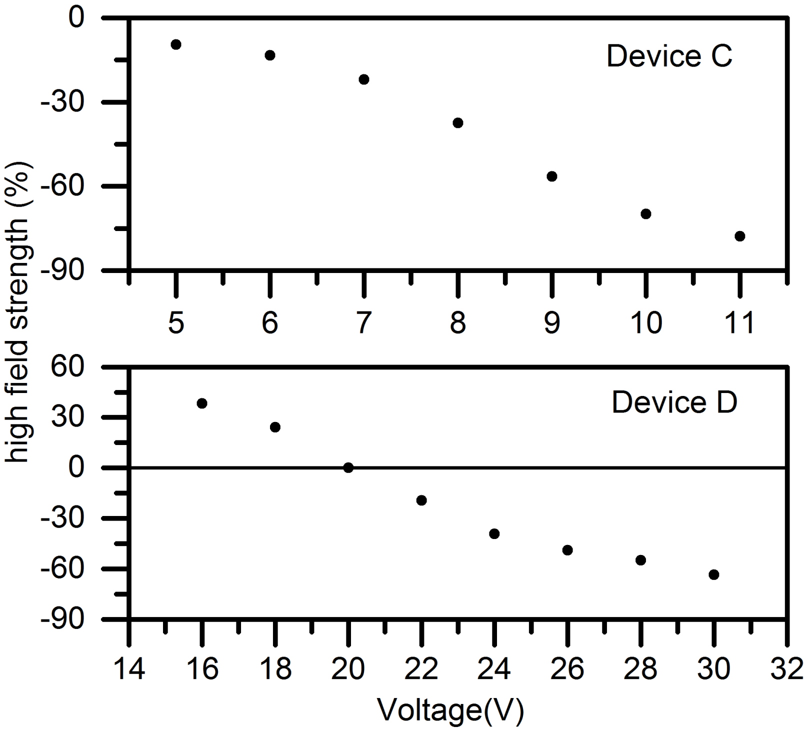

Figure 3.25: The High field strength as a function of drive voltage in device C and device D.

It can be seen that there is a beautiful transition in the high field strength versus drive voltage behaviour of devices A - C. As the voltage increases, the high field strength of device A increases all the way in the positive direction, that of device B increases first in the positive direction then starts to decrease towards negative direction, and that of device C increases all the way in the negative direction. This pattern is completely consistent with that of the hole to electron ratio in these devices. The cathodes of devices A - C were kept the same whilst their anodes were adjusted to enhance hole injection. As a result the hole to electron ratio increases, which on one hand can potentially increase the exciton formation rate, and on the other hand increase the hole exciton interaction rate which may contribute the negative high field component.

The average value of the saturation fields for devices A - D are summarised in table 3.1. The error values are calculated standard deviations. It should be pointed out that when calculate the average B_3 of device C, the very large value at 5 V and 6 V (800 mT) are not included in. It can be seen that B_1 is well defined in all devices. B_2 is less confined, but still in qualitative agreement with each other. B_3 shows considerably larger variation both within devices themselves and among devices. This is not surprising because a function with three components is used to fit MELs with four components. For MELs with a large increase or decay at high fields, the use of triple Lorentzian function is valid because their competitive high field processes are negligible. For MELs with a subtle increase or decay at high fields, the effect of their competitive processes cannot be ignored. The triple Lorentzian function used thus produces very large B_3 value.

Device	A	B	C	D
B_1 (mT)	3.5	3.4	3.3 ± 0.2	3.6 ± 0.4
B_2 (mT)	19	16	18 ± 4	18 ± 4
B_3 (mT)	233 ± 20	143 ± 30	295 ± 50	306 ± 33

Table 3.5: Averaged characteristic fields for devices A - D extracted from triple Lorentzian fitting

3.4 Conclusion of this chapter

There exist multiple magnetic field dependent processes in a working diode, in particular, at least two the high field dependent processes. Literature points to possible processes that may be subject to high field dependence. These include the triplet-charge carrier interaction (TCI) and the triplet-triplet annihilation (TTA). The TCI process is widely used to explain the high field MC which may possess both a positive rise and a negative decay at high fields depending on the structure of the device and the measuring conditions. The TTA process is widely used to explain the high field MEL decays in systems where possible high triplet concentration can occur. Since both processes involve the concentration of excitons, which achievable via varying the structure of a device, the idea of investigating the exciton charge carrier interaction using Alq_3 based organic systems is motivated.

In all, four devices were designed and built. The thickness of organic layer was kept the same for all the devices, making the horizontal comparison among devices possible. IVL data demonstrated that device A, featuring comparable charge carrier injection from both the anode and the cathode, is the most efficient device of all. The MEL of this device all feature a positive rise at high fields, and the rate of the high rise seems to increase with drive voltage. Device B, featuring improved hole injection, shows multiple line-shapes in its MELs at high fields. A small high field rise occurs at low voltages which then transforms gradually to a subtle high field decay as voltage increases. The occurrence of the multiple line-shapes indicates that more than one high field dependent processes is present in a working device. A positive process dominates the rise at low voltages and a negative process dominates the decay at high voltages. Device C, featuring further improved hole injection, shows of no high field rise even at low voltages; the MELs at low voltages show of a saturated high field line-shape. As the voltage increases the high field MEL begins to decay and the magnitude of the decay is enhanced at larger voltages. The decay ends up with a negative value at 11 V, which shows a similar line-shape as that found in low temperature high current density Alq_3 devices. Although the possibility of the existence of TTA is reduced by comparing the absolute efficiencies of device C and device A, the probability cannot be completely ruled out. However, the occurrence of significant high field decays in device D makes it certain that the high field decay in the devices cannot the be due to TTA. Because of $\sim$ 10000 times lower electron injection in device D suggests that there cannot be a high enough triplet concentration for TTA to occur. The fact that the high field MEL decay is seen to increase as the relative hole concentration in the Alq_3 layer is increased suggests that it is associated with exciton - hole interaction. The positive high field component is then tentatively attributed to exciton - electron interactions.

Lorentzian functions were used to fit the magnetic field effects on efficiency. A double Lorentzian function was used first to fit the data of device A. Free fitting of devices at their representative line-shapes were performed before the constrained fitting. The range of the saturation values at the chosen voltages were then used as the constraints for their fitting. Results show that a well defined saturation field, B_1, and a less constraint saturation field, B_2, were found for all devices. The range is 3 mT < B_1 < 4mT and 10 mT < B_2 < 30 mT. Large variation is present in the high field component, which could be due to the fact that a function with three components was used to fit MELs which had four components. Pre-factors obtained from the constrained fitting were interpreted in the form of the percentage ratio of a_3 to the sum of the absolute values of a_1, a_2 and a_3, they are called the high field strength. The high field strengths in device A are all positive and increase with voltage, and for device C, they are all negative and their magnitude increase with voltage. MEL is dominated by the positive process in device A by the negative process in device C. In comparison, the high field strengths of devices B and D both demonstrate a transition from positive to negative, and the positive process and the negative process dominate at different voltage regimes in device B and device D.

Chapter 4

Time resolved MFEs in standard Alq_3 based devices — evidence of magnetic field effects on triplet-charge carrier interaction

4.1 Introduction

In chapter 3, it has been shown that in Alq_3 based devices, the exciton-charge carrier interaction is responsible for the behaviour of the line-shapes of MEL at high fields. Specifically, the exciton-hole interaction is proved to be responsible for the high field MEL decay whilst the exciton-electron interaction is suggested to be responsible for the high field MEL rise. Although the triplet-charge carrier interaction was believed to dominate, there is no direct evidence to support it. In this chapter, magnetic field effects on transient EL are presented in order to provide more information about the exciton-charge carrier interaction.

Studies on exciton-charge carrier interaction were mainly carried out by investigating the effect of charge carriers on the magnitude and/or lifetime of photoluminescence (PL) or delayed PL [87, 98]. Results of prompt PL revealed the existence of singlet exciton–charge carrier interaction while that of delayed PL revealed the existence of triplet exciton–charge carrier interaction. It is well known that excitons can interact with charge carriers via three routes: scattering, quenching and dissociation [21, 99].

The fingerprints of the latter two processes are decreased magnitude and lifetime of PL (or delayed PL).

4.2 Experiment

Research has shown that in Alq_3 the average lifetime of singlets and triplets are 10 ns [13, 100, 101] and 25 μs [14], respectively. The idea of this experiment is to take advantage of the long lifetime of triplets as opposed to that of singlets. This means that at an applied voltage pulse, it takes triplets approximately three orders of magnitude longer to reach their equilibrium state at the ring edge, additionally, triplets live longer at the falling edge. Thus the time dependence of the MFEs can be used to investigate the role of triplets.

Devices used in this chapter are standard Alq_3 based diodes with the structure of ITO / TPD (50 nm) / Alq_3 (50 nm) / LiF (1 nm) / Al (100 nm). The devices were measured via the transient magnetic field electroluminescence using the apparatus described in section 2.4.2. To avoid possible electrical conditioning effects, the measurement was arranged to start from low voltages to high voltages. At each voltage, transient EL was measured from low magnetic fields to high magnetic fields (the order of fields does not affect the results). To improve the quality of the EL, each EL was acquired through averaging data achieved from 1000 pulses. To ensure a moderate measuring speed, all driving pulses were set to a frequency of 1 kHz. The measurements were conducted using pulse widths of 10μs, 20μs and 50μs. Only results measured using 50 μs pulses were presented in this chapter, as it was found that the behaviour of MEL is independent of the pulse width.

4.3 Results and discussion

4.3.1 Transient EL

Figure 4.1 shows the transient EL measured at pulses from 5 V to 10 V. It can be seen that the EL intensity increases rapidly as the amplitude of the pulse increases. This is due, directly, to the number of charges injected from the electrodes increasing with voltage as the energetic injection barriers are reduced at larger bias. Detail of the EL at the rising edge is shown in the inset. It can be seen that as the voltage increases,

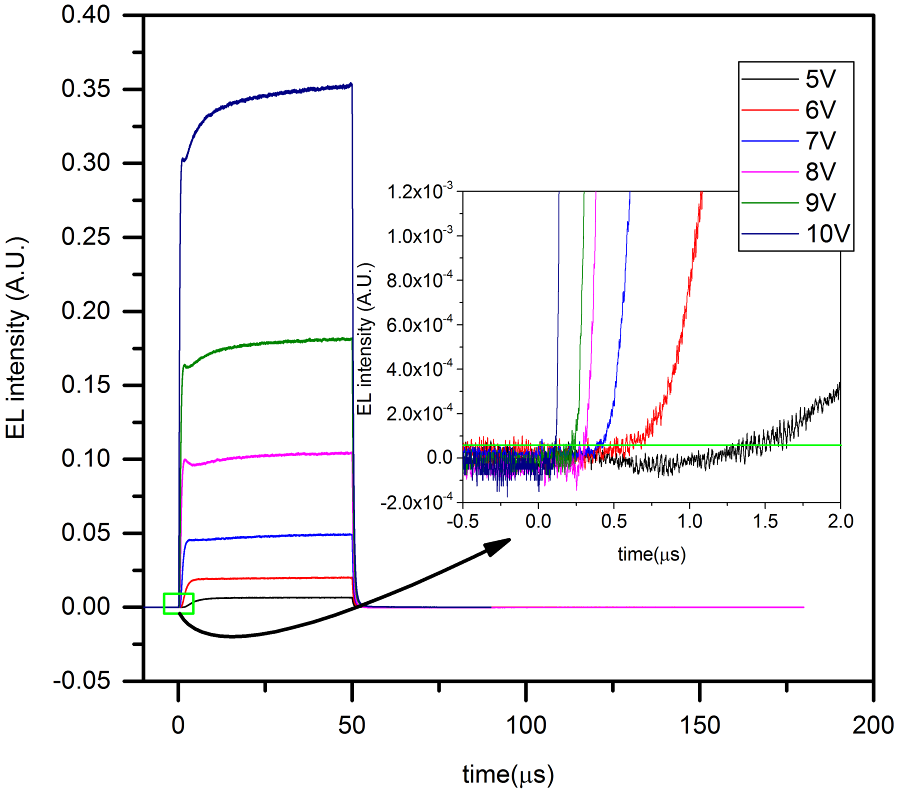

Figure 4.1: Transient EL measured from 5 V to 10 V. The inset shows the section defined by the green rectangular under magnification. It shows the EL rising edge where the intersection of the green line and data defines the charge transit time.

the rising edge becomes steeper, and the onset time of the EL decreases as the transit time of charges through the device is reduced. The reason for the steeper edge at higher voltages is same as that of the increasing EL intensity at higher voltages. That is, the highly voltage dependent charge carrier injection from the electrodes. The reason for the faster arrival is due to the increased electrical field, coupled with fact that the charge carrier mobility is strongly dependent on the electric field across the device [94, 102–104]. The arrival time is defined as the time of the point at which the EL intensity starts to increase rapidly. As the steepest rising edge occurs at 10 V, the arrival time of 10 V is well defined (110 ns). The EL intensity at the turn on point of 10 V is chosen as a standard of measuring the arrival time at other voltages. The EL intensity was found to be 5.3×10^{-5} A.U. and a horizontal green line was drawn at this intensity. This line crosses the EL curves of the other voltages and the time of these intersect defines the onset time for each voltage. The onset times represent the time at which the electrons and holes first meet in the device. It is also called charge transit time. The charge transit time at each voltage is shown in table 4.1.

Voltage(V)	5	6	7	8	9	10
Time(s)	1.34×10^{-6}	5.44×10^{-7}	4.28×10^{-7}	3.1×10^{-7}	2.45×10^{-7}	1.1×10^{-7}

Table 4.1: Charge transit time at different voltages.

Many works have used the transient EL method to estimate the mobility of charge carriers [105–111]. In the current device, it is commonly believed that the light emitting zone is near the TPD/Alq_3 interface [112–114]. Since hole mobility in TDP is approximately 2 orders of magnitude higher than electron mobility in Alq_3 [105, 115], the charge transport time is determined by the time that electrons take to transport from the cathode to the TPD/Alq_3 interface. Knowing the thickness of the Alq_3 layer and the built in potential (V_{bi}) of the device, one can calculate the electron mobility in Alq_3 using Eq. 4.1, where μ represents mobility, d the thickness of the Alq_3 layer, τ the EL arrival time, E the electric field across the device, V the applied voltage and V_{bi} the built in potential of the device.

$$\mu = \frac{d}{\tau \times E} = \frac{d^2}{\tau \times (V - V_{bi})} \tag{4.1}$$

The V_{bi} used in this section was a literature value of 2.2 V [42]. Figure 4.2 shows a Poole-Frenkel plot of electron mobility in Alq_3 calculated using the transient time shown in table 4.1. It can be seen that the electron mobility is of the order of 10^{-5} cm/Vs and strongly dependent on the electric field. This result is comparable to that measured by Zhang et al. using the time of flight method [94].

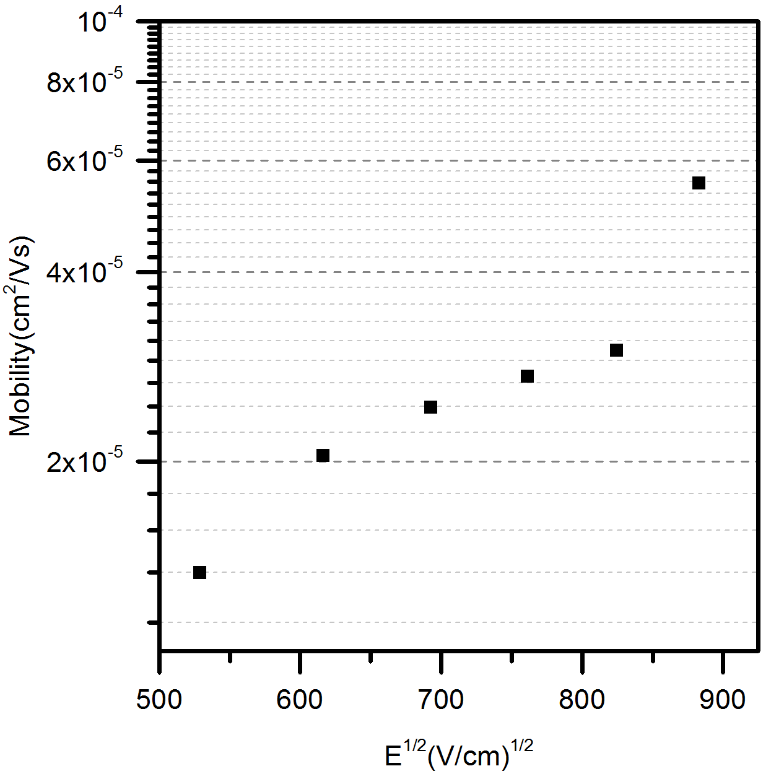

Figure 4.2: Pool - Frenkel plot of electron mobility in Alq_3 calculated from equation 4.1.

It can be seen from figure 4.1 that there are short time small spikes or overshoots appearing in the ELs from 8 V to 10 V. It seems that upon the turn on of the pulses, the EL intensity increases spontaneously to a peak, it then decreases slightly and starts to approach the steady state value slowly. Many works have found large spikes in the transient ELs of OLEDs, some are at the rising edge [116, 117] and some are at the falling edge [117–121]. The interpretation of the overshoots at the rising edge was attributed to the recombination of one type of charge carrier injected with another type of charge carrier remaining, somehow, in the device [116]. As for the overshoots at the falling edge, they were commonly attributed to the recombination of electrons and holes trapped at the interfaces or in the bulk [118–121]. Taking Ref [116] as an example, they found a clear overshoot in DCM doped Alq_3 device EL, as opposed to a pure Alq_3 device where the overshoot was absent. By measuring the EL at different wavelengths, they further confirmed that the overshoot is associated with the emission from the DCM molecules and double pulses showed that the overshoot does not exist in the second pulse as long as the gap between the two pulses is smaller than 1 μs. They suggested that this overshoot is due to the electrons trapped on DCM molecules. To be specific, as the hole mobility in the hole transport layer is much higher than that of electrons in the Alq_3, after injection, holes will arrive at the organic interface near the Alq_3 layer. Those holes then recombine with the electrons trapped on the DCM molecules and emit light instantaneously. As the electrons trapped near the interface run out, the light intensity starts to drop, forming the overshoot. In the case of the small overshoot in figure 4.1, a similar mechanism can be applied. Since the holes injected are faster, they will arrive at the interface earlier, some then enter the Alq_3 layer. However, due to their poor mobility in the Alq_3, they will build up near the interface and there will be a distribution of holes near the interface which tails off within the Alq_3. When electrons move towards the interface, they recombine first with the tail and then reach the higher concentration at the interface, therefore a small increase in the EL is expected. Since the accumulated holes can weaken further injection of holes, a peak is expected during this period.

4.3.2 MFE on transient EL

Figure 4.3 shows one set of raw data taken at 10 V under magnetic fields of 0 mT and 400 mT. Each set of data contains three EL measurements: the EL measured at the target field, 400 mT, in this case; and the EL measured at 0 mT before and after the measurement at 400 mT. These are shown as 0 mT (B) and 0 mT (A) in the figure where B and A denote before and after, respectively. The average of the two ELs measured at 0 mT was taken as the final EL measured at 0 mT. This is to compensate for possible device drift during the measuring process, similar to the study of steady state MFE discussed in chapter 3. It can be seen, however, that the two EL results measured at 0 mT overlap each other completely, which indicates that unlike the steady state MFE measurement, the drift in the transient MFE measurement is negligible. Comparison of the red and blue lines shows that a clear increase was obtained in the EL intensity on applying the 400 mT magnetic field.

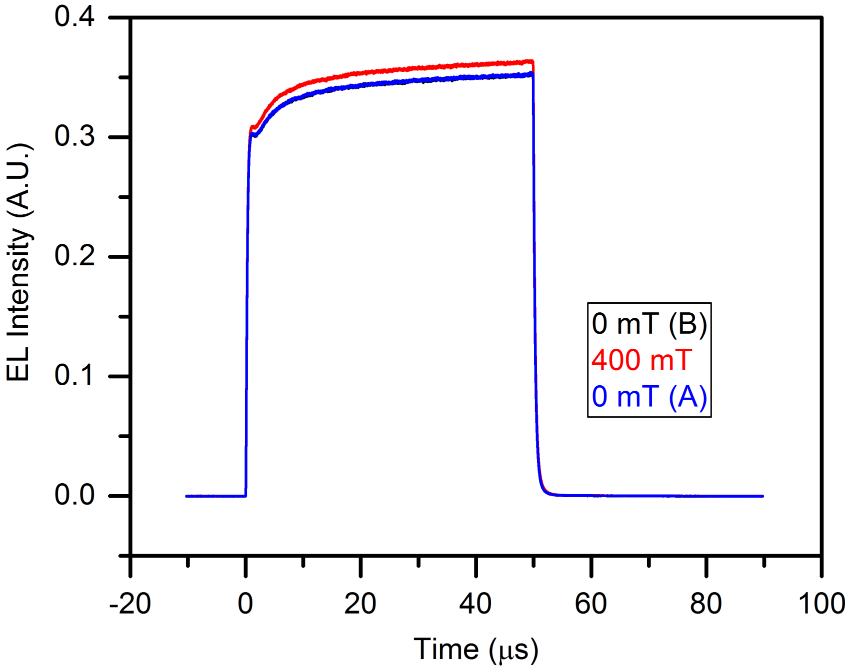

Figure 4.3: One set of raw data measured at 10 V under fields of 0 mT and 400 mT where B and A denote zero field measurements before and after, respectively.

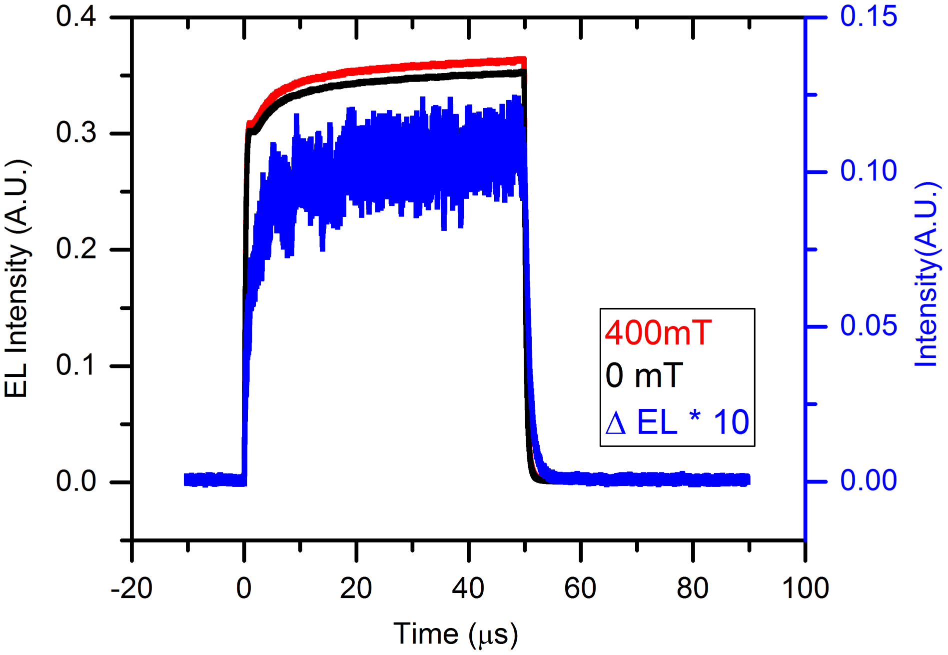

Figure 4.4: Calculated ΔEL (blue line) at 10 V bias. It is the difference between the EL measured at 400 mT (red line) and the average zero field result (black line).

Figure 4.4 shows how the data was used to calculate the MEL at 10 V bias and 400 mT magnetic field. The red line is the EL measured at 400 mT which is the same as the one in figure 4.3, the black line is the averaged EL at 0 mT, and the blue line is the ΔEL, that is, the difference of the two (having been magnified by a factor of 10). The MEL (ΔEL/EL) is calculated using Eq. 4.2.

$$MEL = \frac{\Delta EL}{EL\ (0\ mT)} \times 100\% \tag{4.2}$$

Figure 4.5(a) illustrates an overview of the MEL calculated from the data in figure 4.4. It can be seen that the MEL at the time regimes before the EL turn on and $\sim 15\ \mu$s after the EL turn off is very noisy. It can also be seen that a negative offset is present in the regime before the EL turn on and a positive to negative "spike" is present at $\sim 73\ \mu$s. The largest noise level is as high as 1.5×10^3%. This is simply because that there is no EL signal before the pulse and the signal is very small after the pulse

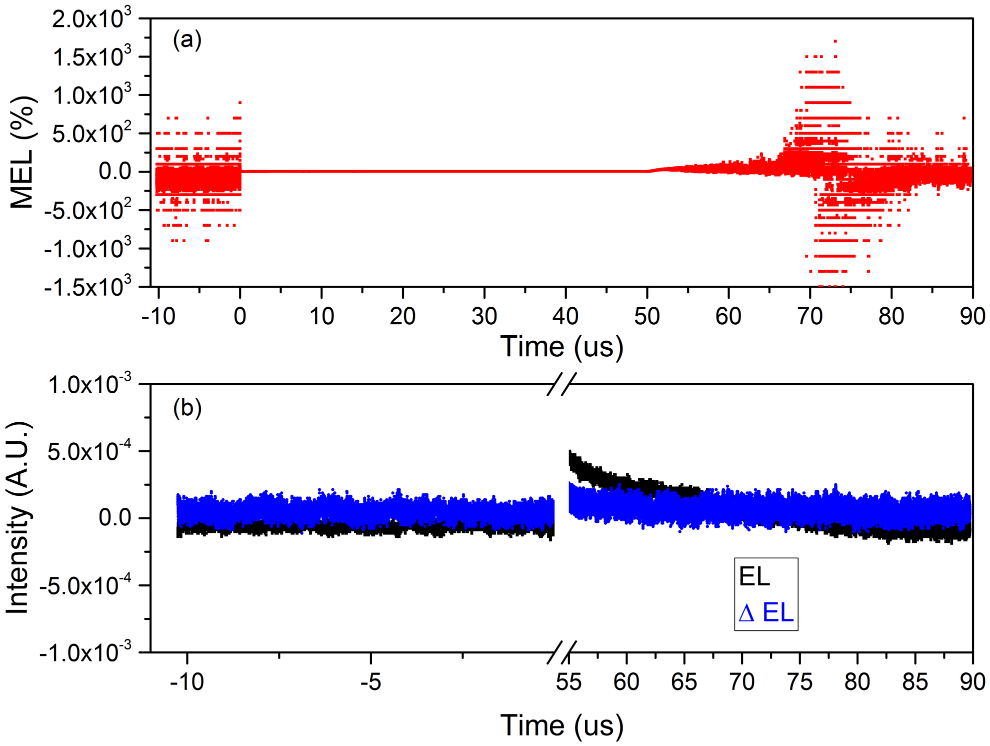

Figure 4.5: (a), an overview of the MEL calculated using data in figure 4.4; (b), ΔEL and EL at the time regime of -10 to 0 μs and 55 to 90 μs.

which can be seen directly in figure 4.5(b), in raw data of those two regimes. Both EL and ΔEL at those regimes are around zero, resulting in a large percentage difference. It can also be seen that at the regime before the pulse, there is a small negative offset present in the EL data, which accounts for the negative offset of MEL in figure 4.5(a). In the regime after the pulse was turned off, figure 4.5(b) shows that as the EL signal is slowly decaying away it crosses the ΔEL at around 73 μs, therefore a largest noise is expected to occur at this regime. Since the EL is positive before the intersection and negative after, positive and negative "spike" like noise is present in figure 4.5(a).

Figure 4.6 shows the MEL in the regime of 0 μs to 70 μs. The 0 μs is defined as the EL turn on point. The inset is an enlarged view of the MEL during the first 20 μs. It can be seen from the inset that as the pulse is turned on, a prompt MEL of 1.2% was obtained almost instantaneously. The MEL then increases slowly for $\sim$ 5 μs, levelling off at approximately 3.3%. After that, the MEL remains approximately constant until the pulse was turned off. After the pulse was turned off, the MEL starts to increase rapidly in an approximately "linear" way for $\sim$ 3 μs before being lost in the noise. The discrete appearance of the scattered noise is a result of digitisation due to the limited resolution of the oscilloscope as the signal in this regime is approaching zero.

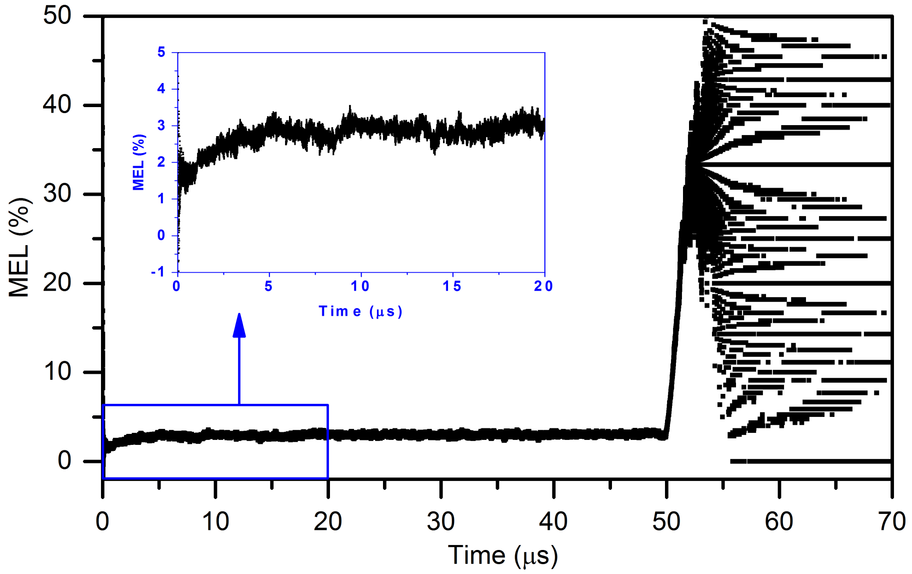

Figure 4.6: The active regime of the MEL at 10 V bias under a field of 400 mT. The inset is a magnification of the 20 μs of data.

In order to understand the behaviour of the MEL, the discussion will be divided into three parts: the gradual increase at the beginning of the pulse, the flat part of the pulse and the rapid increase part after the pulse was turned off. They are called "MEL at the rising edge", "MEL at the 'steady' state" and "MEL at the falling edge", respectively, and will be discussed in the following sections accordingly.

4.3.3 MEL at the rising edge

In this section, the dependence of the MEL at the rising edge on magnetic field and drive voltage is discussed.

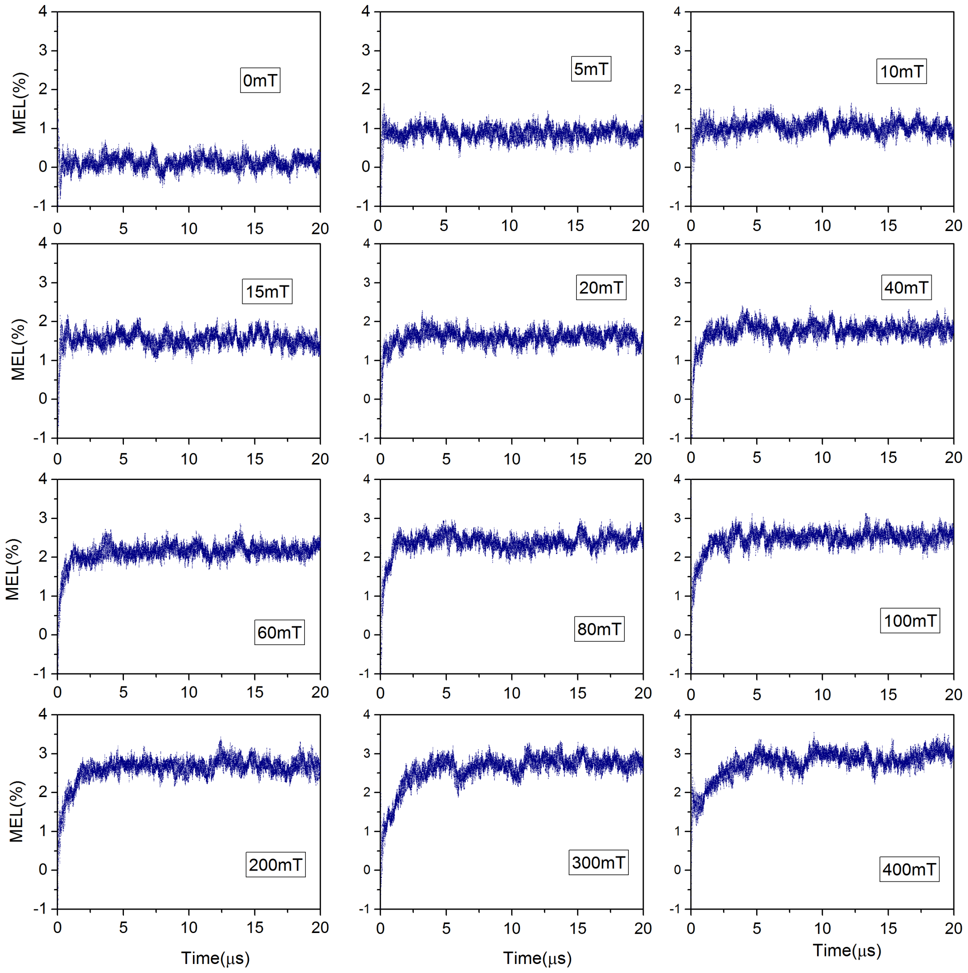

Figure 4.7: The MEL of a 10 V bias at the rising edge under different magnetic fields.

Figure 4.7 shows the MELs of a 10 V pulse at the rising edge under different fields. It can be seen that there is no field dependence at 0 mT, which indicates that the results are reliable. As the field increases to 5 mT, subtle prompt MEL occurs instantaneously and no observable rising feature is found at the beginning of the pulse. The gradual rise occurs from 20 mT onwards and it becomes more significant at higher fields.

Figure 4.8 shows the first 20 μs of the MEL under different drive voltages. Since the gradual rise is more significant at higher fields, only the data measured at 400 mT is presented. The vertical scale of 5 V and 6 V is larger than the other higher voltages.

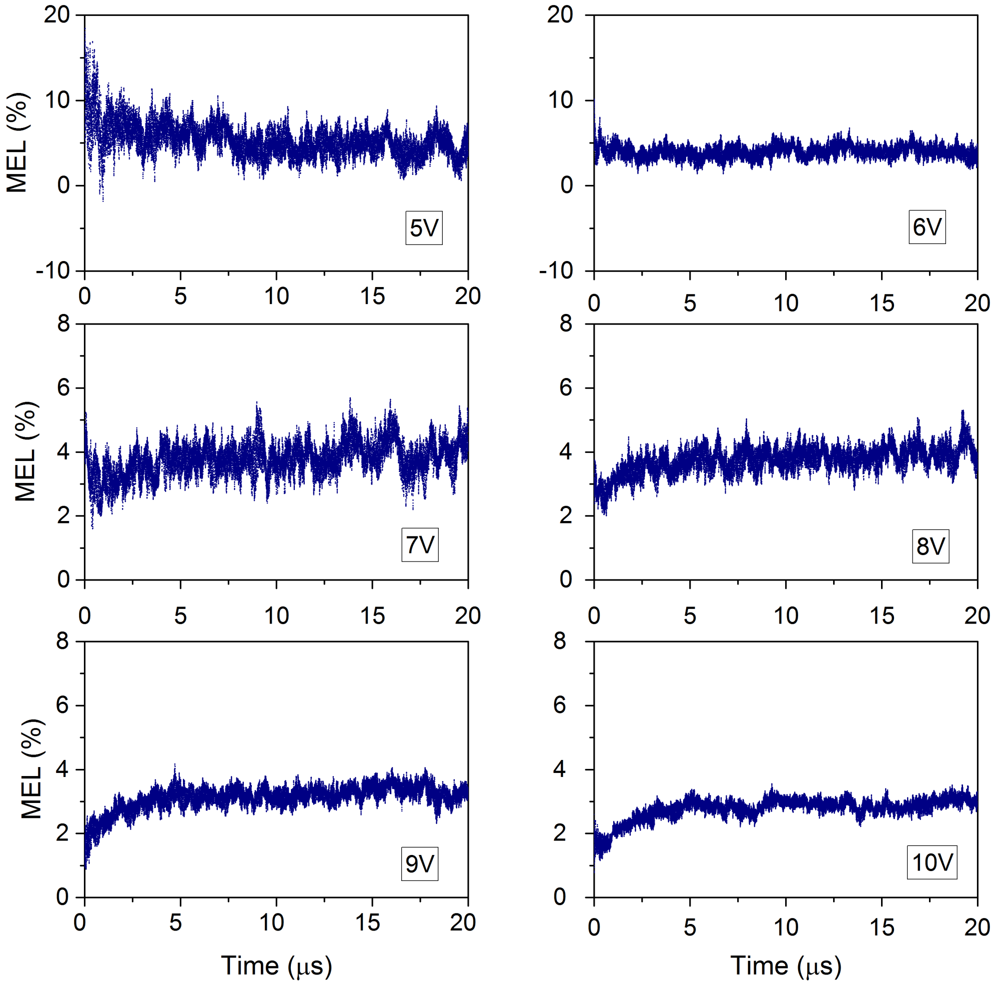

Figure 4.8: The MEL at the rising edge under different drive voltage. The magnetic field is 400 mT.

It can be seen that the noise level decreases as the voltage increases. This is due to the fact that the EL intensity increases dramatically with drive voltage, as shown in figure 4.1, hence the signal to noise ratio is improved. There are well defined gradual increases present at 9 V and 10 V. Following the trend, subtle rises can also be seen at 7 V and 8 V. Instead of showing the rise feature, the 5 V data shows a decay like feature at the beginning. No visible decay or rise is present at 6 V. As discussed in the last section, the MELs calculated before 0 μs are just scattered noise (refer to figure 4.5(a)). If the offset of the noise is a large positive value, it will relax slowly to approach the real MEL value once the EL is turned on. This might be the reason for the small decay in the 5 V MEL data. If we expand the beginning of the data of 7 V and 8 V, this small decay is also present. Because the EL intensity at 5 V is very small, the decay effect is clearer and lasts longer. We can therefore conclude that the gradual rise of the time over 5 μs is positively correlated to the drive voltage.

The fact that this gradual rise has a high field dependence indicates that it is related to exciton-charge carrier interaction; and the fact that it takes time of the order of microseconds to reach the “steady” state suggests that it is associated with triplets, because it takes triplets approximately the same scale of time to build up their population. We, hence, tentatively attribute this small rise to the triplet-charge carrier interaction, and how it is affecting the EL intensity is to be discussed in section 4.3.6.

4.3.4 MEL at the steady state

To study the MFE in the "steady" state, MELs at a particular voltage were averaged over the time range of 10 μs - 50 μs and taken as a function of magnetic field over the range of 0 mT - 400 mT. Figure 4.9 (a) shows the averaged MEL at different applied voltages. It can be seen that the overall magnitude decreases slightly as the voltage increases, which is of the same trend as that obtained from the steady state MFE method, discussed in chapter 3. A comparison of the MELs obtained at those two methods at the same range of voltages are shown in figure 4.9 (b). Although the data obtained from the transient method (solid) is not as smooth as that obtained from the steady state method (open), they share exactly the same line-shape, featuring a rapid low field rise and a gradual high field increase. It, therefore, suggests that they also share the same mechanism. That is, the quenching of the hyperfine field mixing between singlet and triplet contributes to the rapid low field rise and the exciton-charge carrier interaction contributes to the gradual high field increase.

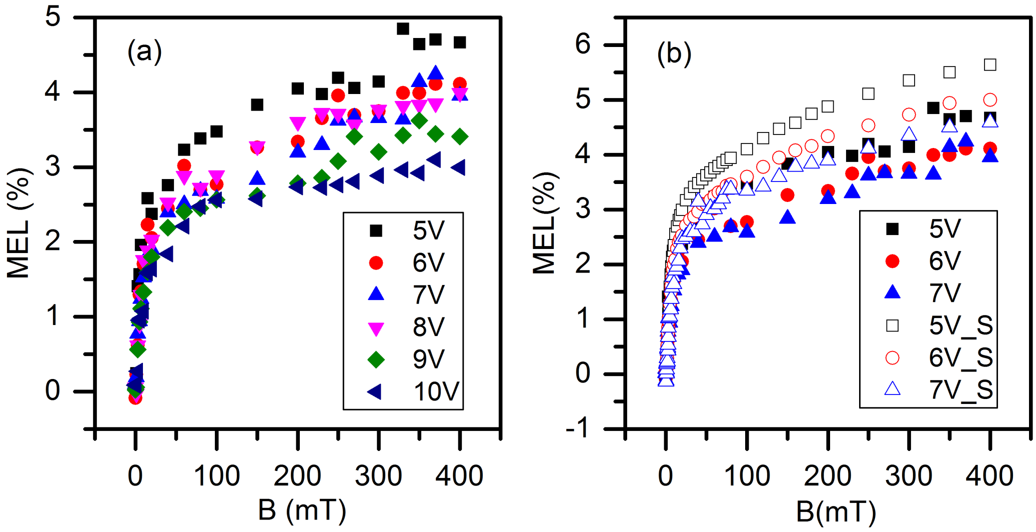

Figure 4.9: (a), The averaged MEL from transient measurements as a function of drive voltage; (b), comparison of MEL obtained from the transient method (solid symbols) and steady state method (open symbols).

4.3.5 MEL at the falling edge

This section discusses the large linear like post-pulse MEL pointed out in figure 4.6. Figure 4.10 shows the post-pulse MELs at 400 mT under different applied bias. The red lines were set to 50 μs where the EL intensity started to decrease, which also indicates the time when the pulses were turned off. Although noisy at low voltages, these post-pulse effect are clearly present at all voltages. The rise in MEL becomes clearer and more significant as the voltage increases. The magnitude of MEL at 52.5 μs is $\sim$ 20% at 9 V and $\sim$ 30% at 10 V. The blank areas of the 7 V data at around 55 μs and of the 8 V data at around 53 μs are because that the MEL values are outside the displayed range. Data at these blank areas is not real. They are positive and negative spikes caused by the transition of EL intensity from positive to negative. For more detail, see section 4.3.2, discussion of figure 4.5 (a).

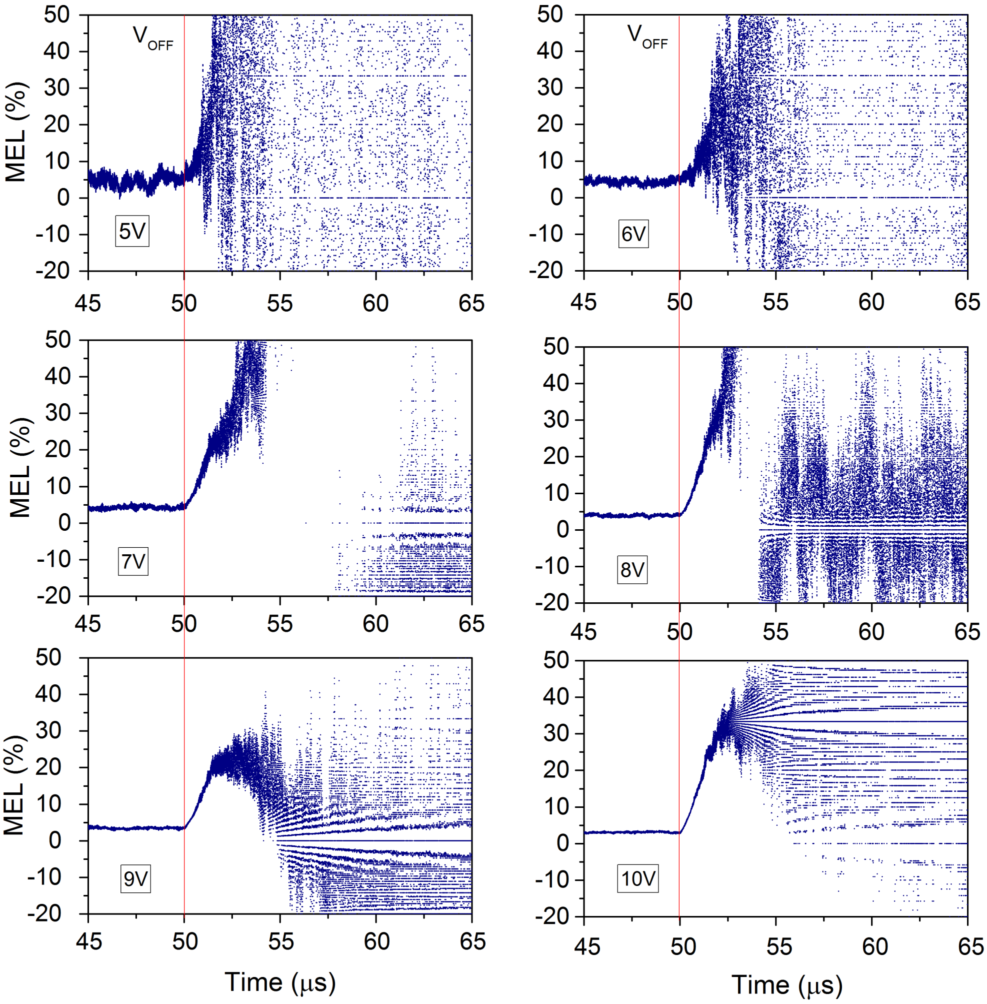

Figure 4.10: The post-pulse MELs under various applied pulses. The magnetic field applied is 400 mT and the red line indicates the off point of the pulse.

To see how the post-pulse MEL changes with the magnetic field, the post-pulse MELs measured at 10 V as and at several fields are presented in figure 4.11. The red lines indicate the time when the pulses were turned off and are set to 50 μs where the EL intensity started to decrease. Compared to the MELs before 50 μs, it can be clearly seen that the MELs after 50 μs start to increase rapidly over a time of $\sim$ 2 μs at fields around 100 mT. A further observation shows that this increase feature occurs from 20 mT and it becomes clearer and stronger as the fields increase. The MELs at lower fields maintain the value for approximately half a microsecond and then approach the noise level. It can be concluded from figure 4.11 that the post-pulse

MEL has a high field dependence (with a $\sim$ 100 mT characteristic field). A close view of the evolution of the post-pulse MEL is shown in figure 4.12. The black line is the EL measured at 0 mT. Right after the pulse is turned off, the MEL increases quasi-linearly with time, over a period of $\sim$ 3 μs, it then reaches a peak at $\sim$ 4 μs , followed by a noisy decline after that.

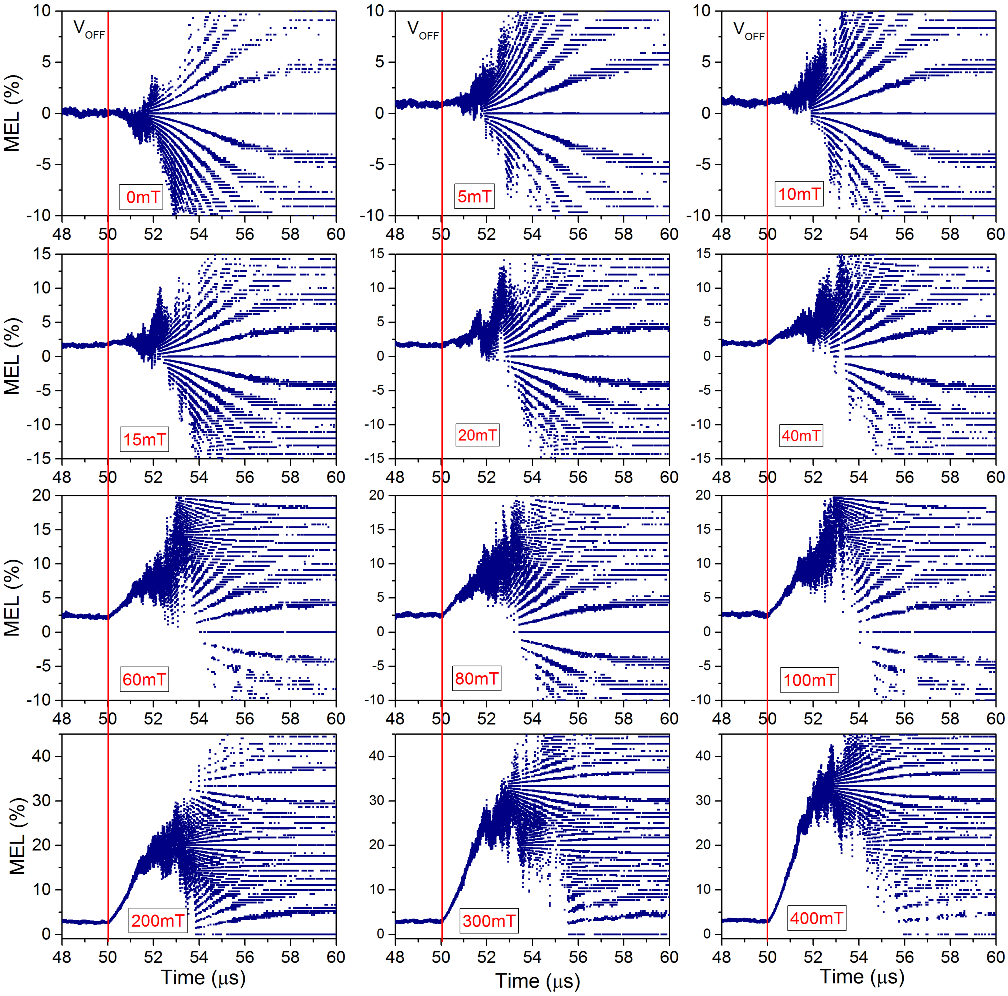

Figure 4.11: The MEL at the falling edge under different magnetic fields. The pulse applied is 10 V and the red lines indicate the time when the pulse turns off.

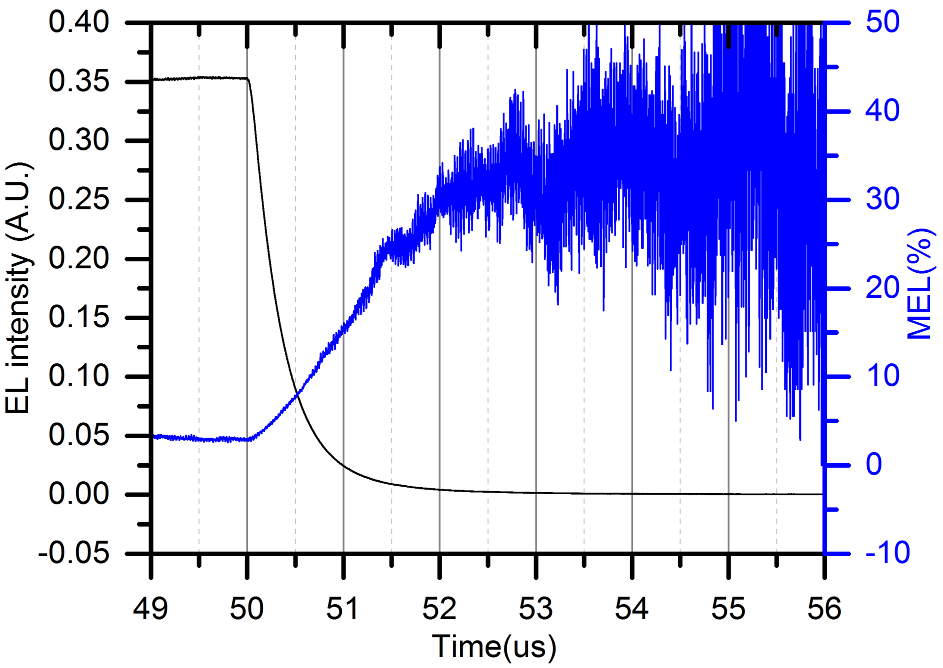

Figure 4.12: The EL at 10 V measured at 0 mT (black line) and the MEL (ΔEL/EL) at 10 V measured at 400 mT (blue line) as a function of time.

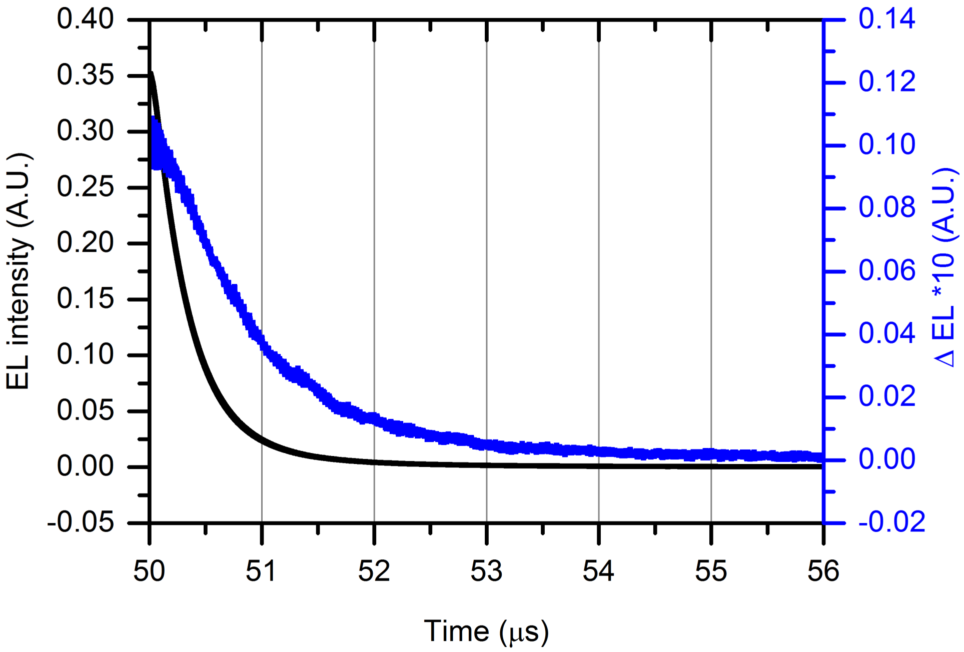

Figure 4.13: EL and ΔEL at 10 V measured at 400 mT. The ΔEL is 10 times magnified.

To understand why the MELs at large voltages show an increasing trend, the EL (black line) and ΔEL (blue line) at 10 V measured at 400 mT is presented in figure 4.13. It is worth noting that the ΔEL is magnified by a factor of 10. It can be seen that after the pulse is turned off, both of the EL and ΔEL start to decrease exponentially. The decrease of the EL, however, is much faster than that of the ΔEL, which explains why the post-pulse MEL keeps increasing even though the pulse was turned off, and a peak value can be obtained as the EL approaches zero. After that, there is not much change in the EL whereas the ΔEL keeps decaying, therefore the MEL will start to decay. This is in qualitative agreement with the 400 mT MEL shown in figure 4.12.

In order to investigate the magnetic field dependence of the post-pulse MELs quantitatively, the MEL during the first 3 μs after the turn off point were divided into 3 domains: 50 - 51 μs, 51 - 52 μs and 52 - 53 μs. The MELs of each domain are then averaged so as to represent the MFEs over this time period. As a result, MELs of each domain can be determined as a function of magnetic field. Figure 4.14 shows the averaged MEL of the three domains as a function of magnetic field.

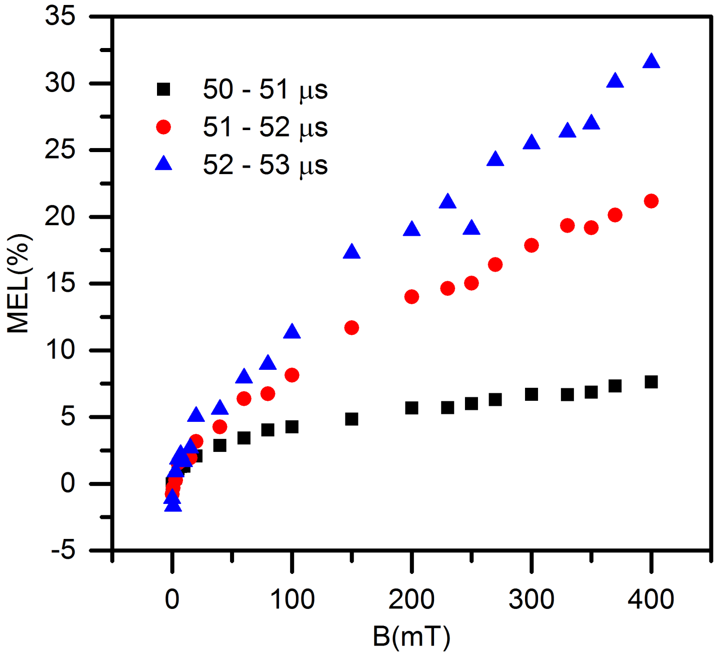

Figure 4.14: The averaged MEL of each domain as a function of magnetic field.

Unlike the averaged MEL calculated in the steady state, the post-pulse MEL shows of a very large high field component and the longer the pulse is turned off the more significant the high field component becomes.

The triple Lorenztain function, Eq. 3.4, was used to fit the averaged MEL of the three domains. The same constraints as those used in chapter 3 are applied. The fitting results are illustrated in figure 4.14. It can be seen that the triple Lorenztain function gives reasonably good fit to all the MELs. The fitting parameters are presented in table 4.2 where $a_3\%$ is the percentage ratio of a_3 to the sum of a_1, a_2, and a_3, representing the contribution of high field component. All three components increase at larger times after the pulse, and the contribution of the high field component is ~58% in domain 50 - 51 μs, ~ 77% in 51 - 52 μs and ~ 80% in 52 - 53 μs.

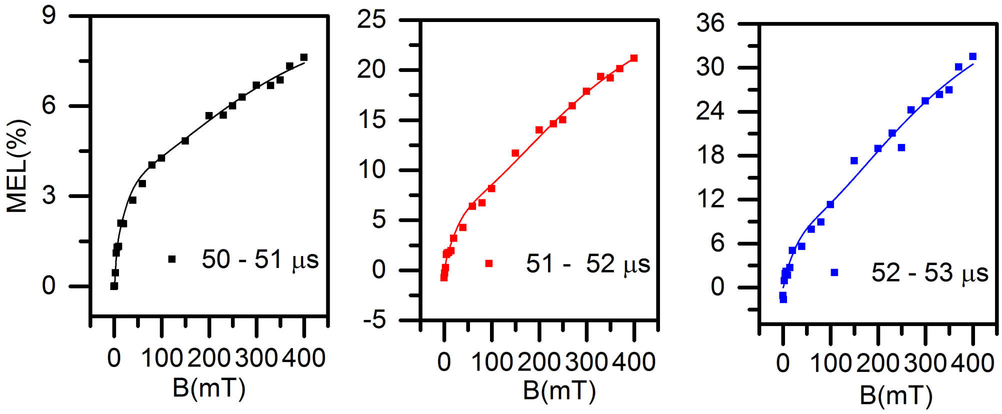

Figure 4.15: Post-pulse MEL in each time domain fitted by the triple Lorentzian function.

Domain	a_1	a_2	a_3	$a_3\%$	B_1 (mT)	B_2 (mT)	B_3 (mT)
50 - 51 μs	1.71±0.98	2.2±1.13	5.7±1.37	58.8%	4.4±3.04	30±13	252±41
51 - 52 μs	1.86±1.25	5.06±1.19	23.75±2.15	77.4%	4.4±3.04	30±13	252±41
52 - 53 μs	2.5±1.55	6.4±1.40	35.9±2.96	80.1%	4.4±3.04	30±13	252±41

Table 4.2: Triple Lorentzian fitting parameters of each domain

To investigate the underlying mechanism of the post-pulse MEL, possible spin carrying species and magnetic field dependent processes in the Alq_3 layer are discussed. At the point where the pulse was turned off, charge carrier injection stopped. In the device there would be: polaron pairs, singlets, triplets, free electrons near the cathode, accumulated holes in the TPD/Alq$_3$ interface, and possible trapped charge carriers in the bulk or near the interfaces. Processes that could potentially be perturbed by a magnetic field include spin mixing between singlets and triplets, spin mixing between polaron pairs featuring singlet and triplet configurations and exciton-charge carrier interactions. Since it is singlets that emit light in Alq$_3$, there must be singlets throughout the time period discussed (50 – 53 μs). Let's consider the singlets and polaron pairs featuring singlet configuration that exist at 50 μs as the 'primary singlets'. Since the lifetime of singlet is of the order of $\sim$10 ns, we know that the EL measured in the time scale of microseconds must come from 'secondary singlets'. These 'secondary singlets' can be formed by recombination of charges present in the bulk, charges accumulated at the interfaces, de-trapped charges and charges formed via the dissociation of excitons. It can therefore be seen that the high magnetic field effect is affecting the processes involving the formation of the 'secondary singlets'. Among those processes, the recombination of charge carriers displays a low field dependence, which indicates that the high field dependence comes from processes that generates mobile charge carriers. These point to de-trapping of trapped charge carriers and/or triplet-charge carrier interaction.

Ding et al. [60] investigated the behaviour of singlets and triplets under magnetic fields using fluorescence and phosphorescence doped Alq$_3$ systems. They constructed two devices with the stricture of ITO / NPB / Alq$_3$: PtOEP / Alq$_3$ / LiF / Al (device A) and ITO / NPB / Alq$_3$: C540 / Alq$_3$ / Alq$_3$: PtOEP / Alq$_3$ / LiF / Al (device B). Alq$_3$ acted as the host material, PtOEP acted as the phosphorescence material, emitting red light with a peak at 650 nm, and C540 acted as fluorescence material, emitting green light with a peak at 510 nm. The idea of the experiment was that since device A contained only PtOEP, both singlets and triplets in the host Alq$_3$ transferred their energy to triplets in the guest PtOEP. The MEL of device A measured at a wavelength of 650 nm contained, therefore, information about field dependent processes involving singlet and triplet. In comparison, device B contained both C540 and PtOEP. In this device, most singlets are filtered out by the C540 doped layer via red light emission before they reach the PtOEP doped layer. As a result, only triplets contributed to the emission in PtOEP. The MELs measured at wavelengths of 510 nm and 650 nm were, therefore, the fingerprints of the behaviour of singlets and triplets under magnetic field, respectively. Their results showed that the MEL of device A measured at 650 nm features a typical line-shape as the ones in figure 4.9: a rapid low field rise followed by a gradual high field increase. Comparison to device A, the MEL of device B measured at 510 nm shows only the low field process which saturates perfectly at fields greater than 40 mT, whilst the MEL measured at 650 nm shows a quasi-linear line-shape. The quasi-linear line-shape in their result is similar to the line-shape of the post-pulse MEL showed in figure 4.15. The similarity of the line-shape suggests that the large MEL obtained after the pulse was turned off is due to triplet-charge carrier interaction.

One may wonder why the magnitude of the post-pulse MELs (4.14) is almost 10 times larger than that of the “steady” state MELs (figure 4.9). To answer this question, the EL is decomposed into two parts: prompt EL (EL_P), that is, EL from the recombination of injected charge carriers, and secondary EL (EL_S), that is, EL from the recombination of charge carriers generated via triplet-charge carrier interaction. The total EL is the sum of the two. It is obvious that EL_P and EL_S are expected to be field dependent and to occur in both the on-pulse and the post-pulse stages. Let ΔEL_P and ΔEL_S denote the magnetic field induced changes in EL_P and EL_S, respectively. Assuming that the field induced change is proportional to the corresponding EL intensity, the MEL can be written as in Eq. 4.3 where K_P and K_S are pre-factors denoting the field dependent mixing rate for the emission process of EL_P and interaction rate for the emission process of EL_S, respectively.

$$MEL = \frac{(\Delta EL_P + \Delta EL_S)}{(EL_P + EL_S)} = \frac{(K_P \times EL_P + K_S \times EL_S)}{(EL_P + EL_S)} \tag{4.3}$$

At the on-pulse stage ("steady" state), both the EL_P and the EL_S contribute to the total EL and the EL_P plays a dominant role. Therefore, the contribution of the high field triplet-charge carrier interaction to the MEL is modified by a large denominator, dominated by EL_P, resulting in a smaller value of the "steady" state MEL. In comparison, the post-pulse EL comes mainly from EL_S. Assuming that the number of the secondary charge carriers generated by triplet-charge carrier interaction is highly field dependent, the post-pulse MEL can be very large, because the denominator is dominated by EL_S which is small. This interpretation is qualitatively in agreement with the fitting results in table 4.2. That is, the longer the pulse was turned off, the larger the high field strength became, because the role of EL_P became weaker and weaker as time proceeded. This does not mean that the large post-pulse MEL is a result of the small denominator, because the numerator is assumed to be proportional to the denominator.

What if the assumption that the triplet-charge carrier interaction rate K_S is highly field dependent is wrong? In this case, the large post-pulse MEL can not the deduced from Eq. 4.3. There is an alternative possibility. Chen et al. [122] found large MEL in a m-MTDATA:Alq$_3$ based charge-transfer system. The light emission mechanism of this system is via the direct recombination of holes on m-MTDATA and electrons on Alq$_3$ (charge-transfer states). It was found that the MEL of the device is larger than that of a pure Alq$_3$ device by a factor of 3. They suggested that since the electron and hole forming a charge-transfer state are sitting on different molecules, the spin exchange energy between singlets and triplets is much smaller, which results in a more efficient intersystem conversion between singlets and triplets. The MEL is, therefore, larger in the charge-transfer device. It is already known that the spin mixing process happens in both electron-hole pairs and excitons. Like the charge-transfer state case, the spin exchange energy between electron-hole pairs is expected to be smaller than that of the exciton. Consequently, the spin mixing rate in electron-hole pairs is expected to be larger than that of the excitons. In this thesis, after the pulse was turned off, the EL intensity decreased rapidly, which indicates that the charge carrier concentration was also very small; accordingly, the number of electron-hole pairs must be larger than the number of excitons; hence the MEL was dominated by the electron-hole pairs, producing a larger MEL. This assumption is valid. When the charge carrier concentration is small, the MEL is dominated by the mixing process occurring in electron-hole pairs, therefore, even if the rate of the triplet-charge carrier interaction is only slightly dependant on the high magnetic field, it can still produce the larger MEL.

To examine the real reason for the large post-pulse MEL, a set of raw data of the rising edge and falling edge is shown in figure 4.16. It can be seen from the figure that at the rising edge, it takes ∼ 0.1 μs for the EL to increase increase from ∼ 0 to 0.05 A.U., while at the falling edge, it takes ∼ 3 μs for the EL to decrease from 0.05 A.U. to ∼ 0. This is in agreement with the conclusion that the EL at the rising edge is mainly from the recombination of primary charge carriers and that at the falling edge is mainly from the recombination of secondary charge carriers. Irrespective of forming by primary or secondary charge carriers, it is expected that at the same EL intensity, the electron-hole pair concentration in the two cases (the rising and the falling edges) will be approximately the same. If the 'electron-hole pair dominating' argument is correct, we would see the same level of change in the EL after applying the 400 mT magnetic field. It is, however, seen from figure 4.16 that the field induced change of EL is much more significant at the falling edge than it is at the rising edge. It is, therefore, concluded that the 'electron-hole pair dominating' argument may be right for the voltage dependent decrease in steady

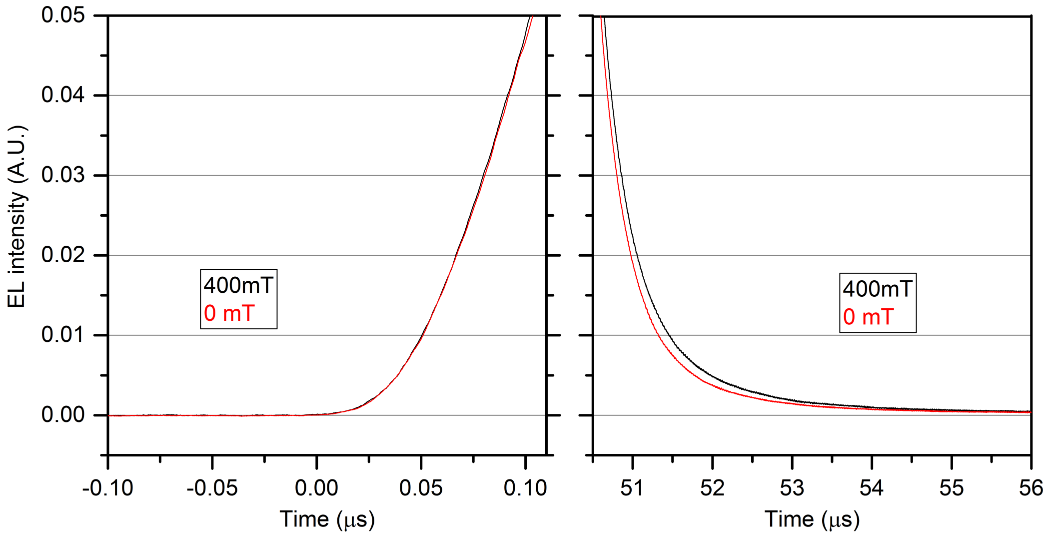

Figure 4.16: A set of raw data of the rising edge and falling edge at the same EL intensity.

state MEL, but it is not the underlying mechanism for the large post-pulse MEL. The reason for the large post-pulse MEL results is that the EL at this regime is mainly due to secondary charge carriers. Since the secondary charge carriers are generated via the high field dependent triplet-charge carrier interaction, it is also concluded that the triplet-charge carrier interaction rate is highly dependent on the magnetic field and its field dependence is much larger than that of the spin mixing processes. The results here also show that although we cannot rule out the magnetic field effect on singlet-charge carrier interaction, the MFE on triplet-charge carrier interaction is certainly far stronger than on singlet-charge carrier interaction.

4.3.6 Triplet-charge carrier interaction

Early studies on the lifetime of delayed fluorescence have shown that charge carriers, both mobile and trapped, can quench triplets [39, 98]. Helfrich et al [98] measured the triplet lifetime under different electron injection densities, they found that the triplet lifetime was greatly decreased at larger electron injection density. Wittmer et al. [39] found that trapped charge carriers can quench excited states at the same rate as that of mobile charge carrier. Kalinowski et al. [99] investigated the quenching mechanisms of excitons on charge carriers. They found that both dissociation and annihilation occurred in their phosphorescence system, depending on the strength of electric field and the electrodes of the devices. They also revealed that holes quench excitons via the annihilation route.

To fully understand how the triplet-charge carrier interaction contributes to the large post-pulse MEL, the results of the interaction on the intensity of charge carriers need to be discussed. There are three possible routes through which charge carriers interact with triplets: scattering, dissociation and annihilation. It is obvious that the scattering process makes no change to both the charge carrier and the triplet concentration, and this process is not magnetic field dependent [20], therefore, the scattering process makes no change to the MEL. The dissociation process breaks down the triplets and generates a pair of mobile charge carriers as well as the original carrier, which increases the number of secondary charge carriers, therefore, contributing to the positive MEL. The annihilation process quenches the triplets without generating charge carrier pairs and leaves the original charge carrier, which decreases the number of triplets, therefore contributes to the negative MEL indirectly via weakening of the dissociation channel.

The results of chapter 3 have suggested that triplet-hole interaction is responsible for the negative high field MELs found in those hole dominated devices, and triplet-electron interaction is tentatively responsible for the positive high field MELs in the standard device. The electron-triplet interaction must be via the dissociation route and the triplet-hole interaction must be via the annihilation route. To be more specific, annihilation and dissociation processes coexist in the device both with and without magnetic field. The dissociation process increases the EL intensity by generating secondary charge carriers, and the annihilation process decreases the EL intensity by weakening the dissociation channel. When applying a magnetic field, especially at high fields, both the dissociation rate and the annihilation rate increase. As a result, in triplet-hole interaction dominated devices the secondary EL channel is weakened, causing a negative high field MEL decay as discussed in chapter 3. On the contrary, in triplet-electron dominated devices the secondary EL channel is enhanced, generating the positive high field MEL. In other words, the triplet-charge carrier interaction which contributes to the EL after the pulse was turned off is through the dissociation of triplets by electrons. It also suggests that the small MEL rise over a time range of ~ 5 μs at the rising edge is due to the triplet-electron interaction.

4.4 Conclusion of this chapter

In this chapter, the transient MFE on standard devices were investigated. It has found that there are three types of behaviour present in the MEL depending on the time regimes and the measurement conditions. A small increase process is found in the beginning of the pulse over a time range of ~ 5 μs under fields higher than 20 mT and voltages larger than 6 V. Its high field and larger voltage dependence along with the time period it lasts, indicate that it is due to triplet-charge carrier interaction. At this stage, it is not clear what type of charge carrier is involved and which interaction route is occurring. A "steady" state MEL is found at the body of the pulse. The comparison of its averaged value as a function of magnetic field and the steady state MEL obtained from the standard device studied in chapter 3 shows that the MEL of this regime shares the same line-shape and mechanisms as those measured by steady state MFE measurements. A large MEL rise is found at the falling edge of the pulse and it is named as post-pulse MEL. The investigation of the origin of EL at this regime reveals that it is dominated by 'secondary singlets' that formed by charge carriers generated by triplet-charge carrier interaction. The discussion of possible ways that could lead to large MEL indicates that triplet-charge carrier interaction rate is the only mechanism which is suitable for the large post-pulse MEL. The comparison of ELs with and without magnetic field at the rising edge and the falling edge shows a much stronger effect at the falling edge. Although we cannot rule out the existence singlet-charge carrier interaction, its field dependence certainly is much weaker than that of triplet-charge carrier interaction. Additionally, the dependence of triplet-charge carrier interaction on magnetic field must be stronger than that of the spin mixing between singlets and triplets. From the discussion of the results of possible triplet-charge carrier interactions, it is suggested that the triplet-hole interaction contributes to the negative high field MEL via the annihilation route whereas the triplet-electron interaction contributes to the positive high field MEL via the dissociation route. The slow rise in MEL at high fields at the beginning of the pulse and the subtle high field component in the "steady" state MEL can now be explained by the magnetic field enhanced triplet dissociation rate via interacting with electrons.

Chapter 5

Conclusion

This thesis has presented the results of two major studies on the MFEs in Alq_3 based OLEDS, focusing on the high field regime. In the first study, OLEDs with different structures were constructed to vary the hole/electron balance, so as to investigate the effect of excitons on high field MFE. It is found that the hole-exciton interaction could lead to a high field decay in MEL, even that room temperature. The second study was then designed to distinguish the roles played by singlet and triplet excitons.

By varying the hole/electron injection balance, it is observed that a negative high field component emerges gradually as the hole to electron ratio increases, which suggests that there are at least two high field processes present, contributing to positive and negative MEL, separately. The fact that significant high field MEL decay is obtained at room temperature in an extremely inefficient and severely hole dominated device points to two conclusions: first, the high field decay of the MEL cannot be due to the widely used triplet-triplet annihilation, at least not in Alq_3 based devices, second, this high field decay must be related to holes. This points to a possible process for explaining the high field MFE being the triplet-charge carrier interaction. It can then be concluded that hole-triplet interaction is responsible for the high field MEL decay. More generally, a hole-exciton interaction is responsible for the high field MEL decay since there is no direct evidence to exclude the hole-singlet interaction. A positive high field MEL can be tentatively attributed to electron-exciton interaction.

Although triplet-charge carrier interaction is widely used to explain MFE in the scientific community, because triplet concentration is expected to be thousands times larger than singlet concentration, there is no direct evidence for excluding the role of singlets. Transient MEL can be conducted to distinguish the role of the two and obtain insight into the interaction process. Additional MEL features are found both at the rising edge and falling edge of a pulse. Small MEL increases are found at the rising edge over a time scale of ~ 5 μs and larger MEL increases are observed at the falling edge over a scale of ~ 6 μs. Both of them show high field dependence and are seen to be stronger at large drive voltage, which suggests that they are due to triplet related processes. This points to the triplet-charge carrier interaction because the triplet-triplet annihilation has been excluded in chapter 3. It also suggests that the dependence of triplet-charge carrier interaction rate on magnetic fields is much stronger compared to that of the spin mixing rate. This conclusion is again confirmed by the comparison of EL with and without magnetic field at the rising edge and the falling edge. At the rising edge it is the spin mixing process dominates and no visible EL increase occurs whereas at the falling edge it is the triplet-charge carrier interaction process dominates and the EL shows a clear increase. The discussion of the results from the three possible triplet-charge carrier interaction routes suggested that triplet-hole interaction contributes to the negative high field MEL via the annihilation route whereas the triplet-electron interaction contributes to the positive high field MEL via the dissociation route.

Chapter 6

Future work

In chapter 3, negative MEL is found to originate from hole-exciton interaction. The transient MEL study in chapter 4 suggests that hole-exciton interaction contributes to negative MEL via quenching the triplets. It would be useful to conduct transient MEL on some hole dominated devices to check if negative MEL occurs at the rising edge and falling edge. The challenges here are that moderately hole dominated devices may generate small signals which are likely to be overshadowed by noise, while significantly hole dominating devices show extremely small EL signals which are hard to detect.

The effect of electrical conditioning on MFE have been briefly studied in chapter 3. As found in the literature, electrical conditioning causes significant enhancement in MFE. It was suggested that the stressing process is likely to generate defects in devices, which decrease the current and EL but increase the magnetic field effects. It seems to imply that defects, such as structural disorder, material degradation or traps play important roles in generating large MFE response. Systematical study of the morphology and mobility of stressed devices may help reveal the mystery of the MFE.

Bibliography

[1] C. W. Tang, S. A. VanSlyke, "Organic electroluminescent diodes", *Applied Physics Letters* **1987**, *51*, 913.

[2] B. Geffroy, P. le Roy, C. Prat, "Organic light-emitting diode (OLED) technology: Materials, devices and display technologies", *Polymer International* **2006**, *55*, 572–582.

[3] S. Reineke, F. Lindner, G. Schwartz, N. Seidler, K. Walzer, B. Lüssem, K. Leo, "White organic light-emitting diodes with fluorescent tube efficiency.", *Nature* **2009**, *459*, 234–8.

[4] C. W. Tang, "Two-layer organic photovoltaic cell", *Applied Physics Letters* **1986**, *48*, 183–185.

[5] C. Waldauf, P. Schilinsky, J. Hauch, C. J. Brabec, "Material and device concepts for organic photovoltaics: towards competitive efficiencies", *Thin Solid Films* **Mar. 2004**, *451-452*, 503–507.

[6] H. Klauk, M. Halik, U. Zschieschang, G. Schmid, W. Radlik, W. Weber, "High-mobility polymer gate dielectric pentacene thin film transistors", *Journal of Applied Physics* **2002**, *92*, 5259.

[7] M. Shtein, J. Mapel, J. B. Benziger, S. R. Forrest, "Effects of film morphology and gate dielectric surface preparation on the electrical characteristics of organic-vapor-phase-deposited pentacene thin-film transistors", *Applied Physics Letters* **2002**, *81*, 268.

[8] T. Sakanoue, H. Sirringhaus, "Band-like temperature dependence of mobility in a solution-processed organic semiconductor.", *Nature materials* **2010**, *9*, 736–40.

[9] K. Tsung, S. So, "High temperature carrier mobility as an intrinsic transport parameter of an organic semiconductor", *Organic Electronics* **July 2009**, *10*, 661–665.

[10] M. Pope, S. Charles, *Electronic Processes in Organic Crystalsand Polymers*, Oxford Science Publications, **1999**, pp. 337–343.

[11] D. Hertel, H. Bässler, “Photoconduction in amorphous organic solids”, *ChemPhysChem* **2008**, *9*, 666–688.

[12] M. Pope, H. P. Kallmann, P. Magnante, “Electroluminescence in Organic Crystals”, *The Journal of Chemical Physics* **1963**, *38*, 2042.

[13] T. Mori, K. Obata, K. Miyachi, T. Mizutani, Y. Kawakami, “Fluorescence Lifetime of Organic Thin Films Alternately Deposited with Diamine Derivative and Aluminum Quinoline”, *Japanese Journal of Applied Physics* **1997**, *36*, 7239.

[14] M. A. Baldo, S. R. Forrest, “Transient analysis of organic electrophosphorescence: I. Transient analysis of triplet energy transfer”, *Phys. Rev. B* **Oct. 2000**, *62*, 10958–10966.

[15] W. J. Finkenzeller, M. E. Thompson, H. Yersin, “Phosphorescence dynamics and spin-lattice relaxation of the {OLED} emitter Ir(btp)2(acac)”, *Chemical Physics Letters* **2007**, *444*, 273–279.

[16] S. I. Yoo, J. A. Yoon, N. H. Kim, J. W. Kim, J. S. Kang, C.-B. Moon, W. Y. Kim, “Improvement of efficiency roll-off in blue phosphorescence {OLED} using double dopants emissive layer”, *Journal of Luminescence* **2015**, *160*, 346–350.

[17] A. Brown, K. Pichler, N. Greenham, D. Bradley, R. Friend, A. Holmes, “Optical spectroscopy of triplet excitons and charged excitations in poly(p-phenylenevinylene) light-emitting diodes”, *Chemical Physics Letters* **1993**, *210*, 61–66.

[18] M. a. Baldo, D. F. O’Brien, M. E. Thompson, S. R. Forrest, “Excitonic singlet-triplet ratio in a semiconducting organic thin film”, *Physical Review B* **Nov. 1999**, *60*, 14422–14428.

[19] J. Kalinowski, M. Cocchi, D. Virgili, P. Di Marco, V. Fattori, “Magnetic field effects on emission and current in Alq3-based electroluminescent diodes”, *Chemical Physics Letters* **Oct. 2003**, *380*, 710–715.

[20] R. C. Johnson, R. E. Merrifield, P. Avakian, R. B. Flippen, “Effects of Magnetic Fields on the Mutual Annihilation of Triplet Excitons in Molecular Crystals”, *Physical Review Letters* **Aug. 1967**, *19*, 285–287.

[21] R. E. Merrifield, “Theory of Magnetic Field Effects on the Mutual Annihilation of Triplet Excitons”, *The Journal of Chemical Physics* **1968**, *48*, 4318.

[22] W. Wagemans, P. Janssen, A. Schellekens, F. Bloom, P. Bobbert, B.Koopmans, “the many faces of organic magnetoresistance”, *SPIN* **2011**, *1*.

[23] H. Gu, X. Zhang, H. Wei, Y. Huang, S. Wei, Z. Guo, "An overview of the magnetoresistance phenomenon in molecular systems", *Chem. Soc. Rev.* **2013**, *42*, 5907–5943.

[24] M. Cox, E. H. M. van der Heijden, P. Janssen, B. Koopmans, "Investigating the influence of traps on organic magnetoresistance by molecular doping", *Physical Review B* **Feb. 2014**, *89*, 085201.

[25] M. Wohlgenannt, P. a. Bobbert, B. Koopmans, "Intrinsic magnetic field effects in organic semiconductors", *MRS Bulletin* **July 2014**, *39*, 590–595.

[26] H. Gu, S. Chang, D. Holford, T. Zhang, H. Lu, T. Kreouzis, W. P. Gillin, "Annealing and doping-dependent magnetoresistance in single layer poly(3-hexyl-thiophene) organic semiconductor device", *Organic Electronics* **2015**, *17*, 51–56.

[27] H. Gu, S. Chang, H. Lu, D. F. Holford, T. Zhang, J. Hu, W. P. Gillin, T. Kreouzis, "Impurity effects on charge transport and magnetoconductance in a single layer poly(3-hexyl-thiophene) device", *Applied Physics Letters* **2016**, *108*.

[28] P. Desai, P. Shakya, T. Kreouzis, W. P. Gillin, "The role of magnetic fields on the transport and efficiency of aluminum tris(8-hydroxyquinoline) based organic light emitting diodes", *Journal of Applied Physics* **2007**, *102*.

[29] P. Desai, P. Shakya, T. Kreouzis, W. P. Gillin, N. A. Morley, M. R. J. Gibbs, "Magnetoresistance and efficiency measurements of Alq_3-based OLEDs", *Physical Review B* **Mar. 2007**, *75*, 094423.

[30] W. Gillin, S. Zhang, N. Rolfe, P. Desai, P. Shakya, a. Drew, T. Kreouzis, "Determining the influence of excited states on current transport in organic light emitting diodes using magnetic field perturbation", *Physical Review B* **2010**, *82*, 1–6.

[31] Ö. Mermer, G. Veeraraghavan, T. L. Francis, Y. Sheng, D. T. Nguyen, M. Wohlgenannt, a. Köhler, M. K. Al-Suti, M. S. Khan, "Large magnetoresistance in nonmagnetic π-conjugated semiconductor thin film devices", *Physical Review B - Condensed Matter and Materials Physics* **2005**, *72*, 1–12.

[32] P. a. Bobbert, T. D. Nguyen, F. W. A. van Oost, B. Koopmans, M. Wohlgenannt, "Bipolaron Mechanism for Organic Magnetoresistance", *Physical Review Letters* **Nov. 2007**, *99*, 216801.

[33] W. Wagemans, F. L. Bloom, P. a. Bobbert, M. Wohlgenannt, B. Koopmans, “A two-site bipolaron model for organic magnetoresistance”, *Journal of Applied Physics* **2008**, *103*.

[34] B. Hu, Y. Wu, “Tuning magnetoresistance between positive and negative values in organic semiconductors”, *Nature Materials* **Dec. 2007**, *6*, 985–991.

[35] U. Niedermeier, M. Vieth, R. Pätzold, W. Sarfert, H. Von Seggern, “Enhancement of organic magnetoresistance by electrical conditioning”, *Applied Physics Letters* **2008**, *92*, 37–40.

[36] S. a. Bagnich, U. Niedermeier, C. Melzer, W. Sarfert, H. von Seggern, “Origin of magnetic field effect enhancement by electrical stress in organic light emitting diodes”, *Journal of Applied Physics* **2009**, *105*, 123706.

[37] V. Ern, R. E. Merrifield, “Magnetic Field Effect on Triplet Exciton Quenching in Organic Crystals”, **1968**, *21*, 609–611.

[38] P. A. R. P. Groff, A. Suna, R. E. Merrifield, “Magnetic hyperfine modulation of dye-sensitized delayed fluorescence in organic crystals”, *Physical Review Letter* **1972**, *29*, 2655.

[39] M. Wittmer, I. Zschokke-Gränacher, “Exciton–charge carrier interactions in the electroluminescence of crystalline anthracene”, *The Journal of Chemical Physics* **1975**, *63*, 4187.

[40] S. Zhang, M. Willis, R. Gotto, K. a. Roy, N. J. Rolfe, T. Kreouzis, W. P. Gillin, “Understanding the role of electron and hole trions on current transport in aluminium tris(8-hydroxyquinoline) using organic magnetoresistance”, *Applied Physics Letters* **2014**, *104*, 043307.

[41] Y. Wu, B. Hu, “Metal electrode effects on spin-orbital coupling and magnetoresistance in organic semiconductor devices”, *Applied Physics Letters* **2006**, *89*, 203510.

[42] P. S. Tuladhar, unpublished thesis, PhD thesis, Queen Mary University of London, **2008**.

[43] Y. Lei, Y. Zhang, R. Liu, P. Chen, Q. Song, Z. Xiong, “Driving current and temperature dependent magnetic-field modulated electroluminescence in Alq_3-based organic light emitting diode”, *Organic Electronics* **2009**, *10*, 889–894.

[44] R. Liu, Y. Zhang, Y. L. Lei, P. Chen, Z. H. Xiong, “Magnetic field dependent triplet-triplet annihilation in Alq3-based organic light emitting diodes at different temperatures”, *Journal of Applied Physics* **2009**, *105*.

[45] Y. Zhang, R. Liu, Y. L. Lei, Z. H. Xiong, “Low temperature magnetic field effects in Alq[sub 3]-based organic light emitting diodes”, *Applied Physics Letters* **2009**, *94*, 083307.

[46] S. Zhang, T. Kreouzis, W. Gillin, “Low temperature magnetic field effects on the efficiency of aluminium tris(8-hydroxyquinoline) based organic light emitting diodes in the absence of magnetoresistance”, *Synthetic Metals* **June 2013**, *173*, 46–50.

[47] P. Janssen, S. H. W. Wouters, M. Cox, B. Koopmans, “Unraveling the temperature and voltage dependence of magnetic field effects in organic semiconductors”, *Journal of Applied Physics* **2013**, *114*, 174909.

[48] Y. Zhang, Q. Zhang, Y. Lei, Z. Xiong, “Magnetoconductance response due to the triplet exciton–charge interaction in organic light-emitting diodes”, *Organic Electronics* **2013**, *14*, 2505–2509.

[49] P. Chen, Y. L. Lei, Q. L. Song, Y. Zhang, R. Liu, Q. M. Zhang, Z. H. Xiong, “Magnetoelectroluminescence in tris (8-hydroxyquinolato) aluminum-based organic light-emitting diodes doped with fluorescent dyes”, *Applied Physics Letters* **2009**, *95*, 16–19.

[50] Y. Luo, H. Aziz, “Correlation Between Triplet-Triplet Annihilation and Electroluminescence Efficiency in Doped Fluorescent Organic Light-Emitting Devices”, *Advanced Functional Materials* **Apr. 2010**, *20*, 1285–1293.

[51] Q. Peng, N. Gao, W. Li, P. Chen, F. Li, Y. Ma, “Investigation of energy transfer and charge trapping in dye-doped organic light-emitting diodes by magneto-electroluminescence measurement”, *Applied Physics Letters* **2013**, *102*, 193304.

[52] S. van Reenen, S. P. Kersten, S. H. W. Wouters, M. Cox, P. Janssen, B. Koopmans, P. a. Bobbert, M. Kemerink, “Large magnetic field effects in electrochemically doped organic light-emitting diodes”, *Physical Review B* **Sept. 2013**, *88*, 125203.

[53] Y. Wu, Z. Xu, B. Hu, J. Howe, “Tuning magnetoresistance and magnetic-field-dependent electroluminescence through mixing a strong-spin-orbital-coupling molecule and a weak-spin-orbital-coupling polymer”, *Physical Review B* **Jan. 2007**, *75*, 035214.

[54] L. Yan, M. Shao, C. F. O. Graeff, I. Hummelgen, D. Ma, B. Hu, "Changing intermolecular spin-orbital coupling for generating magnetic field effects in phosphorescent organic semiconductors", *Applied Physics Letters* **2012**, *100*, 013301.

[55] Y. Sheng, T. D. Nguyen, G. Veeraraghavan, Ö. Mermer, M. Wohlgenannt, "Effect of spin-orbit coupling on magnetoresistance in organic semiconductors", *Physical Review B - Condensed Matter and Materials Physics* **2007**, *75*, 1–6.

[56] F. L. Bloom, W. Wagemans, M. Kemerink, B. Koopmans, "Correspondence of the sign change in organic magnetoresistance with the onset of bipolar charge transport", *Applied Physics Letters* **2008**, *93*, 263302.

[57] L. Yan, Y. Wu, Z. Xu, B. Hu, "Positive and negative magnetic field effects in organic semiconducting materials", *Synthetic Metals* **Nov. 2009**, *159*, 2323–2325.

[58] H. Kang, I.-J. Lee, C. Sup Yoon, "Sign change in the organic magnetoresistance of tris(8-hydroxyquinolinato)aluminum upon annealing", *Applied Physics Letters* **2012**, *100*, 073302.

[59] H. Gu, T. Kreouzis, W. P. Gillin, "The transition from bipolaron to triplet-polaron magnetoresistance in a single layer organic semiconductor device", *Organic Electronics* **2014**, *15*, 1711–1716.

[60] B. Ding, K. Alameh, "Simultaneous monitoring of singlet and triplet exciton variations in solid organic semiconductors driven by an external static magnetic field", *Applied Physics Letters* **2014**, *105*, 013304.

[61] W. Jia, Q. Zhang, L. Chen, Y. Ling, H. Liu, C. Lu, P. Chen, Z. Xiong, "Spin–orbital coupling induced high-field decay of magneto-electroluminescence in pristine Alq_3-based organic light-emitting diodes", *Organic Electronics* **July 2015**, *22*, 210–215.

[62] S. Zhang, T. Kreouzis, W. Gillin, "Low temperature magnetic field effects on the efficiency of aluminium tris(8-hydroxyquinoline) based organic light emitting diodes in the absence of magnetoresistance", *Synthetic Metals* **2013**, *173*, 46–50.

[63] J. Rybicki, R. Lin, F. Wang, M. Wohlgenannt, C. He, T. Sanders, Y. Suzuki, "Tuning the Performance of Organic Spintronic Devices Using X-Ray Generated Traps", *Physical Review Letters* **Aug. 2012**, *109*, 076603.

[64] V. Prigodin, J. Bergeson, D. Lincoln, A. Epstein, “Anomalous room temperature magnetoresistance in organic semiconductors”, *Synthetic Metals* **May 2006**, *156*, 757–761.

[65] B. Hu, Y. Wu, Z. Zhang, S. Dai, J. Shen, “Effects of ferromagnetic nanowires on singlet and triplet exciton fractions in fluorescent and phosphorescent organic semiconductors”, *Applied Physics Letters* **2006**, *88*.

[66] Y. Wu, B. Hu, J. Howe, A.-P. Li, J. Shen, “Spin injection from ferromagnetic Co nanoclusters into organic semiconducting polymers”, *Phys. Rev. B* **Feb. 2007**, *75*, 075413.

[67] P. Chen, M. Li, Q. Peng, F. Li, Y. Liu, Q. Zhang, Y. Zhang, Z. Xiong, “Direct evidence for the electron–hole pair mechanism by studying the organic magneto-electroluminescence based on charge-transfer states”, *Organic Electronics* **Oct. 2012**, *13*, 1774–1778.

[68] S. Zhang, J. Song, T. Kreouzis, W. P. Gillin, “Measurement of the intersystem crossing rate in aluminum tris(8-hydroxyquinoline) and its modulation by an applied magnetic field”, *Journal of Applied Physics* **2009**, *106*, 043511.

[69] J. Kalinowski, J. Szmytkowski, W. Stampor, “Magnetic hyperfine modulation of charge photogeneration in solid films of Alq3”, *Chemical Physics Letters* **2003**, *378*, 380–387.

[70] M. Wohlgenannt, Z. V. Vardeny, “Spin-dependent exciton formation rates in -conjugated materials”, *Journal of Physics: Condensed Matter* **2003**, *15*, R83.

[71] C. Gärditz, A. G. Mückl, M. Cölle, “Influence of an external magnetic field on the singlet and triplet emissions of tris-(8-hydroxyquinoline)aluminum(III) (Alq3)”, *Journal of Applied Physics* **2005**, *98*.

[72] V. Ern, R. E. Merrifield, “Magnetic Field Effect on Triplet Exciton Quenching in Organic Crystals - L. S. Swanson et. al..pdf”, **1968**, *21*, 609–611.

[73] J. Y. Song, N. Stingelin, W. P. Gillin, T. Kreouzis, “Reduced hole mobility due to the presence of excited states in poly-(3-hexylthiophene)”, *Applied Physics Letters* **2008**, *93*, 1–4.

[74] J. Y. Song, N. Stingelin, a. J. Drew, T. Kreouzis, W. P. Gillin, “Effect of excited states and applied magnetic fields on the measured hole mobility in an organic semiconductor”, *Physical Review B - Condensed Matter and Materials Physics* **2010**, *82*, 1–5.

[75] F. Li, L. Xin, S. Liu, B. Hu, "Direct measurement of the magnetic field effects on carrier mobilities and recombination in tri-(8-hydroxyquinoline)-aluminum based light-emitting diodes", *Applied Physics Letters* **2010**, *97*, 073301.

[76] P. Desai, P. Shakya, T. Kreouzis, W. P. Gillin, "The role of magnetic fields on the transport and efficiency of aluminum tris(8-hydroxyquinoline) based organic light emitting diodes", *Journal of Applied Physics* **2007**, *102*.

[77] R. N. Mahato, H. Lulf, M. H. Siekman, S. P. Kersten, P. A. Bobbert, M. P. de Jong, L. De Cola, W. G. van der Wiel, "Ultrahigh Magnetoresistance at Room Temperature in Molecular Wires", *Science* **July 2013**, *341*, 257–260.

[78] S. P. Kersten, S. C. J. Meskers, P. a. Bobbert, "Route towards huge magnetoresistance in doped polymers", *Physical Review B* **July 2012**, *86*, 045210.

[79] J. Kalinowski, J. Szmytkowski, W. Stampor, "Magnetic hyperfine modulation of charge photogeneration in solid films of Alq3", *Chemical Physics Letters* **2003**, *378*, 380–387.

[80] Y. Sheng, T. D. Nguyen, G. Veeraraghavan, Ö. Mermer, M. Wohlgenannt, S. Qiu, U. Scherf, "Hyperfine interaction and magnetoresistance in organic semiconductors", *Physical Review B* **July 2006**, *74*, 045213.

[81] Y. Wu, Z. Xu, B. Hu, J. Howe, "Tuning magnetoresistance and magnetic-field-dependent electroluminescence through mixing a strong-spin-orbital-coupling molecule and a weak-spin-orbital-coupling polymer", *Physical Review B - Condensed Matter and Materials Physics* **2007**, *75*, 1–6.

[82] L. Yan, M. Shao, C. F. O. Graeff, I. Hummelgen, D. Ma, B. Hu, "Changing intermolecular spin-orbital coupling for generating magnetic field effects in phosphorescent organic semiconductors", *Applied Physics Letters* **2012**, *100*, 1–4.

[83] N. Rolfe, M. Heeney, P. Wyatt, A. Drew, T. Kreouzis, W. Gillin, *Synthetic Metals* **Apr. 2011**, *161*, 608–612.

[84] S. Majumdar, H. S. Majumdar, H. Aarnio, D. Vanderzande, R. Laiho, R. Österbacka, "Role of electron-hole pair formation in organic magnetoresistance", *Physical Review B - Condensed Matter and Materials Physics* **2009**, *79*, 1–4.

[85] W. J. Baker, D. R. McCamey, K. J. Van Schooten, J. M. Lupton, C. Boehme, "Differentiation between polaron-pair and triplet-exciton polaron spin-dependent

mechanisms in organic light-emitting diodes by coherent spin beating", *Physical Review B - Condensed Matter and Materials Physics* **2011**, *84*, 1–7.

[86] W. Qin, K. Gao, S. Yin, S. J. Xie, "Investigating the magnetic field effect on electron-hole pair in organic semiconductor devices", *Journal of Applied Physics* **2013**, *113*.

[87] M. Wittmer, I. Zschokke-Gränacher, "Exciton–charge carrier interactions in the electroluminescence of crystalline anthracene", *The Journal of Chemical Physics* **1975**, 4187.

[88] Y. Zhang, R. Liu, Y. L. Lei, Z. H. Xiong, "Low temperature magnetic field effects in Alq3-based organic light emitting diodes", *Applied Physics Letters* **2009**, *94*.

[89] M. Cölle, C. Gärditz, a. G. Mückl, "Phosphorescence and electrophosphorescence in thin films of tris-(8-hydoxyquinoline)aluminum(III) (Alq3)", *Synthetic Metals* **2004**, *147*, 97–100.

[90] Q. Peng, P. Chen, F. Li, "The charge-trapping and triplet-triplet annihilation processes in organic light-emitting diodes: A duty cycle dependence study on magneto-electroluminescence", *Applied Physics Letters* **2013**, 023301.

[91] P. Shakya, P. Desai, M. Somerton, G. Gannaway, T. Kreouzis, W. P. Gillin, "The magnetic field effect on the transport and efficiency of group III tris(8-hydroxyquinoline) organic light emitting diodes", *Journal of Applied Physics* **2008**, *103*.

[92] K. Sugiyama, H. Ishii, Y. Ouchi, K. Seki, "Dependence of indium–tin–oxide work function on surface cleaning method as studied by ultraviolet and x-ray photoemission spectroscopies", *Journal of Applied Physics* **2000**, *87*, 295.

[93] H. Kanaan, P. Jolinat, G. Ablart, P. Destruel, C. Renaud, C. Wen Lee, T. P. Nguyen, "Influence of poly (3,4-ethylenedioxythiophene)-poly (styrenesulfonate) in polyfluorene-based light-emitting diodes: Evidence of charge trapping at the organic interface", *Organic Electronics: physics materials applications* **2010**, *11*, 1047–1052.

[94] H. Zhang, P. Desai, Y. Q. Zhan, A. J. Drew, W. P. Gillin, T. Kreouzis, "The importance of holes in aluminium tris-8-hydroxyquinoline (Alq3) devices with Fe and NiFe contacts", *Applied Physics Letters* **2014**, *104*.

[95] H. Bässler, "Charge Transport in Disordered Organic Photoconductors a Monte Carlo Simulation Study", *physica status solidi (b)* **1993**, *175*, 15–56.

[96] P. E. Burrows, V. Bulovic, S. R. Forrest, L. S. Sapochak, D. M. McCarty, M. E. Thompson, "Reliability and degradation of organic light emitting devices", *Applied Physics Letters* **1994**, *65*, 2922.

[97] H. Aziz, "Degradation Mechanism of Small Molecule-Based Organic Light-Emitting Devices", *Science* **Mar. 1999**, *283*, 1900–1902.

[98] W. Helfrich, "Destruction of triplet excitons in anthracene by injected electrons", *Physical Review Letters* **1966**, *16*, 401–403.

[99] J. Kalinowski, W. Stampor, J. Szmytkowski, D. Virgili, M. Cocchi, V. Fattori, C. Sabatini, "Coexistence of dissociation and annihilation of excitons on charge carriers in organic phosphorescent emitters", *Physical Review B - Condensed Matter and Materials Physics* **2006**, *74*, 1–11.

[100] W. Humbs, H. Zhang, M. Glasbeek, "Femtosecond fluorescence upconversion spectroscopy of vapor-deposited tris(8-hydroxyquinoline) aluminum films", *Chemical Physics* **2000**, *254*, 319–327.

[101] Y. Kawasumi, I. Akai, T. Karasawa, "Photoluminescence and dynamics of excitons in Alq_3 single crystals", *International Journal of Modern Physics B* **2001**, *15*, 3825–3828.

[102] P. W. M. Blom, M. J. M. de Jong, M. G. van Munster, "Electric-field and temperature dependence of the hole mobility in poly(p-phenylene vinylene)", *Phys. Rev. B* **Jan. 1997**, *55*, R656–R659.

[103] L. B. Schein, A. Peled, D. Glatz, "The electric field dependence of the mobility in molecularly doped polymers", *Journal of Applied Physics* **1989**, *66*, 686–692.

[104] R. G. Kepler, P. M. Beeson, S. J. Jacobs, R. A. Anderson, M. B. Sinclair, V. S. Valencia, P. A. Cahill, "Electron and hole mobility in tris(8hydroxyquinolinolatoN1,O8) aluminum", *Applied Physics Letters* **1995**, *66*, 3618–3620.

[105] A. G. M*ü*ckl, S. Berleb, W. Br*ü*tting, M. Schwoerer, "Transient electroluminescence measurements on organic heterolayer light emitting diodes", *Synthetic Metals* **2000**, *111–112*, 91–94.

[106] A. J. Pal, R. Österbacka, K.-M. K*ä*llman, H. Stubb, "Transient electroluminescence: Mobility and response time in quinquethiophene Langmuir–Blodgett films", *Applied Physics Letters* **1997**, *71*, 228–230.

[107] J. Wang, R. G. Sun, G. Yu, A. J. Heeger, "Fast pulsed electroluminescence from polymer light-emitting diodes", *Journal of Applied Physics* **2002**, *91*, 2417–2422.

[108] H. Park, D.-S. Shin, H.-S. Yu, H.-B. Chae, "Electron mobility in tris(8-hydroxyquinoline)aluminum (Alq3) films by transient electroluminescence from single layer organic light emitting diodes", *Applied Physics Letters* **2007**, *90*.

[109] D. Li, G. Dong, L. Duan, L. Wang, Y. Qiu, "New method of mobility measurement for organic semiconductors by optoelectronic coupling", *Journal of Physical Chemistry C* **2012**, *116*, 5235–5239.

[110] S. C. Tse, H. H. Fong, S. K. So, "Electron transit time and reliable mobility measurements from thick film hydroxyquinoline-based organic light-emitting diode", *Journal of Applied Physics* **2003**, *94*, 2033–2037.

[111] C. Hosokawa, H. Tokailin, H. Higashi, T. Kusumoto, "Transient behavior of organic thin film electroluminescence", *Applied Physics Letters* **1992**, *60*, 1220–1222.

[112] C. W. Tang, S. A. VanSlyke, C. H. Chen, "Electroluminescence of doped organic thin films", *Journal of Applied Physics* **1989**, *65*, 3610–3616.

[113] J. Kalinowski, L. C. Palilis, W. H. Kim, Z. H. Kafafi, "Determination of the width of the carrier recombination zone in organic light-emitting diodes", *Journal of Applied Physics* **2003**, *94*, 7764–7767.

[114] N. C. Erickson, R. J. Holmes, "Investigating the role of emissive layer architecture on the exciton recombination zone in organic light-emitting devices", *Advanced Functional Materials* **2013**, *23*, 5190–5198.

[115] S. Naka, H. Okada, H. Onnagawa, Y. Yamaguchi, T. Tsutsui, "Carrier transport properties of organic materials for {EL} device operation", *Synthetic Metals* **2000**, *111–112*, 331–333.

[116] C. Ma, O. Lengyel, J. Kovac, I. Bello, C. Lee, S. Lee, "Time-resolved transient electroluminescence measurements of emission from DCM-doped Alq3 layers", *Chemical Physics Letters* **Oct. 2004**, *397*, 87–90.

[117] V. Savvateev, A. Yakimov, D. Davidov, "Transient Electroluminescence from Poly (phenylenevinylene)-Based Devices", *Advanced materials* **1999**, *11*, 519–531.

[118] V. R. Nikitenko, V. I. Arkhipov, Y.-H. Tak, J. Pommerehne, H. Bässler, H.-H. Hörhold, “The overshoot effect in transient electroluminescence from organic bilayer light emitting diodes: Experiment and theory”, *Journal of Applied Physics* **1997**, *81*, 7514.

[119] J. M. Lupton, V. R. Nikitenko, I. D. W. Samuel, H. Bässler, “Time delayed electroluminescence overshoot in single layer polymer light-emitting diodes due to electrode luminescence quenching”, *Journal of Applied Physics* **2001**, *89*, 311–317.

[120] V. Chandra, M. Tiwari, B. Chandra, M. Ramrakhiani, “Electroluminescence overshoot effect in single layer pulsed organic light emitting diodes”, *Synthetic Metals* **2011**, *161*, 460–465.

[121] L. Niu, M. Guan, X. Chu, Y. Zeng, Y. Li, Y. Zhang, “Overshoot effect and inflexion characteristics in transient electroluminescence of hybrid phosphorescent OLEDs”, *Journal of Physics D: Applied Physics* **2015**, *48*, 055103.

[122] P. Chen, Q. Peng, L. Yao, N. Gao, F. Li, “Identifying the efficient inter-conversion between singlet and triplet charge-transfer states by magneto-electroluminescence study”, *Applied Physics Letters* **2013**, *102*.